Thermo-mechanical fatigue crack growth behaviour of Ti-6246

Jennie Palmer
(BEng *Hons.*)

Submitted to Swansea University in fulfilment of the requirements for the Degree of Doctor of Engineering

Swansea University

April 2020

DECLARATION

This work has not previously been accepted in substance for any degree and is not being concurrently submitted in candidature for any degree.

Signed [redacted] (candidate)

Date 24/04/20

STATEMENT 1

This thesis is the result of my own investigations, except where otherwise stated. Where correction services have been used, the extent and nature of the correction is clearly marked in a footnote(s).

Other sources are acknowledged by footnotes giving explicit references. A bibliography is appended.

Signed [redacted] (candidate)

Date 24/04/20

STATEMENT 2

I hereby give consent for my thesis, if accepted, to be available for photocopying and for inter-library loans **after expiry of a bar on access approved by the Swansea University.**

Signed [redacted] (candidate)

Date 24/04/20

ABSTRACT

Within the gas turbine engine, the high transient thermal stresses developed due to variations in power requirements during a typical flight cycle give rise to the phenomenon of thermo-mechanical fatigue (TMF). Associated with higher operating temperatures, the study of TMF within the gas turbine engine has mainly been focused on materials used in the latter turbine sections. However, the increasing temperatures to improve operating efficiency have led to the requirements for an understanding of the TMF behaviour in materials used for the later stages of the compressor. As such, fatigue crack growth rates are required to be evaluated under non-isothermal conditions along with the development of a detailed understanding of related failure mechanisms. In the current study a bespoke TMF crack growth (TMFCG) test set up has been developed and validated to investigate the TMFCG behaviour of the titanium alloy, Ti-6246. The study has explored the effects of phasing between mechanical loading and temperature, as well as the effects of maximum cycle temperature. Results show in-phase (IP) test conditions to have faster crack growth rates than out-of-phase (OP) test conditions, due to increased temperature at peak stress and therefore increased time-dependent crack growth. Fractography evidences subtle differences in fracture mechanisms and the microstructural analysis along the crack path has aided the characterisation of damage mechanisms in IP and OP test conditions.

TABLE OF CONTENTS

LIST OF FIGURES

LIST OF TABLES

ACKNOWLEDGEMENTS

The completion of this project would not have been possible without the encouragement and support of many people. First and foremost, I would like to thank my academic supervisor, Prof. Mark Whittaker. Having an approachable supervisor with a wealth of knowledge in both titanium alloys and TMF testing has been invaluable. I would also like to express my deepest gratitude to Dr. Jonathan Jones for the continued technical input and endless support throughout the project; without it, the project would not be the success it is.

I would also like to thank Rolls-Royce plc and EPSRC for the sponsorship throughout the project, providing both the funding and the material. In particular, thank you to my industrial supervisor, Mr. Steve Williams for your technical expertise and insight into the project.

Special thanks go out to the entire staff at the Institute of Structural Materials and Swansea Materials Research & Testing at Swansea University. I would like to thank the workshop staff for their continued help and support in developing and maintaining the test facilities used throughout this project. Thank you to Julie Palmer for your endless admin support that ensured not only the research project continued smoothly, but also enabled me to develop through various training courses and conferences. I would also like to thank Prof. Robert Lancaster for the encouragement to embark on the EngD programme and for the extended support and guidance throughout.

Thank you to Turan Dirlik for the technical support in developing and maintaining the software used throughout the project.

Finally, a massive thank you to my friends and family for their continued support and motivation. I know I would not be where I am today without it. In particular, thank you to my best friend and partner, Jason, for helping me switch off, relax and keep my spirits high.

NOMENCLATURE

ABBREVIATION/SYMBOL	DESCRIPTION
ACARE	Advisory Council for Aeronautics Research in Europe
α_p	Primary α lamellar
α_s	Secondary α lamellar
ACPD	Alternating current potential drop
ACW	Anti-clockwise
BCC	Body-centred cubic
CW	Clockwise
DCPD	Direct current potential drop
EBSD	Electron backscatter diffraction
EDS	Energy-dispersive X-ray spectroscopy
FCG	Fatigue crack growth
FEGSEM	Field emission gun scanning electron microscope
HCF	High cycle fatigue
HCP	Hexagonal close-packed
ICS	Induction coil system
IF	Isothermal fatigue
IFCG	Isothermal fatigue crack growth
IP	In-phase
IPF	Inverse pole figure
IRTC	Infrared thermography camera
LCF	Low cycle fatigue
MEK	Methyl-ethyl-ketone
MUD	Multiples of uniform distribution
OP	Out-of-phase
RLF	Radiant lamp furnace
S_a	Surface roughness
SE	Secondary electron
SEM	Scanning electron microscope
T_β	β-transus temperature
TC	Thermocouple
TEM	Transmission electron microscope
Ti-6246	Ti-6Al-2Sn-4Zr-6Mo

Ti-64	Ti-6Al-4V
T_{MAX}	Maximum temperature
TMF	Thermo-mechanical fatigue
TMFCG	Thermo-mechanical fatigue crack growth

1 INTRODUCTION

The aerospace industry is at the forefront of research, innovation and technology. With an increasing understanding of the impact of emissions on the environment, the aerospace industry is faced with the challenge to improve efficiency and reduce its environmental impact. As part of a European initiative to tackle climate change, the Advisory Council for Aeronautics Research in Europe (ACARE) is set out to achieve goals, such as reducing CO_2 emissions by 75% per passenger kilometre, by 2050 [1]. ACARE's 'Flightpath 2050' vision has placed significant pressure on the aero-engine industry to advance the materials used and push them to their limits.

As a result, modern gas turbine engines are expected to achieve increasingly higher levels of fuel economy, reduced NO_x emissions and noise, as was reducing the overall weight of the engine [2]. In order to achieve these goals, aero-engine manufacturers, such as Rolls-Royce plc., are challenged with improving the operating efficiency through the use of lighter materials and higher operating temperatures. As such, materials used for the traditionally cooler compressor sections of the gas turbine engine are being exposed to more challenging operating conditions.

Known for their high strength-to-weight ratio, titanium alloys are often a preferred choice within the aerospace industry for applications with low to intermediate operating temperatures. With the ability to operate at temperatures ranging from sub-zero to 600°C, they are utilised in the gas turbine for both discs and blades from the front fan to the last stage of the high-pressure compressor [3].

During the take-off, cruise, descent, and landing cycle that the jet engines experience when in service, high temperature features such as disc rims typically endure severe alternating thermal and mechanical loads, made more prominent with increasing operating temperatures. Such thermal stresses developed with the power requirements during a typical flight cycle can lead to the phenomenon of thermo-mechanical fatigue (TMF). TMF is the result of combined mechanical and thermal loading cyclically varying with time. The effects of this combined loading can be more damaging by more than an order of magnitude compared with isothermal fatigue at the maximum operating temperature [4]. With the improving efficiency of the gas turbine at the forefront of aerospace research, TMF is an important phenomenon to consider.

TMF testing can be carried out under strain or load control, both of which require the definition of phase angle (between thermal and mechanical strains or stresses) and loading direction. This programme investigates testing under load-controlled conditions where an in-phase (IP) cycle can be defined as having thermal and mechanical stresses increase/decrease concurrently. Tests conducted with a phase angle of 180°, also known as out-of-phase (OP), are defined as having the minimum temperature coincide with the peak stress and vice versa. Thus, there are an infinite number of phase angles between these two extremes and deviating from IP and OP introduces the relevance of loading direction, as this describes whether the loading history on the stress-temperature axes is clockwise (CW) or anti-clockwise (ACW).

With limited research conducted into the TMF crack growth (TMFCG) behaviour in titanium alloys, the focus of this project seeks to further investigate the complex interaction of creep, oxidation and TMF within the titanium alloy, Ti-6Al-2Sn-4Zr-6Mo (Ti-6246). Ti-6246 is an $\alpha+\beta$ alloy, with an evidently different microstructure to Ti-6Al-4V (Ti-64), displaying a fine Widmanstatten microstructure [5]. Ti-64 has traditionally not been exposed to in-service temperatures above 350°C and therefore typically high temperature damage mechanisms such as creep, have not been perceived to be a critical issue [6]. However, with the continuing desire to increase the operating temperatures of the gas turbine, alloys such as Ti-6246 and Ti-834 are being widely used at higher temperatures [7]. It is therefore becoming increasingly more important to ensure research is carried out to gain a better understanding of the TMFCG behaviour of the material.

The purpose of this research is therefore to investigate the crack growth behaviour of Ti-6246 under TMF conditions to allow for a more representative understanding of its behaviour during in-service conditions, particularly within the gas turbine.

2 PROJECT OBJECTIVES

The objective of this project is to investigate the crack growth behaviour of a titanium alloy under TMF loading, including the effect of phase angle and peak temperature. This will therefore allow for more accurate prediction of crack growth rates, and thus reduce the need for inspection of components when considered using a life to first crack approach.

The development of a TMF crack growth (TMFCG) facility is clearly experimentally challenging, particularly the requirement for an appropriate combination of a crack monitoring method that couples effectively with the heating/cooling technique. This project has set out to develop a bespoke testing facility in which the TMFCG behaviour of alloys used within the jet engine can be tested in a way that is repeatable and reliable, by providing a laboratory environment that closely replicates in-service conditions.

A set of TMFCG tests, encompassing a complex array of testing conditions has been undertaken to establish the effect of the outlined test variables. With the ongoing requirement of accurate lifing methodologies in damage tolerant disc materials the overall motivation of this project is to aid the development and improve existing lifing models through the means of mechanical testing and fracture analysis.

3 LITERATURE REVIEW

3.1 The Gas Turbine

The gas turbine is an example of a structure that houses components expected to withstand high levels of stress and harsh conditions, such as high temperature, without failing. The fundamentals of operation of a gas turbine are as follows; air is drawn into a compressor section, where it is compressed, and the pressure is increased. At this point, the velocity of the air is also decreased, before entering the combustion chamber, where it is mixed with fuel and ignited. The high energy air-fuel mixture enters the turbine stage, where it expands down to the exhaust pressure, producing a shaft work output in the process. The turbine shaft work is used to drive the compressor; and in the case of a three-stage engine the low-pressure turbine drives the fan, the intermediate-pressure turbine drives the intermediate-pressure compressor and the high-pressure turbine drives the high-pressure compressor. The resultant exhaust products are expelled, producing a forward thrust and drives the vehicle forward.

Jet propulsion is a practical application of Newton's third law of motion: for every action there is an opposite and equal reaction. By thrusting a large volume of air rearwards through a jet engine, an equal and opposite force is produced propelling the aircraft forwards.

The aeroengine industry has become increasingly competitive and continuous improvements to engine efficiency and environmental impact, over the past 70 years, have been fundamental to commercial success. Since the 1970's fuel consumption has decreased by 25% and large reductions in noise and emissions have resulted in a much-reduced environmental impact of the jet engine. With the continuous desire to improve the gas turbine's efficiency, there is a requirement for a collaboration of multiple disciplines, however, it is fundamentally dependent on the capability of the materials employed by the jet engine [8].

Originally the jet engine predominantly comprised of steel. However, due to the demand for increasing operating temperatures, the use of steel within the engine has been reduced and is now dominated by titanium alloys in the earlier, cooler sections of the jet engine, and nickel superalloys in the later, hotter sections as displayed in Figure 3.1. The shaft, over time, has remained steel. In recent years, both ceramics and composites have entered the gas turbine [9].

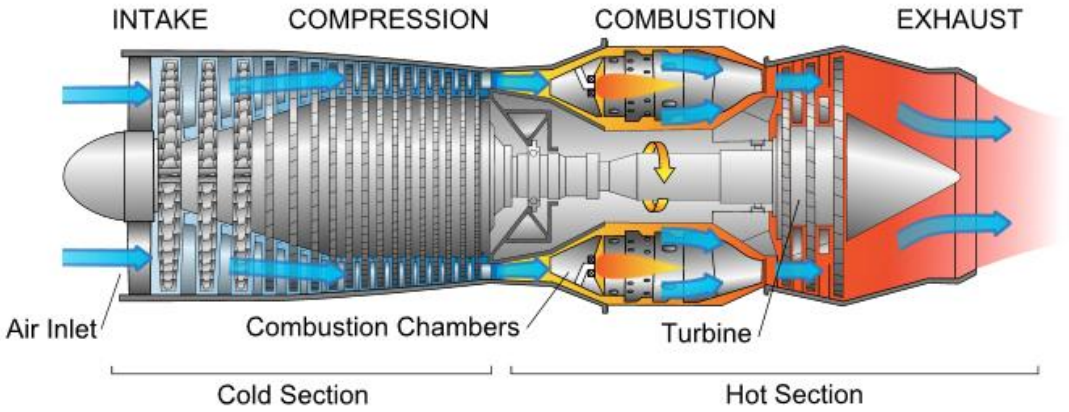

Figure 3.1 Schematic of the gas turbine engine, displaying the different sections [9]

3.1.1 The Compressor Section

The compressor is responsible for efficiently raising the pressure of the working fluid passing through it. As the air is drawn in via the fan and passes through the compressor, it is compressed by passing through a number of stages. Each stage of the compressor comprises of a set of rotor blades attached to a rotating disc, followed by a set of stator vanes attached to a stationary disc. The operating principles of the compressor are such that the air enters progressively smaller areas, resulting in an increase in the air pressure. This results in an increase in the energy potential of the air, and thus an increase in total pressure. Due to the divergence of the blade flow paths, the majority of the increase is in the form of velocity, with a small increase in static pressure. As the air then passes through the stator vanes, the flow is decelerated, converting the accelerated velocity to higher static pressure. The stator vanes are positioned at such an angle that the exiting air is directed efficiently towards the rotor blades of the next stage. This process is repeated through each stage, before the desired pressure ratio is achieved and the compressed air enters the combustor [10].

Circumferential Loading Slot

A typical axial compressor used in aero engines usually comprises of 6 to 14 stages. They consist of alternate stator and rotor stages. The rotors are composed of a rotor disc with the blades attached to the disc rim using either an axial root fixing or a circumferential root fixing [11].

Axial fixings are where a series of slots are machined out of the disc to accept the dovetail or fir-tree shaped rotor blade fixing, as shown in Figure 3.2 a) [9]. These fixings are more complex and more costly than the circumferential alternative. However, they are generally more robust for handling foreign object damage and thus are typically used in the earlier stages of the compressor. Circumferential fixings are usually more simple and cheaper and are used in the latter stages of the compressor, where the loading requirements are less. Consisting of an annular groove at the head of the disc, circumferential fixings are relatively easy to machine. The blades are assembled into the disc through a loading slot and the ring is then closed with a locking device, as shown in Figure 3.2 b) [9].

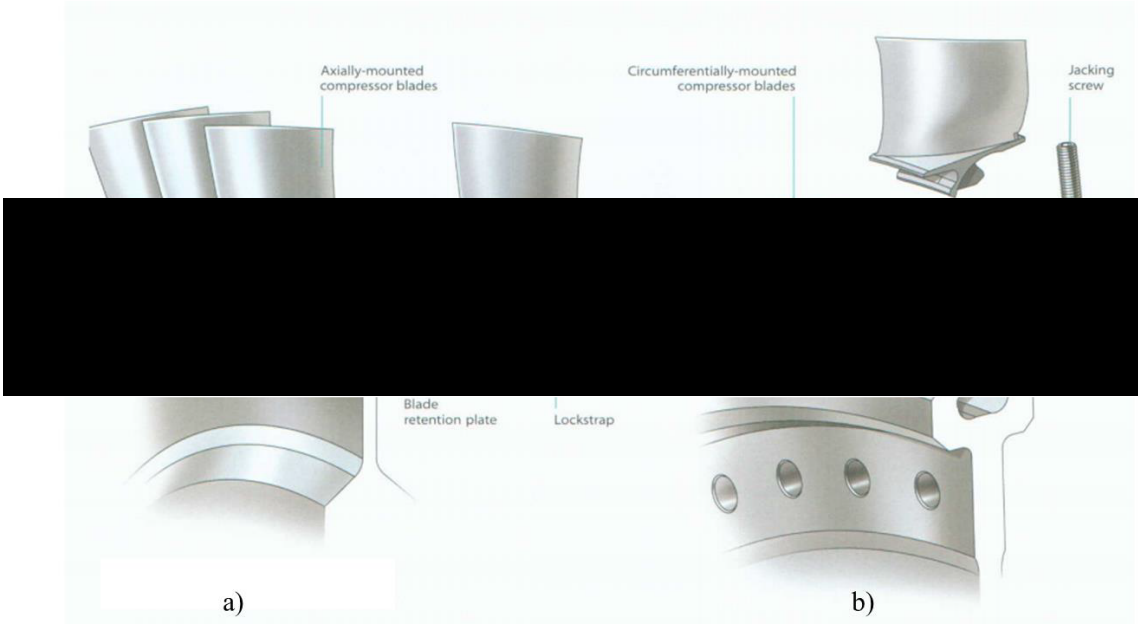

Figure 3.2 a) Schematic of axial fixings and rotor blades with dovetail root fixings, b) Schematic of circumferential fixings and locking device [9]

The total disc stress is comprised of a combination of the stresses imposed by the blades and spacers, the inertia stresses within the disc itself, and the thermal stresses imposed by bore to rim thermal gradients. With continually increasing core temperatures, these thermal stresses are becoming more significant. They are induced when the rim heats up at a faster rate than the bore, during acceleration, as well as from steady state running, whereby the speed is reduced and the bore cools down much slower than the rim.

It is the combination of the induced thermal and mechanical stresses on the circumferential loading slots, as shown in Figure 3.3, that are driving the motivation for the need to further understand the TMFCG behaviour in titanium alloys.

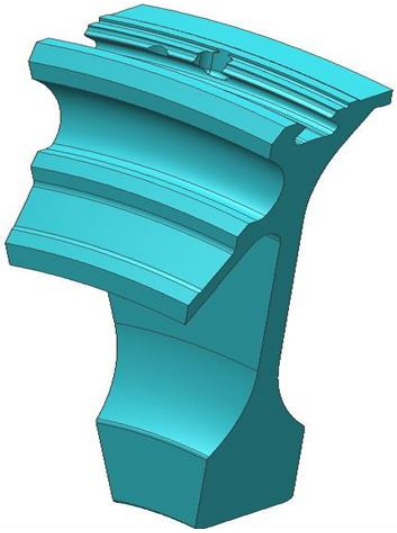

Figure 3.3 Schematic illustrating the circumferential loading slot – the area of interest for understanding the TMFCG behaviour in this study

3.2 Titanium Alloys

Titanium is the ninth most abundant element on Earth with its oxide found widely distributed and in Britain, the commercial production of titanium alloys began in the early 1950's. Today, titanium alloys, and their attractive mechanical properties, make up 40% of the gas turbine engine [12]. Compared to steels, which dominated early engine designs within the aerospace industry, research and development of titanium alloys introduced a less dense, high strength competitor into the industry [13].

3.2.1 Crystallography

Similar to elements like iron, titanium experiences a change in crystallographic arrangement of the atoms at high temperature. In its pure form, this allotropic phase transformation in titanium occurs at 882°C. Below this transition temperature, the atomic structure is such that the atoms have a hexagonal close-packed (HCP) arrangement. This state is categorised as the α phase. At temperatures higher that 882°C, the atoms take on a body-centred cubic form (BCC), which is known as the β phase [14]. The crystallographic forms are illustrated in Figure 3.4.

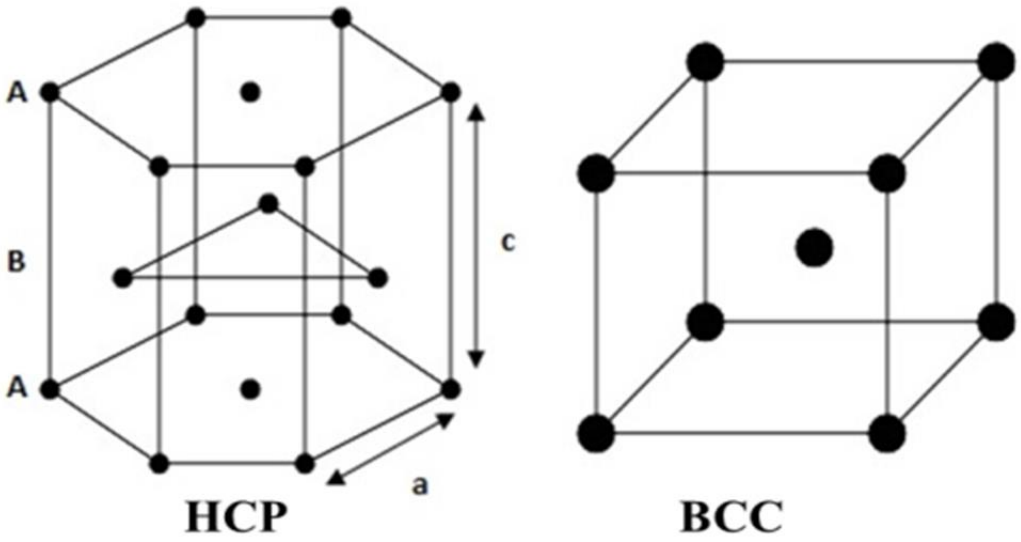

Figure 3.4 Schematic displaying the atomic arrangement of a HCP and BCC crystallographic structure

Figure 3.4 shows that within the BCC structure, atoms exist at each cube corner and one atom at the centre. For this structure, there are no close-packed planes, only close-packed directions. Therefore, unlike other atomic structures, because of the lack of close-packed planes within the BCC form, stacking sequences cease to exist, thus so do stacking faults [15]. As both the corner atom and centre atom positions are equivalent, the coordination number for the BCC crystal structure is eight as each centre atom has as nearest neighbours its eight corner atoms [16].

Unlike the BCC structure, the HCP structure is more complex. As can be seen in Figure 3.4, the HCP crystal structure is one in which cubic symmetry does not exist within the unit cell. The atomic structure consists of a top and bottom face, that both contain six atoms that form a regular hexagon around the atom located at the centre of each face. Another plane that provides an additional three atoms is located at the centre of the unit cell. The coordination number and atomic packing factor for the HCP are 12 and 0.74 respectively, with a stacking sequence of AB AB AB. Figure 3.4 also shows that the lattice parameter differs with direction in HCP structures, denoted as a and c. However, c will always be greater than a, resulting in a c/a ratio. This ratio should be 1.633; however, this ratio sometimes deviates from the ideal value [16].

3.3 Alloy Classification

Commercial titanium alloys are traditionally classified into three different categories; α, α+β and β alloys, depending on whether the alloying elements act to stabilise the hexagonal α phase or the body-centred cubic β phase. The effects of both α and β stabilisers on a titanium alloy are of paramount importance in understanding the mechanical properties of said alloy.

3.3.1 α Stabilisers

Aluminium is the strongest α stabiliser and for this reason, not only is it usual to express all the contributory elements as an 'aluminium equivalent', but it is also used widely in commercial alloys. Other α stabilisers include tin, zirconium and oxygen. The addition of α stabilisers to the titanium matrix results in an increase in the transformation temperature between the α and β phase. The phase diagram formed by this addition is displayed in Figure 3.5.

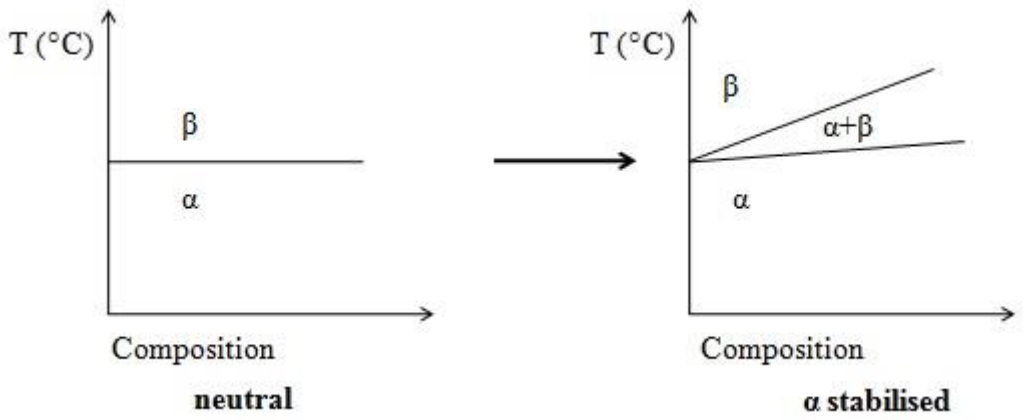

Figure 3.5 Phase diagram illustrating the effects of the addition of α stabilising elements to titanium

It is clear from Figure 3.5, that not only does the α phase field increase with increasing alloy content, but that a third phase is introduced in which both the α and β phase coexist. It must be noted that no amount of β can be retained by quenching to room temperature for any aluminium concentration.

Dissolving in the titanium matrix, aluminium acts as a strengthening agent for temperatures up to 550°C. The aluminium atoms are somewhat smaller that titanium atoms, thus their addition reduces both the 'a' and 'c' lattice parameters for the hexagonal unit cell [17]. Possessing a lower density, the addition of aluminium gives rise to an alloy that is less dense than pure titanium.

The benefits of adding aluminium were realised early on and alloys developed focused on improving both tensile strength and creep properties. Ti-6Al-4V and Ti-5Al-4.5Sn; two alloys that are still widely used, were developed in the 1950's. However, studies showed that as the amount of α stabilising elements were increased, mechanical properties were adversely affected. Although the creep strength continued to increase, the alloys became brittle during processing or when exposed to temperature, resulting in fabrication difficulties [18]. Thus, to avoid problems, the implementation of limiting the amount of α stabilising elements was introduced. For example, the development of high temperature strength alloys followed the rule: Al-equivalent ≤ 9 [17].

3.3.2 β Stabilisers

For β stabilisers, molybdenum is the most effective, thus the relative concentrations are expressed as a 'molybdenum equivalent'. Unlike the α stabilisers, β stabilising elements act to lower the transus temperature (as shown in Figure 3.6) and increase the amount of β phase retained in the alloy at room temperature.

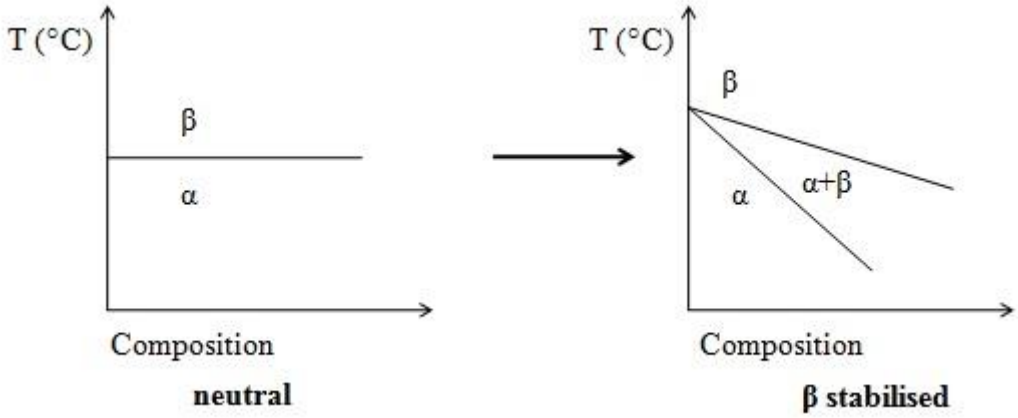

Figure 3.6 Phase diagram illustrating the effects of the addition of β stabilising elements to titanium

β stabilisers are characterised into two categories; isomorphous and eutectoids. Alloying elements that are categorised as isomorphous, such as molybdenum and vanadium, are so because they are mutually soluble with the β-titanium phase. Within the eutectoid series, a solid-state reaction in which two new phases are precipitated over a range of compositions, occurs. These phases are generally an intermetallic and a matrix rich α phase. Alloying elements that adhere to this trend include iron, manganese and chromium [19].

3.4 Ti-6Al-2Sn-4Zr-6Mo (Ti-6246)

Like most titanium alloys, Ti-6Al-2Sn-4Zr-6Mo (Ti-6246) is an alloy known for its exceptional strength to weight ratio. It is a solid solution strengthened α+β alloy widely used for the application of the intermediate stage of the compressor within the gas turbine.

Although known to have a higher temperature capability than Ti-64, the exact temperature capability of Ti-6246 depends on the loading conditions during service. Research suggests that for long-term load-carrying applications, the operating temperatures should not exceed 400°C. However, for short-term load-carrying applications, it has been reported that Ti-6246 can be operated at temperatures up to 540°C [20].

As with any titanium alloy, the microstructure of Ti-6246 is largely dependent on the thermo-mechanical processing route it undergoes. For applications requiring damage tolerance, a fully lamellar microstructure is desired. Enhancing the material's fracture toughness, a fully lamellar microstructure can be obtained reasonably easily in the final stages of the processing route. This is achieved with an annealing treatment in the β phase field, also known as β recrystallisation. In industry, the recrystallisation temperature is usually kept within 30-50°C above the β transus in order to maintain control of the β grain size [21].

It is important to note that the most influential parameter in the processing route is the cooling rate from the β phase field. This is due to the fact that the cooling rate determines the characteristic features of the lamellar microstructure, such as the size of the α-lamellae (α-plates/laths), the α colony size, and the thickness of α layers at β grain boundaries. These characteristics typically decrease with increasing cooling rate [22]. It is believed that the α colony size is of particular importance when considering mechanical properties of a fully lamellar microstructure, as presented in Ti-6246. This is due to the fact that this microstructural parameter determines the effective slip length and thus, the yield strength. For instance, applying a high cooling rate, results in a small α colony, basket-weave microstructure, which in turn, increases the yield strength of the material [21].

3.5 Thermo-mechanical Fatigue (TMF)

3.5.1 Introduction

In recent years, increasing the efficiency whilst reducing the environmental impact of the jet engine has been at the forefront of the aerospace industry. In order to achieve this demand, two approaches have been adopted: weight reduction and increasing the operating temperature. In both cases, it is evident that the current materials within the gas turbine will be impacted considerably. Materials with high temperature fatigue and creep capabilities, combined with suitable corrosion properties are desired and with such a competitive strength-to-weight ratio, along with its impressive corrosion resistance, much research into titanium alloys has been conducted.

During operations, such as start-up and shut down, many components within the gas turbine jet engine are simultaneously subjected to alternating mechanical and thermal loads. Such situations can result in the initiation and propagation of cracks through to failure, a phenomenon termed as thermo-mechanical fatigue (TMF) [23]. The thermo-mechanical loading conditions, within the gas turbine, are generated by the difference in phasing between the load and thermal gradients in the engine components during operation, known as the phase angle, denoted as ϕ.

A phenomenon that has been researched for several years, TMF is comprised of three damage mechanisms: creep, fatigue and oxidation. Depending on the phase angle, the extent of each damage mechanism may vary. The addition of the variable ϕ results in a number of TMF conditions to be considered, thus resulting in the realisation of TMF conditions in a laboratory environment proving challenging [24].

TMF can lead to a limited lifetime of a component compared to isothermal fatigue (IF) due to the additional deformation and damage mechanisms under varying temperature conditions. One of the major differences between IF and TMF is constraint. When exposed to heating, structures expand and as they do, they develop thermal gradients. Expansion at stress concentrators is usually constrained by the neighbouring cooler material. In the case of TMF, the thermal stress developed is converted into mechanical stress which can result in fatigue damage within the structure [4].

Much research has been carried out on IF of metal alloys, however, due to its time-consuming and complex nature, TMF is very much underreported, despite its great importance [25]. The data collected from IF tests are often used to predict deformation behaviour and lifetime of components exposed to TMF. However, previous studies, such as that conducted by Franclois and Remy (1991) shows that damage accumulated under TMF conditions is not directly comparable to IF. Franclois and Remy conducted a study on a cast cobalt-based superalloy, MAR-M 509 in which the TMF behaviour was compared to that of IF. They were able to conclude that isothermal low cycle fatigue life to crack initiation was shown to give an inaccurate prediction of TMF life [26].

A number of mechanical properties, including creep and fatigue resistance are utilised to assess how a material will perform at high temperature. However, due to the complex nature of TMF and the need to understand parameters such as phase angle, strain/stress range, temperature range and R ratio, mechanical properties for materials used for high temperature applications are generally obtained from IF testing. Testing under TMF test conditions is expensive and time-consuming; it is therefore evident that there is a clear requirement for an accurate life prediction model [24]. Researchers have been working towards this.

3.5.2 Phase Angle

The phase between the mechanical and thermal cycles, during TMF testing, is defined as the angular fraction of the cycle by which the mechanical cycle follows the thermal cycle; thus for a positive phase shift, the cycle follows an anti-clockwise path, with the maximum tensile stress occurring during the cooling stage, and vice versa [27].

The two phase angles most typically used to assess lives under TMF conditions are in-phase (IP) TMF ($\phi = 0°$); whereby the mechanical load in the material increases as the temperature increases and vice versa, and out-of-phase (OP) TMF ($\phi = -180°$); whereby the mechanical load decreases as the temperature increases and vice versa [28]. These two test conditions are illustrated in Figure 3.7.

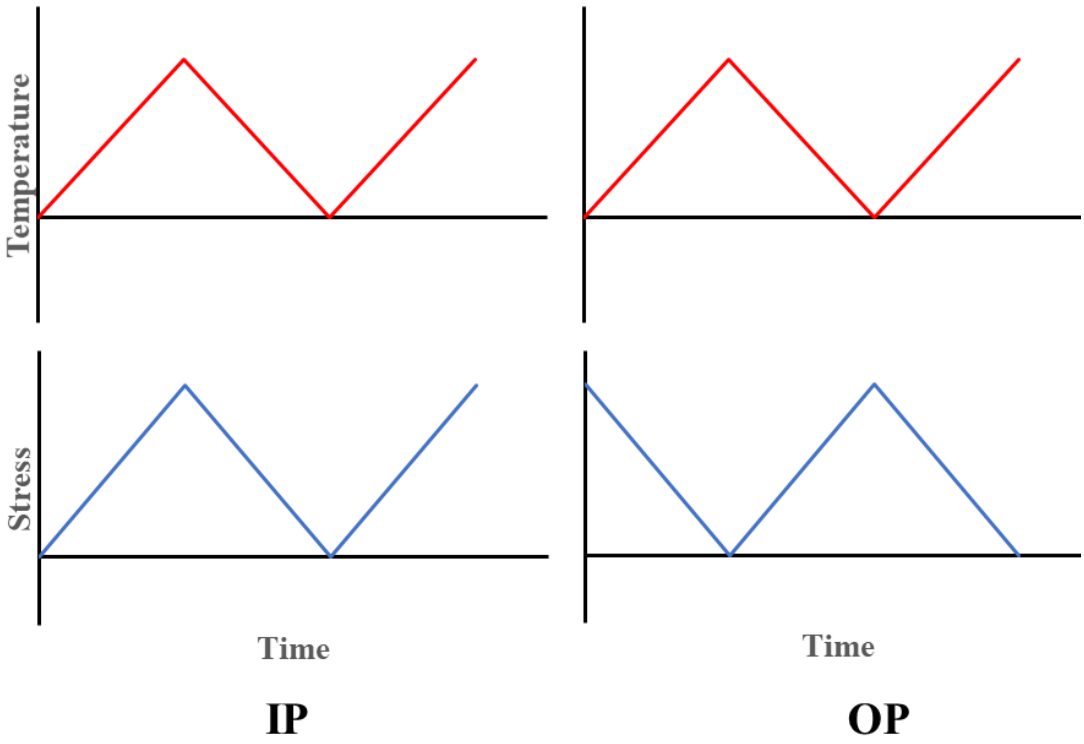

Figure 3.7 Diagram showing temperature and stress cycles under IP and OP test conditions

At present, investigations into the alternative phase angles, between the two extremes of IP and OP are limited. The research is further complicated with the fact that the cycle can take one of two directions around the stress-temperature loop; clockwise (CW) and anti-clockwise (ACW), as illustrated in Figure 3.8. It is therefore important that any model developed and/or adopted to describe TMF behaviour is capable of interpolation across phase angles [27].

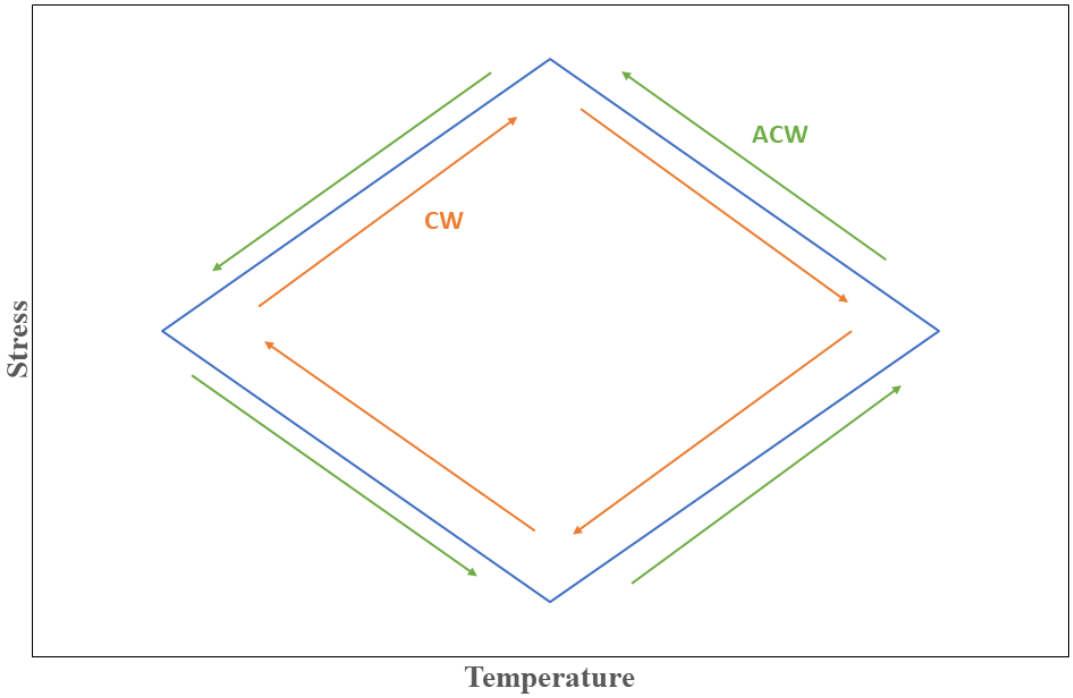

Figure 3.8 Diagram showing the cycling of stress against temperature for CW and ACW direction under TMF loading

3.5.3 Damage Mechanisms

There are three damage mechanisms associated with TMF: fatigue, creep and oxidation. These damage mechanisms may act independently or in combination according to various metals and operating conditions, such as temperature range, mechanical strain/stress range, phase angle or environmental factors.

Fatigue damage is traditionally defined as the weakening of a material caused by repeatedly applied loads. Creep refers to a material experiencing deformation at a constant stress level, leading to intergranular creep cavity growth and failure. However, under TMF conditions, it has been observed that creep deformation contributes to the formation and propagation of microcracks. Metal alloys are at risk to corrosion by oxidation when exposed to high temperature environments. A time dependent damage mechanism, oxidation is accelerated by the application of a tensile stress [29].

3.5.4 Fatigue

Fatigue involves the progressive development of cracks from initiation, through propagation stages to failure and is an important damage mechanism that affects the life of a material. It is therefore crucial to understand a material's mechanical behaviour to ensure safety whilst in service. It is a failure mode that occurs in structures and components that are subjected to dynamic stresses over an extended period of repeated stress or strain cycling. Being the single largest cause of failure in metals, estimated to comprise approximately 90% of all metallic failures, it is of paramount importance to ensure a material's properties and behaviours are well tested and understood [30]. It is usually a brittle failure, even in ductile materials and will typically occur in three stages; 1) crack initiation, in which a small crack forms at some point of high stress concentration; 2) crack propagation, during which the crack advances incrementally with each stress cycle; and 3) final failure, which occurs very rapidly once the advancing crack reaches a critical size [16].

First recorded in the first half of the nineteenth century, fatigue is usually defined into two regimes: low cycle fatigue (LCF) and high cycle fatigue (HCF). LCF is associated with relatively high loads that produce not only elastic strain but also some plastic strain during each cycle. The fatigue life in this domain is relatively short and occurs at less than 10^4 to 10^5 cycles. HCF occurs at lower stress levels wherein deformations are completely elastic, resulting in a greater fatigue life of more than 10^4 to 10^5 cycles [31]. Microstructure has an important influence on the fatigue properties of a material. With regards to titanium alloys, the HCF strength depends primarily on the resistance to dislocation motion. Similar to the dependence of yield stress, HCF strength depends highly on the slip length and α colony size, and thus is a function of the cooling rate from the β phase field. However, it should be noted, that for a fully lamellar microstructure, such as that present in Ti-6246, the absolute values for both the HCF strength and the yield stress depend, in addition to the cooling rate effect, on the details of the final annealing/aging treatment. The LCF strength of a material is a result of two contributing factors: its resistance to crack nucleation and its resistance to microcrack propagation. Both factors increase with increasing cooling rate from the β phase field, and thus the LCF strength of lamellar microstructures will increase under these circumstances [22].

LCF and HCF testing has been developed in an attempt to simulate in-service conditions, and thus has aided the development of higher performance alloys for the jet engine. As a result, designers have been able to identify specific component needs, thus allowing material choices to be made appropriately, such as materials with good LCF resistance for fan discs, whilst materials with better HCF resistance are required for components such as the fan blades [32].

Fatigue testing can be conducted under either strain control or load control. The difference being that strain-controlled specimens are cycled repeatedly between a maximum and minimum position, whilst load controlled specimens are repeatedly cycled between a maximum and minimum load.

Crack Initiation

In engineering components, the principal sites of fatigue crack initiation (or nucleation) include voids, inclusions, dents, scratches, macroscopic stress concentrations and areas of microstructural and chemical discontinuity. While the most likely location for cracks to initiate in metals and alloys of high purity is at surface grains, fatigue cracks in commercial alloys could form at both near-surface and interior locations [31].

In order to understand crack initiation during LCF in metals, it is necessary to understand the deformation mechanism within the material. In commercial alloys, the mechanism of plastic deformation, is achieved through slip or twinning of the crystalline lattices [33]. In a pristine material, with no existing cracks or defects, cracks will initiate through reversible slip damage concentrated in intense slip bands. Slip is promoted as the stresses tend towards the plastic regime. As the component is exposed to cycling tension and compression, the slip damage creates intrusions and extrusions [33]. These features are known as persistent slip bands. A schematic of this process is displayed in Figure 3.9.

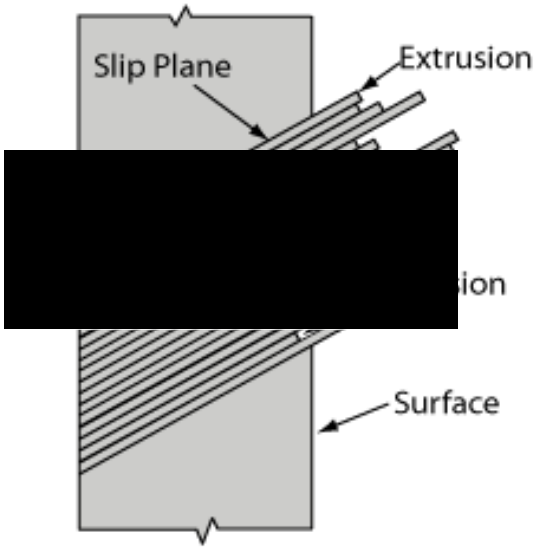

Figure 3.9 Schematic illustrating the process of surface crack initiation [34]

Crack Propagation

Fatigue crack propagation can be divided into three stages: stage I, stage II, and stage III. Once initiated, stage I involves a fatigue crack propagates along high shear stress planes, 45° to the cyclic stress, as displayed in the schematic in Figure 3.10. Also known as the short crack propagation stage, the crack propagates until a microstructural barrier is reached, causing a deceleration in crack growth. Such barriers include grain boundaries, inclusions and any features that cannot accommodate the initial crack growth direction. Therefore, in order to improve a materials fatigue strength, increasing the number of microstructural barriers is desired, thus grain refinement is encouraged [35].

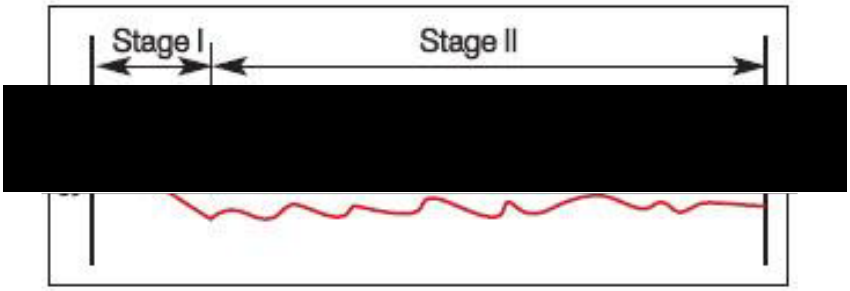

Figure 3.10 Schematic illustrating how a crack propagates through a specimen [36]

Stage II crack propagation is initiated when the stress intensity factor, K is increased due to the increase in applied loads, resulting in the development of slip in different planes close to the crack tip. Unlike stage I, stage II crack growth is perpendicular to the stress axis. The power law relationship, known as the Paris law, is utilised at this stage, and thus stage II is also commonly known as the Paris regime. The Paris law is expressed as follows:

$$\frac{da}{dN} = C\Delta K^m$$

Equation 1

Where a is the crack length, N is the number of load cycles, thus, the term on the left-hand side of the equation denotes the crack growth rate. On the right-hand side, C and m are material constants and ΔK is the range of the stress intensity factor [31].

The Paris law is a power law relationship between crack growth rate and the range of stress intensity factor and is typically visualised as a graph on a log-log plot, as illustrated in Figure 3.11 [37].

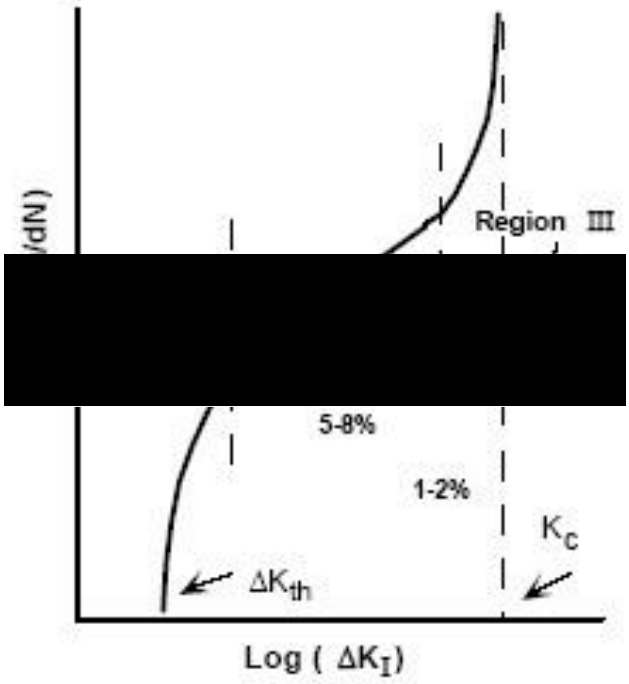

Figure 3.11 Log-log graph of crack growth rate against the range of stress intensity factor [38]

The crack, at this stage, continues to grow incrementally with each cycle and an important characteristic, known as 'striations' may develop within the material [35]. These striations, not visible to the naked eye, present as surface ripples, as shown in Figure 3.12 and can be seen with the aid of a scanning electron microscope (SEM) [39].

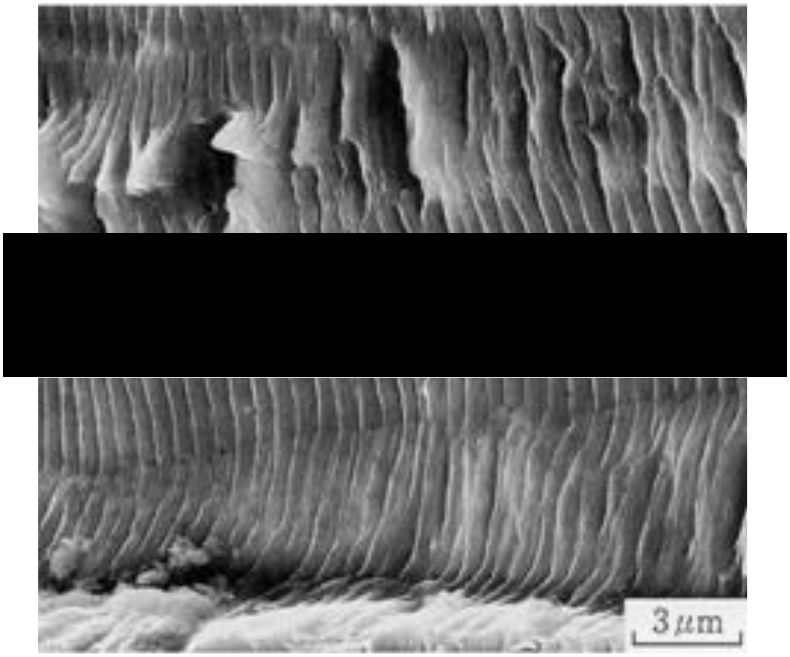

Figure 3.12 SEM image displaying striations [38]

The process of successive blunting and sharpening of a fatigue crack is the most accepted mechanism, as proposed by Laird (1979) for the formation of fatigue striations and is illustrated in Figure 3.13. The striation spacing, according to this mechanism, is equal to the crack growth rate per cycle, da/dN [40].

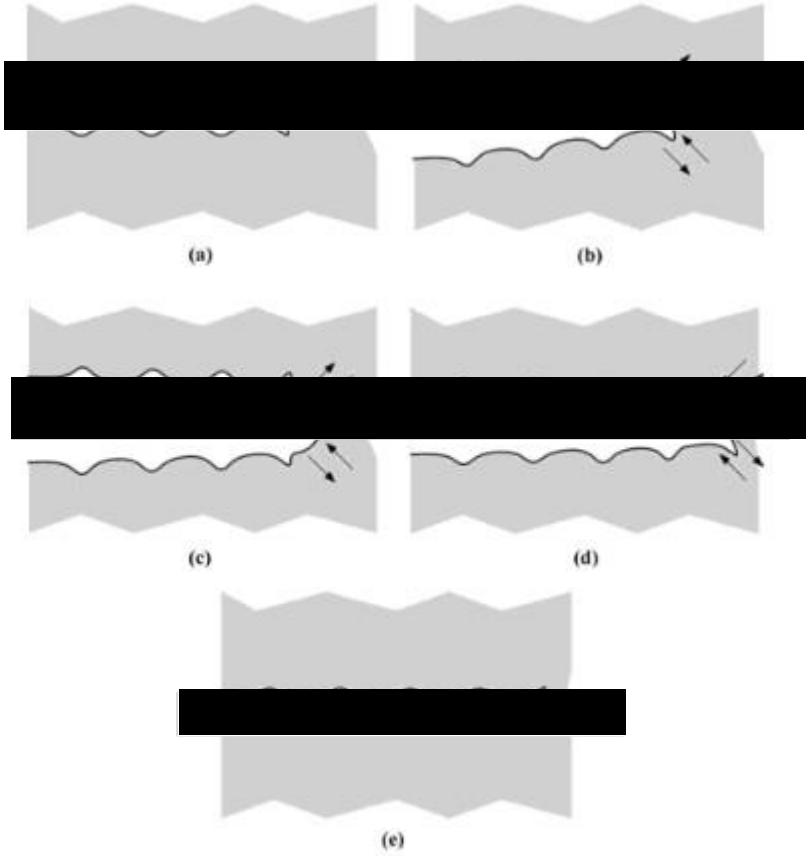

Figure 3.13 Schematic illustrating the formation of striations through the sharpening and blunting of a crack, as proposed by Laird [34]

An alternative view of fatigue, however, is the damage accumulation mechanism. A mechanism supported by Lankford and Davidson (1983) [41], states that a number of cycles are required to produce a critical amount of damage, at which time the crack grows by a small increment. They observed that striation spacing did not necessarily correlate to crack growth per cycle, but instead the correlation was dependent on the range of stress intensity factor, i.e. several cycles may be required to produce one striation [40].

Stage III of fatigue crack propagation is related to the unstable crack growth that occurs as the maximum stress intensity factor, K_{max} tends towards the critical stress intensity factor, K_{IC}. The crack growth during this stage is controlled by the static modes of failure and is particularly sensitive to the microstructure, stress ratio R and stress state. As final fracture occurs, the fracture surface appears more fibrous and irregular, as shown in Figure 3.14. The dominating feature that is present in final fracture consist of microvoid coalescences and/or cleavages [42].

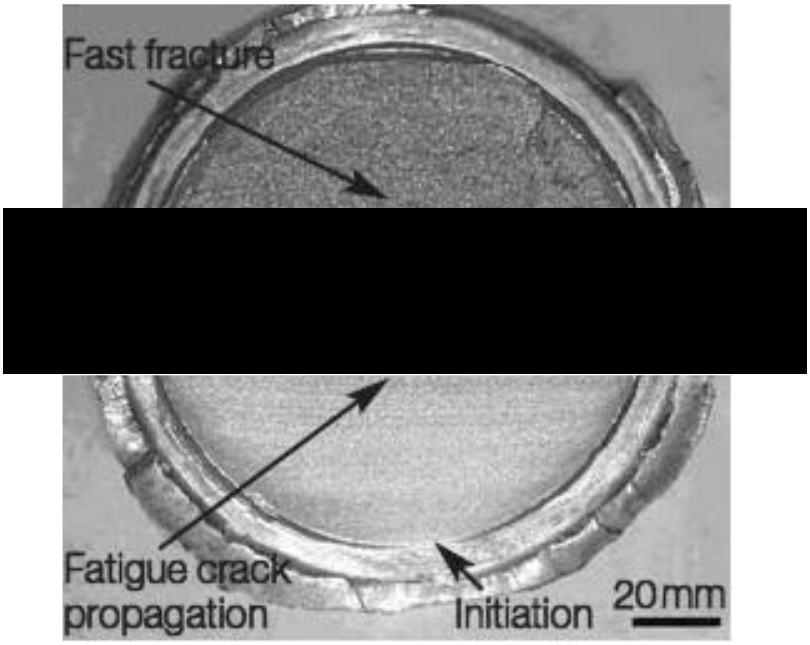

Figure 3.14 Image displaying the different stages of fatigue damage [43]

3.5.5 Creep

Defined as the time-dependent and permanent deformation behaviour of a material under cyclic loading conditions at elevated temperatures, creep is a dominating damage mechanism that is often a limiting factor to a component's life. Typically, a creep test consists of subjecting a specimen to a constant load or stress while maintaining a constant temperature. The deformation or strain is recorded and plotted as a function of elapsed time, as illustrated in Figure 3.15 [16].

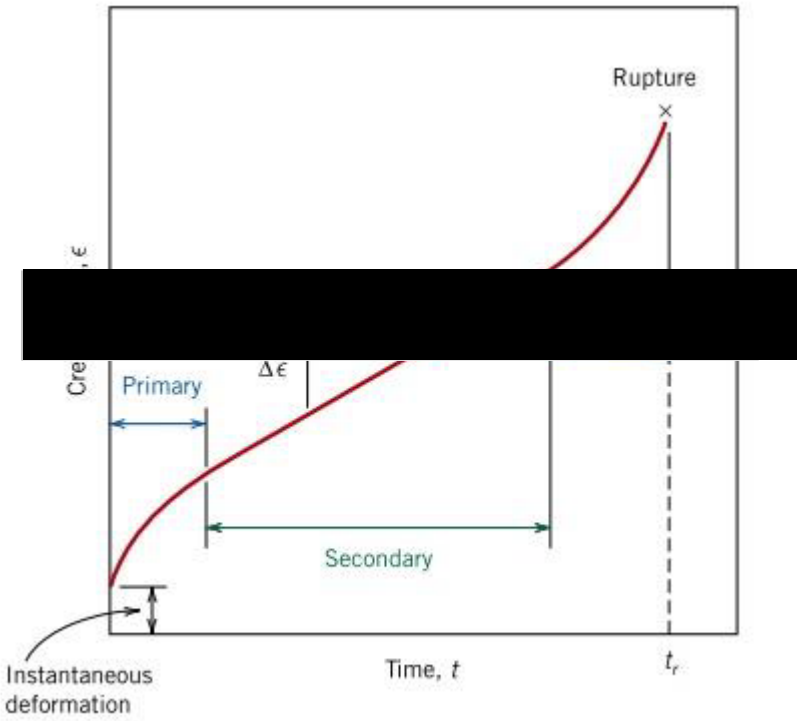

Figure 3.15 Creep strain curve with respect to time, displaying the different creep regions [15]

Upon application of the load in a creep test, there is an instantaneous deformation that occurs, as can be seen in Figure 3.15. Depending on the applied stress, this deformation can be completely elastic. The resulting creep curve consists of three regions: primary, secondary, and tertiary creep. In the initial stage of creep, or primary creep, the strain rate is relatively high, but slows with increasing time. This is due to the material experiencing an increase in creep resistance or strain hardening.

A traditional view of creep deformation is that the strain rate, with time, eventually reaches a minimum and becomes near constant, as illustrated by the linearity of the plot. This is the stage of secondary creep, or also known as steady-state creep and is the stage that is most understood. The stabilisation of the strain rate has been observed as the result of balancing between strain hardening and recovery; the process whereby the material becomes softer and retains its ability to experience deformation. This is often the longest stage of creep. The traditional view of steady-state creep is disregarded by some researchers, who have observed not a steady-state phase, but a minimum rate of creep, in which a decaying primary stage is offset by an accelerating tertiary stage [44].

Finally, tertiary creep involves the exponential increase in the strain rate and results in ultimate failure, also termed as rupture. This failure is a result of microstructural and/or metallurgical changes such as; grain boundary separation and the formation of internal cracks, cavities and voids [16].

Creep characteristics are influenced by both stress and temperature as shown in Figure 3.16.

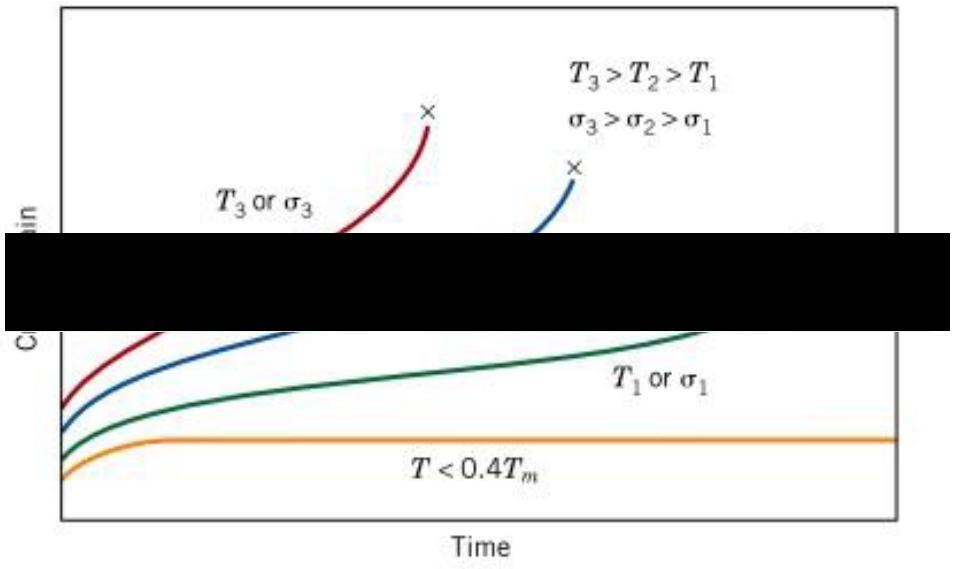

Figure 3.16 Creep strain versus time, illustrating the effects of temperature and stress [15]

As can be seen, with increasing stress and/or strain, the steady-state creep rate is increased, and the rupture life is diminished.

3.5.6 Oxidation

Titanium has a great affinity for oxygen and one of the benefits of this attraction is the formation of a protective oxide coat at ambient temperatures, resulting in an increase in tensile strength. During the oxidation process, this reaction results in the formation of the protective oxide coat, sometimes known as the 'scale', and an adjacent oxygen rich layer in the base metal. This layer is called α-case due to it being a continuous layer of oxygen stabilised α phase [22].

An increasing level in oxygen strengthens the α phase and changes the deformation behaviour of α titanium from a wavy to a planar slip mode. The formation of surface cracks under tensile loading could be the result of this harder, less ductile α-case. It is for this reason, that oxygen levels are controlled in alloy compositions to about 1500-2200ppm [17].

The diffusion rates through the oxide layer are slow enough, below 550°C, to prevent excess oxygen contents being dissolved in the bulk material, thus no significant formation of α-case occurs. For this reason, the operation temperature for conventional titanium alloys is limited to a temperature regime below 550°C [22].

In order to decrease the diffusion rate of oxygen through the scale, various additions of alloying elements have been investigated. A study into the α-case formation phase during the investment casting process, conducted by Lee, Jeon and Kim (2006), investigated different molds. They were able to conclude that the use of Al_2O_3+10Ti and Al_2O_3+50Ti as a primary coat was effective in reducing the formation of α-case. This was because TiO acted as a diffusion barrier, decreasing the oxygen solubility in titanium during the casting process [45].

During TMF testing, it has been reported that oxidation damage is more likely to occur under OP loading. This is due to the fact that whilst the specimen is under compression at higher temperatures, the high affinity of oxygen and titanium causes an oxide film to build up. However, as the specimen is subject to the low temperature tensile portion of the OP loading cycle, where the oxide film becomes more brittle, the oxide film ruptures and spalls. Mechanical straining then leads to more cracking and the exposure of a new clean surface; thus, the clean metal will rapidly oxidise and the process will repeat itself during the subsequent cycles [23].

3.5.7 TMF Lifing Predictions

TMF cannot be accurately predicted solely through the use of IF and creep test data, as the combined effect of thermal and mechanical loading during the 'flight cycle', as well as 'start up' and 'shut down' procedures can produce diverse results in comparison. Life predictions can be non-conservative as a result of the relevant damage mechanisms not being correctly represented and therefore, the complex damage mechanism, TMF needs to be considered for more accurate in-service conditions to be replicated and component lives to be predicted [24].

The limited attempts to model TMF behaviour can be broadly categorised into two categories; the first assumes that for a large portion of the TMF life, under strain-controlled testing, is spent in crack initiation. Based on this assumption, traditional methods such as the strain-energy partitioning and Coffin-Manson approach; can be adopted. On the other hand, the second category assumes that cracks form very early in the test, possibly from the first cycle, and thus, the TMF life is dominated by crack propagation [24].

It is concluded by a number of researchers that under test conditions where a constant strain range is utilised across phase angles, the mean stress is an important factor and that a relationship exists between the mean stress and the fatigue life [24][46].

In 1992, T. E. Strangman of Allied-Signal Aerospace Company; developed a TMF life model for coated superalloy turbine components. At the time, it was claimed that the model was unique in that it calculates both mechanical and environmental contributions (transient oxidation and hot corrosion) to coating crack penetration into the superalloy. Concentrating on OP TMF cycles, it was concluded that the TMF model predicts lives as a function of engine design, mission usage and materials system parameters [47].

Ostergren Model

Originally used in conjunction with isothermal testing, the Ostergren model is a life prediction model based on energy, in which the occurrence of failure due to the repeated tensile energy dissipation in a hysteresis loop is considered [48]. It can be modified to consider the effect of oxidation, temperature and frequency obtained by implementing a combination of the frequency-modified Ostergren mode and the Antolovich oxidation damage model [49].

Huang et al. found the Ostergren model can describe the damage occurring during TMF tests [49]. However, it was found that a great disparity of fatigue life occurred for IF and TMF tests at low Ostergren energy, and thus it is concluded the Ostergren model is not suitable for predicting the TMF life by using IF data at the maximum temperature. It was also observed, by de la Yedra et al. that predictions made for IP test conditions were inaccurate and predictions made for OP test conditions were over conservative; suggesting the parameter in the Ostergren model does not capture all variables involved with TMF [49]. Beck et al. observed similar results and believe the contribution of thermally activated processes reduced the IP TMF life [49]. A study carried out by Lee et al. also found inaccurate TMF predictions were made using the Ostergren model and existing LCF data. In an attempt to predict the TMF life of Ni-based superalloy, IN738LC for the use of gas turbine blades, Lee et al. concluded IP TMF predictions were more accurate than OP TMF predictions, in which no trend was seen. Thus, indicating that the Ostergren model is not suitable for predicting the OP TMF life cycle using LCF data, and hence reaffirming the complex nature of TMF damage mechanisms [49].

Zamrik Model

Similar to the Ostergren model, the Zamrik model is an energy-based life prediction method, specifically proposed to improve OP TMF life prediction. Again, reliant on the use of LCF data, Huang et al. found the Zamrik model possessed a good capability of predicting OP TMF life and is more suitable and precise than the Ostergren model. However, de la Yedra et al. found the model resulted in a poor prediction [50]. Lee et al. also concluded from their study that, although the Zamrik model was able to more accurately predict the OP TMF life of IN738LC using LCF data than the Ostergren model, it is far from a perfect prediction [51]. More recently, Barrett et al. investigated the use of TMF life prediction models in 9-12Cr steels and concluded that conventional methods such as Ostergren and Zamrik, should be exercised with caution; particularly as they found such models break down for cases of TMF loading with high temperature dwell periods [51].

It is clear there is a requirement to develop a lifing model capable of handling the different damage mechanisms associated with diverse loading conditions at high temperatures. Extensive testing in combination with a detailed microstructural and fractographic analysis must be undertaken in order to achieve such a model.

3.5.8 Previous Work

Isothermal Fatigue Crack Growth (IFCG) Behaviour in Ti-6246

Fatigue crack growth (FCG) properties of titanium alloys, including near-threshold and Paris region, are of great significance and have been extensively studied by many investigators [52]–[65]. The predominant influencing factors on FCG behaviour range from loading conditions and environment to alloy composition and microstructure [66]. These factors are hard to decouple and the resulting effects on the final FCG behaviour include crack closure, crack blunting, crack propagation and so on.

The fatigue crack growth behaviour in Ti-64, under isothermal conditions, is well researched and understood [53][54][67][65]. However, limited data about the FCG behaviour of high temperature and high strength titanium alloys have been reported [66]. Qiu et al. compared the long crack FCG behaviour in relation with the alloy types, different lamellar microstructures and stress ratios in the case of three α+β titanium alloys with nominal composition of Ti-6Al-2Sn-4Zr-xMo (x = 2, 4 and 6) [66]. The researchers found the damage tolerance properties from Ti-6242 to Ti-6246 alloys were degraded with increasing Mo content. This was driven by the variation of α/β colony size. The property discrepancy was more obvious for the early stage of the Paris-region, where FCG behaviour was sensitive to microstructure and usually resulted in the cleavage propagation and zig-zag paths. Larger α/β colonies were found to lead to higher crack deflection and thus, slower FCG rates. As well as microstructural effects, the researchers were able to conclude stress ratios also affected the FCG behaviour; where a higher stress ratio corresponded to lower crack deflection and higher FCG rates [66].

Ghonem (2010) also investigated the effect of microstructure on FCG mechanisms in high temperature titanium alloys. In general, it is observed that a coarse microstructure is more resistant to crack propagation, whereas a finer microstructure tends to be beneficial in delaying crack initiation [63]. Like Qiu et al., Yoder and Eylon placed particular emphasis on the role of colony size in affecting the FCG behaviour [68]. Eylon et al. went further and stated not only the size but also the orientation of the colonies of similarly aligned α platelets, is a dominant factor in FCG, since intense shear bands developing ahead of the crack are highly influenced by microstructure orientation [69]–[72]. They also showed that in large α/β colonies, the FCG process might be interpreted by start/stop behaviour at colony boundaries, the stopping event being the initiation of cracking into the next colony. However, Ravichandran concluded that α platelets are predominant microstructure features in fully lamellar microstructures, while colonies are more important in Widmanstatten formation [73].

As a high temperature titanium alloy, investigations into the fatigue behaviour at elevated temperatures have been conducted by researchers. Beranger et al. carried out LCF tests between 20°C and 500°C on Ti-6246 and saw the alloy exhibits cyclic softening irrespective of the test temperature. At 20°C, the researchers found cyclic softening was due mainly to the dominant role of the long-range internal stress field in relation to the duplex structure of the material. Whereas, at 300°C and 500°C, the occurrence of Ti_3Al precipitation in the α phase and the related second phase shearing mechanism are the main origins of cyclic softening at higher temperatures [73]. Lesterlin et al. investigated the influence of environment at 500°C on the fatigue behaviour in a Ti-6246 alloy. Testing in humidified argon, air and vacuum, it was found, as shown in Figure 3.17, the FCG rate was accelerated in humified argon and air [74]. The propagation curves in humidified argon and air are characterised by a plateau. This plateau phenomenon in the mid-rate range is particularly pronounced and occurs at higher rates in humified argon than in air. Lesterlin et al. found this result supports that at 500°C, water vapour constitutes the active specie responsible for the great enhancement observed in the mid-rate range compared to the tests conducted in vacuum. Furthermore, the researchers were also able to conclude the different rates of FCG for the humidified argon and air emphasise that oxygen has no embrittling effect on crack tip fatigue damage and at least presents a protective role [74][75].

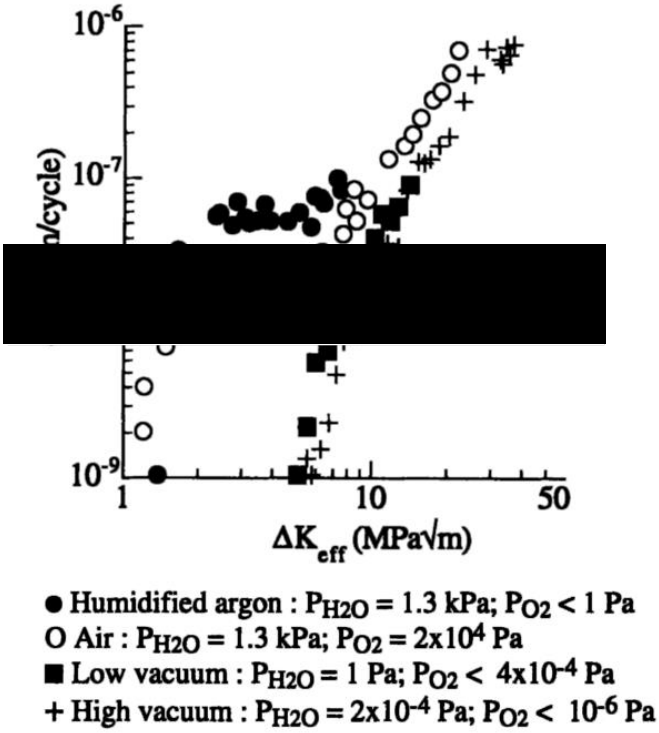

Figure 3.17 Fatigue crack growth rates in humidified argon, air, low vacuum and high vacuum, 35Hz, Lesterlin et al. [74]

Evans et al. investigated the interactions between fatigue, creep, and environmental damage in Ti-6246. Testing at temperatures ranging from 80°C to 550°C, Figure 3.18 shows a marked increase in FCG rates as the temperature rises, suggesting an increasing influence of high temperature damage due to creep and the environment [76]. An increase in the stress ratio also resulted in faster crack growth rates thereby demonstrating a strong dependence on mean stress.

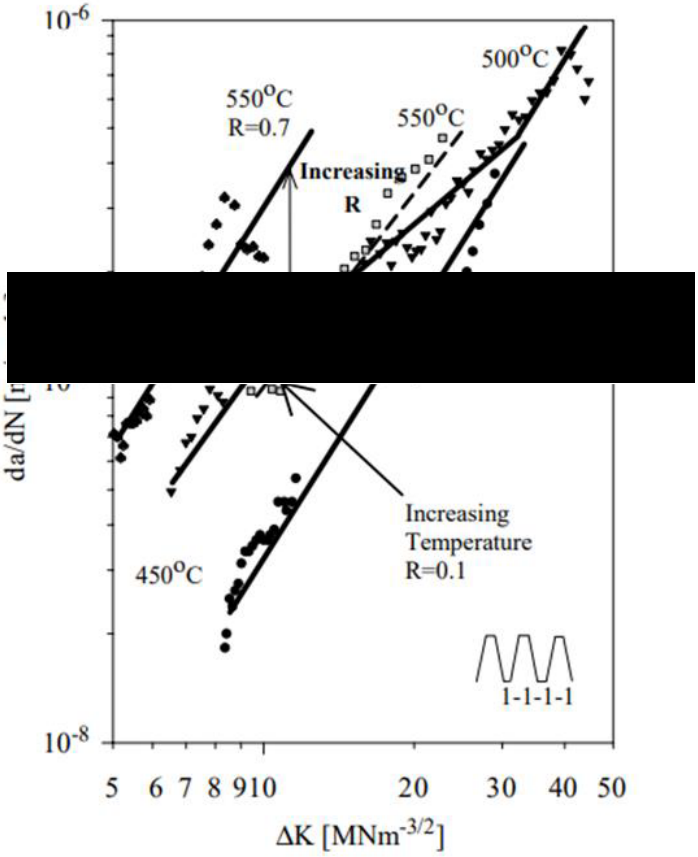

Figure 3.18 Fatigue crack growth rates in air for Ti-6246 showing the effects of temperature and stress ratio, Evans et al. [76]

In an attempt to partition the relative contributions offered by the environment and creep, Evans et al. conducted a series of FCG tests were performed under hard vacuum conditions. The results are illustrated in Figure 3.19. The creep contributions were established from the cyclic and dwell testing in high vacuum and the environmental influence was defined by directly comparing air and vacuum conditions under similar cyclic waveforms and loading conditions [76]. The researchers of this investigation highlighted the requirement for an advanced life prediction capability that embraces all three damage modes and thus, led them to focus their efforts on the development of such model [77]–[79].

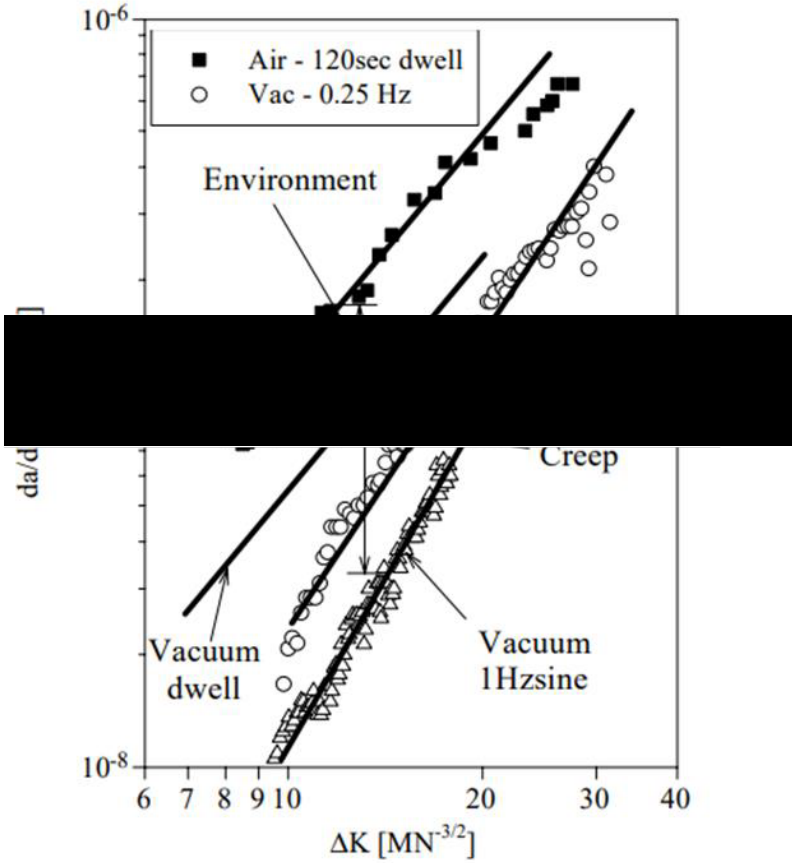

Figure 3.19 Fatigue crack growth rates in air for Ti-6246 showing the effects of temperature and stress ratio, Evans et al. [76]

Influence of Phase Angle in Nickel Alloys

The TMF crack initiation behaviour has been more widely explored in materials than the TMF crack propagation behaviour. Due to their higher temperature capabilities, this research has primarily focused on nickel-based superalloys.

Previous research has investigated the influence of phase angle on TMF behaviour. Pahlavanyali et al. studied the effect of phase angle shift on TMF life and failure of polycrystalline superalloy, Nimonic 90, tested IP, OP and ACW phase angles. Results showed that phase shifts of up to 20°, in either direction, had no effect on the failure mechanism, however, phase shifts did have an influence on the deformation and resultant TMF life [27]. These findings aided the development of the code of practice, which states than an upper limit of ±2° on deviations in the phase angle should be maintained when employing TMF tests [80].

A previous study by Jones et al. investigated the influence of phase angle, strain range and peak cycle temperature on the TMF crack initiation behaviour and damage mechanisms of the nickel-based superalloy, RR1000 [81]. The experiment involved testing at six diverse phase angles between 0° and -180°, two peak cycle temperatures and a mechanical strain range from 0.7 to 1.4%. From the extensive study, Jones et al. were able to conclude that, for RR1000, the phase angle employed had a significant influence on the cycle mean stress evolution, deformation, and damage behaviour, significantly influencing the TMF life. Moreover, the strain range and/or peak temperature affects the degree of this influence; with lower strain amplitudes resulting in detrimental effects on the OP TMF life, and higher strain amplitudes adversely affecting the IP TMF life [81]. This trend appears to follow through many investigations into the influence of phase angle on TMF behaviour in nickel alloys [25], [82]–[84].

Previous investigations on nickel alloys have all reported the same resulting failure mechanisms, in which IP loading gives rise to predominantly pure intergranular failure whilst OP loading gives rise to failure which is predominantly transgranular in nature [25], [27], [81], [83], [85]–[90].

TMFCG Behaviour in Nickel

TMFCG behaviour has not been as widely explored as TMF life, likely due to the added complexity of the need to reliably measure and monitor the crack during testing. As a result, there are currently no governing standards in place for such testing. However, as such an important area of material behaviour to understand, it has become apparent in recent years, that more research is being conducted in the subject area.

Research by Pretty et al., on the TMFCG behaviour in nickel-based superalloy, RR1000, showed that phase angle has an influence on the crack growth rate. It was possible to conclude from their findings that IP conditions result in faster crack growth rates than OP, due to the high stress and high temperature regime being more damaging in terms of creep and oxidation, giving rise to intergranular failure compared to the more transgranular-dominated failure in OP conditions. Diamond cycles were also found to be sensitive to loading direction, with the ACW (-90°) displaying a slightly increased growth rate, in comparison to the CW (+90°) condition [91].

TMF in Titanium

Although research on the TMF behaviour of nickel alloys is quite well established, that on the TMF behaviour of titanium alloys is limited. Prasad et al. compared the FCG behaviour in Ti-834 under isothermal and TMF conditions. The results, displayed in Figure 3.20, show faster crack growth rates at higher temperatures under both isothermal and TMF conditions. In terms of phase angle, it shows that under both temperature regimes, both IP and OP present similar FCG rates at the lower ΔK values, but as the ΔK increases, the OP crack growth rate is faster than the IP test conditions [92].

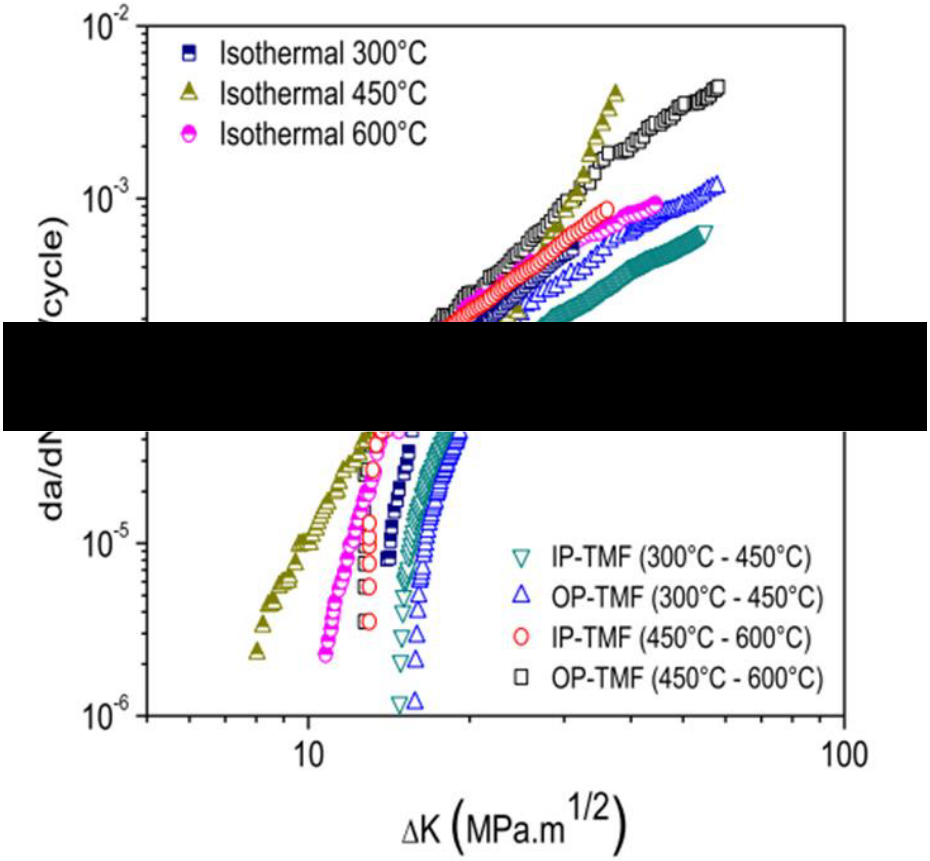

Figure 3.20 Fatigue crack growth rates for ti-834 under isothermal and TMF conditions, Prasad et al. [92]

Prasad and Kumar also conducted a study comparing the fatigue life of Ti-64 under isothermal and TMF conditions. They observed, as shown in Figure 3.21, that the alloy exhibits appreciably lower fatigue life under OP TMF loading compared to IP TMF and IF. The fatigue life under IP TMF was similar to that under 400°C IF loading, and the 100°C IF loading conditions resulted in the highest fatigue life. It was observed by the researchers, that under both IP and OP TMF loading, the fracture was dominated by transgranular crack propagation. Multiple crack initiation sites with tortuous crack paths were evident under IP TMF loading, whereas a relatively straight crack path was observed under OP TMF loading, with the fatigue crack clearly initiating from the fracture of oxide particles under the latter loading conditions. Thus, the investigators concluded the combined effect of tensile mean stresses and oxidation led to the detrimental OP TMF life as compared to the IP TMF and IF life [93].

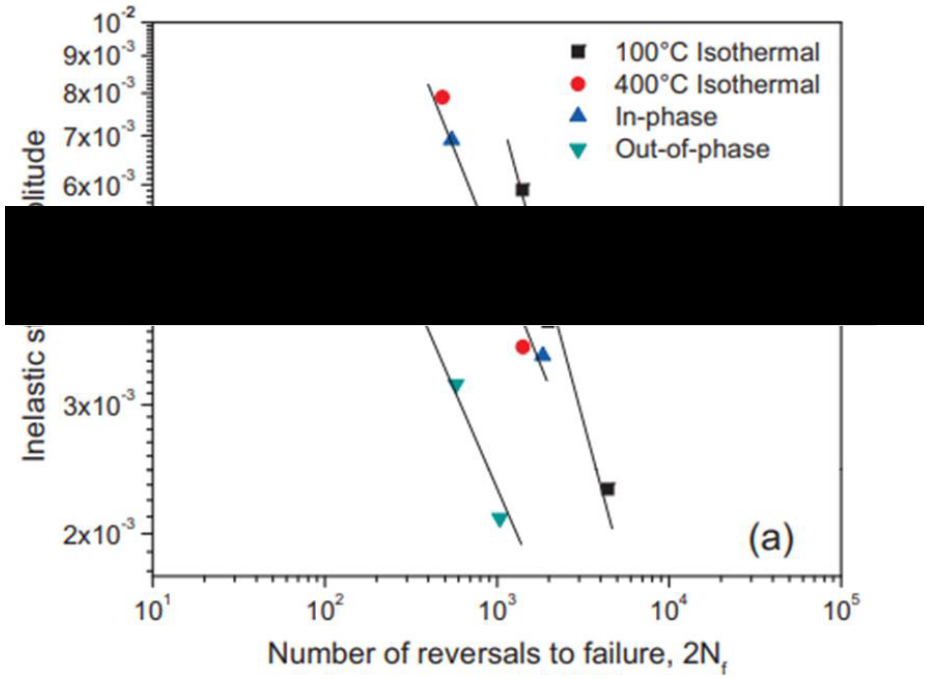

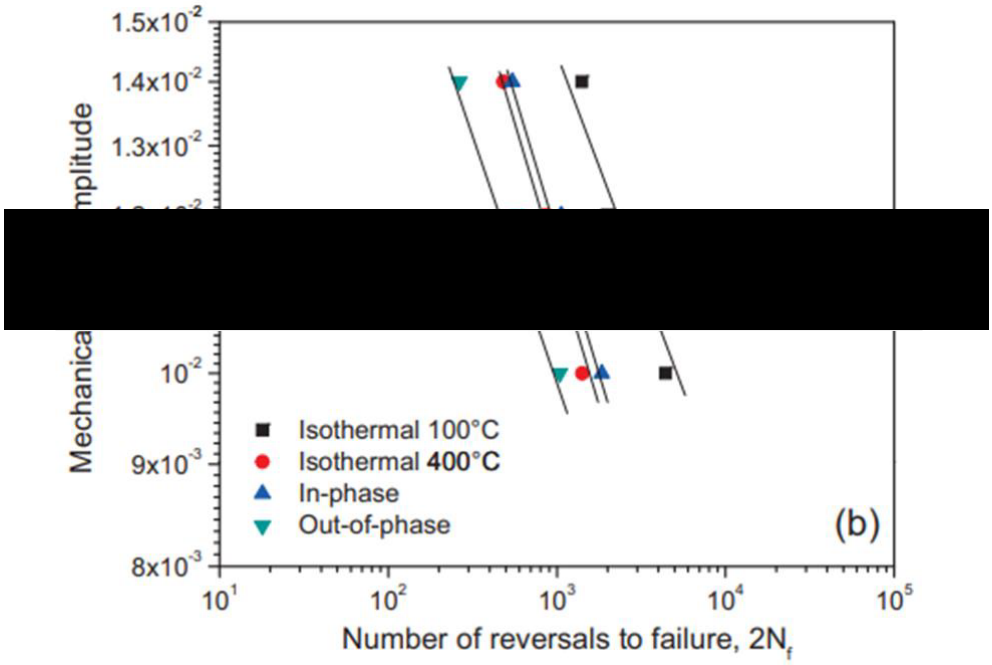

Figure 3.21 Fatigue life curves showing the variation of a) plastic strain amplitude and b) mechanical strain amplitude vs reversals to failure [93]

Investigating the environmental behaviour of Ti-834 under TMF conditions, Christ also concluded that OP TMF loading was found to be much more detrimental than IP cycling. However, the researcher noted that this effect can only partially be attributed to the positive mean stress which exists in OP TMF testing. It is seen that an embrittlement by hydrogen takes place at intermediate temperatures in addition to oxidation at high temperatures. Whilst under tension at an intermediate temperature, where a freshly formed alloy surface is exposed to the surrounding gas, as experienced in OP TMF loading, the effects of hydrogen are more prominent. In contrast, in IP loading, it was found that hydrogen effects are negligible since the relevant temperature range is passed through while in compression [94].

The complexity of TMF is highlighted in the research that exists, with the effects of phase angle and temperature range playing a large role. The study of previous work further validates the need to gain an understanding of the TMFCG behaviour in Ti-6246.

3.6 Dynamic Heating Methods

Under isothermal fatigue (IF) test conditions, the desired temperature can be achieved using a conventional split furnace, as shown in Figure 3.22. However, such a furnace is unable to achieve the rapid dynamic thermal cycles required during TMF test conditions. Within the aerospace industry, the gas turbine engine is exposed to rapid heating and cooling rates during different stages of the flight cycle; from take-off and climb to cruise and descent and thus, it is important that such rates are closely replicated in laboratory testing [95]. In order to achieve the required thermal cycles, a setup capable of the demanding test conditions is required, such as radiant lamp furnaces (RLFs) or induction coil systems (ICSs).

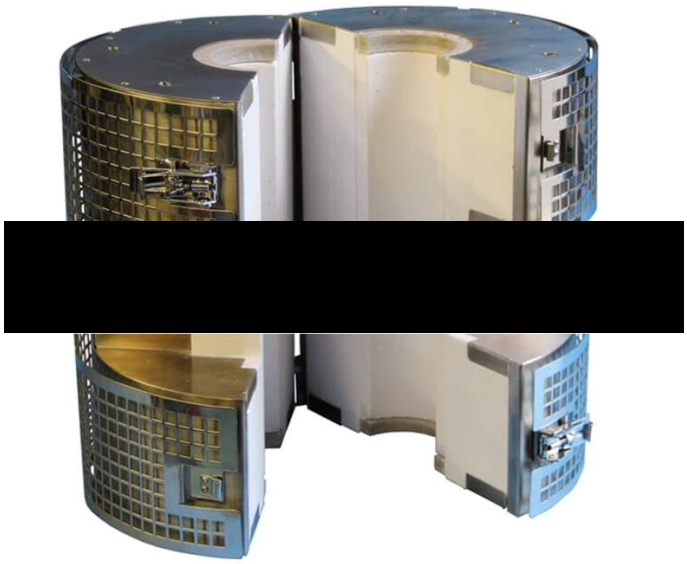

Figure 3.22 Image of conventional split furnace used as standard for FCG testing under isothermal conditions [96]

3.6.1 Induction Coil System (ICS)

Induction heating is a technique based on two principles; electromagnetic induction and the Joule effect, in which heat is produced within the material itself. By applying an alternating voltage to an induction coil, an alternating current will result and flow in the coil circuit. The resulting alternating coil current produces, in its surroundings, a time-variable magnetic field that has the same frequency as the coil current. This magnetic field induces eddy currents in the workpiece located inside the coil, and through the Joule effect, I^2R (where I is current and R is resistance), heat is produced [97].

An ICS has previously been employed in several institutions [98]. With their ease of adaptation and the ability to be applied to existing test frames, ICSs are an attractive choice for heating within TMF testing. Offering a relatively inexpensive and reliable heating solution, their flexibility also enables the use of established fixtures and specimen geometries, leading to direct comparisons with previous IF test results [98].

However, studies conducted by Yuan and Kalkhof stated that induction heating has the potential to influence crack propagation through preferential heating of the highly stressed region at the crack tip [99]. The occurrence of thermal gradients across the gauge length should therefore be minimised in order to ensure that the crack tip experiences similar conditions throughout cycling.

The importance of coil design has also been highlighted by researchers. Andersson et al. conducted a series of experiments to quantify the effect of temperature gradients existing over the gauge length of a cylindrical test piece. The tests were carried out with different ICSs and different heating/cooling rates and showed that the internal temperature differs from the external temperature [100]. Evans et al. undertook an analysis on the different coil designs that could be utilised for induction heating. They found that a problem arose whilst using large grips in their test apparatus as they acted as heat sinks drawing heat away from the specimen and thus development of the ICS was required [101].

3.6.2 Radiant Lamp Furnace (RLF)

RLFs offer a potential solution to preferential crack tip heating that may arise with ICSs. RLFs use an array of lamps around the specimen. Each lamp is backed by a parabolic reflector which focuses light towards the centre of the furnace. They have been used in a number of different experimental setups since the early 1990s when they were used by Pernot et al. [102] and Mall et. al [103].

3.7 Temperature Control Methods

Emphasised in the governing TMF standards for strain-controlled testing; ISO12111, and load-controlled testing, temperature measurement and control is considered a most critical issue in TMF testing and was in fact addressed by the European developmental code of practice to be a major source of scatter data during a round robin exercise [104]–[106]. Reliable test results can only be accomplished provided the temperature has been kept to within good temperature tolerances, as outlined in the aforementioned standards, which state the temperature at the centre of the gauge section should be controlled with an accuracy of ±5°C and the axial temperature gradients within the gauge length should not exceed ±10°C [104][105]. Usually temperatures are measured and controlled using thermocouples, infra-red pyrometry or more recently thermal imaging cameras.

3.7.1 Thermocouples

A thermocouple (TC) is a sensor for measuring temperature and is outlined in current governing standards as a recommended method to be used during TMF testing [104][105]. ISO12111, the international standard for strain controlled TMF testing encourages the use of TCs for temperature measurement, through either ribbon type, spot welded or coaxial contact TCs.

Ribbon type TCs can measure the direct temperature in the centre of the specimen's gauge length without risk of damaging the surface of the alloy. However, since they are wrapped around the specimen, as shown in Figure 3.23, rather than welded to the outer surface, care must be taken to ensure that there is sufficient thermal contact between the test piece and the thermocouple without any potential degradation during the period of the experiment through oxidation or roughening of the surface [23][105][106]. This method has not been widely used, seemingly due to a lack of consistency [107].

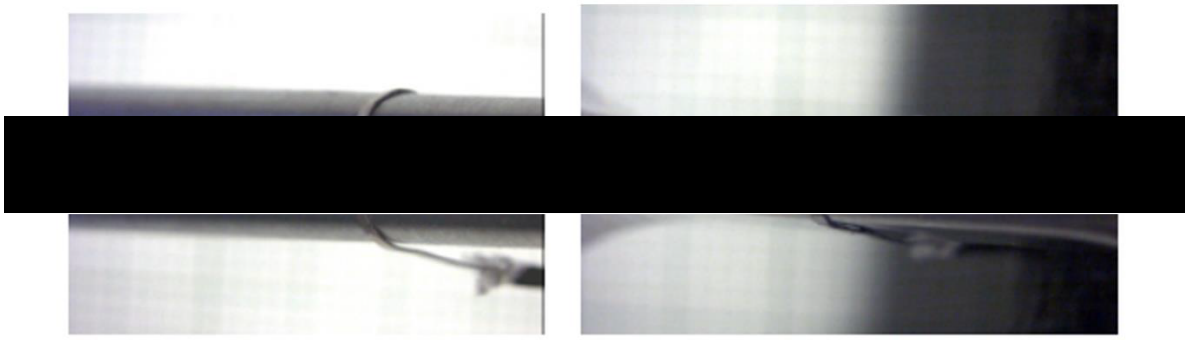

Figure 3.23 Image showing the wrapping of ribbon TCs [105]

Instead, welded TCs have become the dominant method by which control has been established [108]. As the welding process can cause a defect on the surface of the specimen, it is encouraged by the existing standards to spot-weld outside the critical volume of tested material, such as within the specimen gauge length, if the desire is to obtain an appropriate fatigue life under TMF loading [98][105]. The spot-weld can essentially act as a surface defect, which in turn acts as a stress raiser and thus, research has reported cracks initiating from the TC contact point [109]. Ensuring the TC wire diameter is as small as possible, using individual and not beaded TCs, and providing additional thermal contact by wrapping the TC wire around the test piece are methods that have reported to minimise the severity of the technique [108]. However, despite these measures, spot-welded TCs can induce a cold spot, resulting in a surface defect and hence, the possibility of a crack initiation site [106]. Justifying the outlined recommendations in the standards, TCs are not typically spot welded in the test piece gauge section, instead, it has become the recommendation that TCs are instead spot welded on the specimen shoulder for dynamic high temperature control [105][107]. The accuracy and practicality of such technique under rapid dynamic thermal cycles, however, has been questioned, despite recommendations. In particular, in specimens with a long parallel gauge section, where large distances exist between the material under investigation and the TC location on the test piece shoulder [95][107][110].

Coaxial TCs are another alternative, as shown in Figure 3.24. This method requires sufficiently deep holes to be drilled into the specimen, to allow insertion of the TC. The accuracy of this arrangement is dependent on the machined hole diameter, as the closer the TC diameter is to that of the hole, the more accurate the reading will be [108]. However, no matter the level of diligence, this method still proves challenging [111].

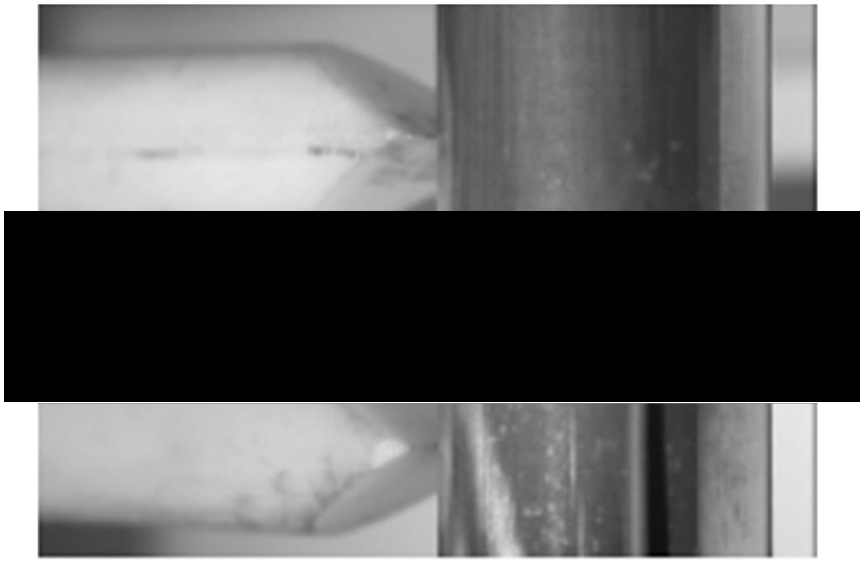

Figure 3.24 Image showing a coaxial TC fixed to the a specimen [105]

3.7.2 Pyrometry

Through the detection of thermal radiation emitted from the specimen's surface, pyrometry is a non-contact method for determining the specimen temperature during TMF testing. However, concerns have previously been raised regarding the use of pyrometers during high temperature applications as the technique is susceptible to the oxidation of the specimen surface over time [111][95]. Formation and growth of the oxide layer throughout a TMF test can lead to changes in the specimen's coefficient of emission and therefore affect the temperature stated by the pyrometer.

Therefore, to provide an accurate temperature measurement and/or control throughout a test, a pre-oxidised surface can be introduced prior to testing to ensure a stable emissivity value for the material [108]. Emissivity relates to the ability of a material to radiate infrared energy compared to a perfect blackbody for a given temperature. As such, emissivity is crucial for thermal measurements, since without knowing the emissivity of the object, it is not possible to determine the true value of its temperature [112]. Alternatively, high emissivity thermal paints can be used to stabilise emissivity, however this method has its own drawbacks as discussed by Jones [107][80][113].

Another possible downside of pyrometry is the method can only measure an area around $2mm^2$; a drawback shared with TCs [85]. Moreover, in order to profile a specimen using a pyrometer TCs must be used; hence, despite being a non-invasive technique and avoiding complications with TCs during testing, inherent temperature errors are open to be carried forward from the thermal profiling procedure using TCs. The ISO12111 standard does however allow for non-contact measurements to be made through techniques such as pyrometry and they are commonly used during TMF testing [114][101][115].

3.7.3 Infrared Thermography Camera (IRTC)

More recently, the possibility of temperature measurement, control, and profiling of TMF tests using an infrared thermography camera (IRTC) has been explored. An IRTC operates in a similar manner to a pyrometer, being dependent on emitted radiation from the test specimen (and therefore dependent on surface condition). IRTCs detect infra-red radiation given off by a test piece and produces images of that radiation, called thermograms. However, the method offers the opportunity to overcome a significant drawback of both TCs and pyrometry, in that only spot measurements can be made. The amount of radiation emitted increases with temperature and therefore it is possible for variations in temperature across the whole gauge length to be captured.

The operational background and principles of IRTC systems has been reported by Meola [116], whilst the influences of the material in use, emissivity complications, infra-red considerations, size and location of control area as well as other external influences on the accuracy and applicability of the IRTC to control temperature has been reported by Jones [107]. Jones was able to conclude that an IRTC system is a reliable non-invasive technique that is unaffected by heating and cooling of the specimen during TMF testing. In addition, the study confirmed that the camera can use an average temperature taken across the whole gauge length rather than at distinct points.

3.8 Fatigue Crack Monitoring

When investigating fatigue, there are two aspects of interest to consider: fatigue crack initiation and fatigue crack growth (FCG). It has become apparent through a lack of literature that TMFCG, despite being an important aspect to understand, is one that has not been investigated to the same extent as total TMF life. As already expressed, TMF is a complicated phenomenon and in order to successfully conduct TMF tests in aid of component lifing, temperature control and measurement is of paramount importance. However, when considering TMFCG, accurate crack monitoring also becomes of particular importance and thus leads to additional difficulties when testing. As there are no governing standards or code of practice currently available for TMFCG testing, it is important to draw on existing knowledge to aid the development of such documents and test techniques.

Studies conducted in the early 1980's utilised optical techniques as a method of crack monitoring [114][117][118] whilst the late 1980's saw a shift towards the use of direct current potential drop (DCPD) as an approach for monitoring crack growth [118]–[120].

Representing one of the possibilities to measure crack length during experimental TMFCG investigations, the DCPD method works on the principle of an occurrence of a discontinuity in a specimen being recorded when a homogeneous current of an adequate value is passed through the whole cross section of the specimen, causing a potential drop. This method has been widely adopted by governing standards and proven popular in the published literature [121][122].

As well as using a direct current, it is possible to use an alternating current in adoption of the potential drop technique (ACPD). Whereas the DCPD method relies on a large direct current (typically 30 amps) being passed through a specimen to measure resistance, the ACPD method relies on small alternating currents, typically of 1 amp, being passed through a specimen to measure impedance. Although both techniques have their advantages and disadvantages, ACPD has always suffered from the effect of pick up (voltages induced in the signal lead by the current supply lead) which can quite often result in dramatic alterations in the measured signal magnitudes [123].

The DCPD method is usually confined to the materials testing and research applications and is the more traditional and hence accepted, of the potential drop methods. The method, however, has not been widely investigated under dynamic temperature environments, and concern has been raised by researchers, with regards to the compatibility of combining DCPD monitoring with induction heating [101][108]. It is thought that the eddy currents produced from the induction heating may interact with the current required for DCPD monitoring, causing noise and interference. Research conducted by Pretty et al. shows the two methods to be a viable combination for TMFCG testing, providing care is taken in selecting an appropriate ICS, and thus this will form part of the investigation [91].

4 MATERIAL

4.1 Material Composition

The material studied throughout this investigation is titanium alloy, Ti-6246, in which the composition can be found in Table 4.1.

Table 4.1 Nominal composition of Ti-6246 disc material (Ti balance)

	Composition			
	Al	**Sn**	**Zr**	**Mo**
Titanium wt%	5.97	2.06	3.92	5.89

The energy-dispersive X-ray spectroscopy (EDS) maps in Figure 4.1 show the composition of the Ti-6246 specimens.

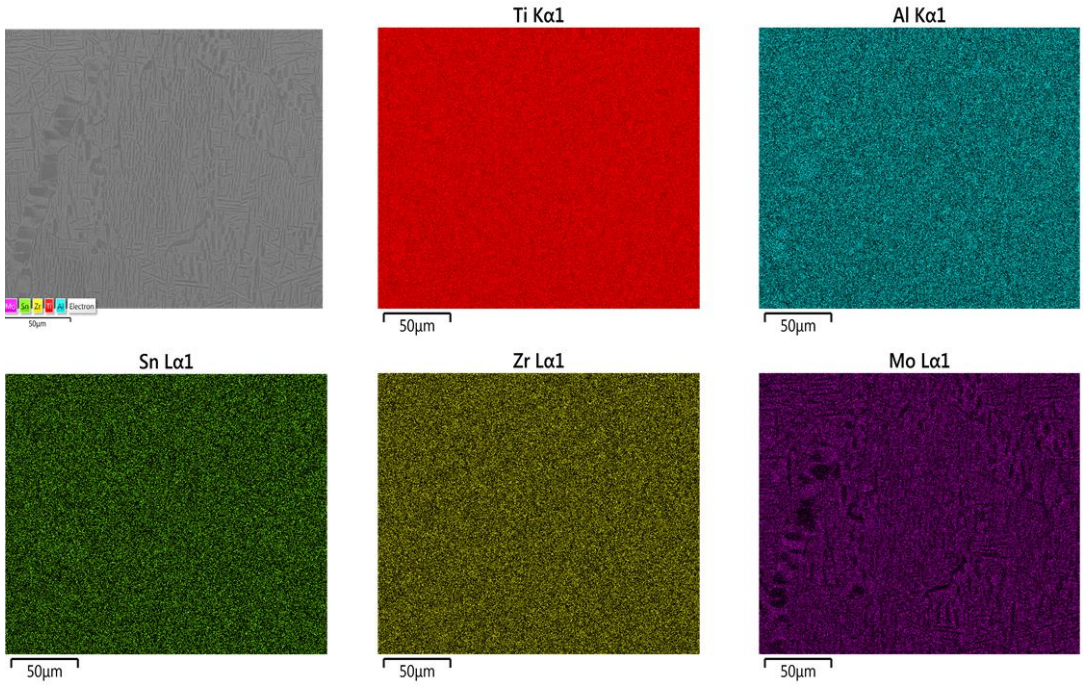

Figure 4.1 EDS maps showing the composition of the base material of the Ti-6246 specimens used throughout this investigation

4.2 Processing Route

Ti-6246 is a solid solution strengthened (α+β) alloy. It is commonly used in elevated temperature aero-engine applications, such as intermediate pressure compressor discs, at temperatures of ~450°C. Rolls-Royce plc. have standardised the processing and heat treatment schedule to optimised property combinations for such applications. Whilst the processing route for the material studied throughout this investigation is proprietary information, a typical processing route for Ti-6246 is shown in Figure 4.2.

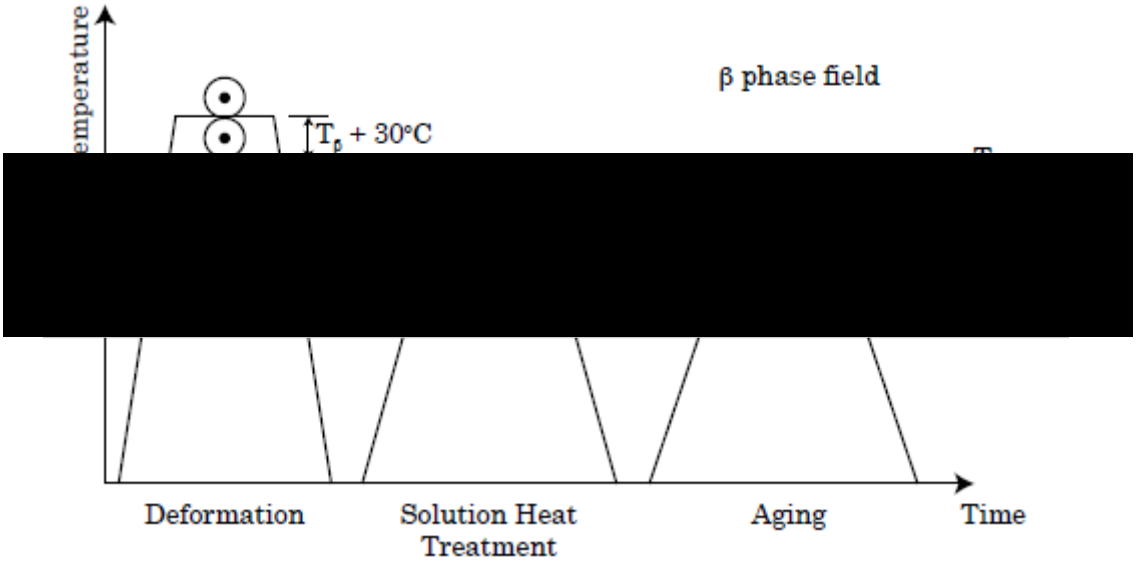

Figure 4.2 Typical processing and heat treatment schedule for compressor disc alloy Ti-6246 [124]

When processed for compressor disc applications, Ti-6246 can undergo final forging 30°C above the β-transus temperature, T_β (935°C), followed by fast cooling via a water quench to prevent recrystallisation of the deformed β grain structure [125]. Performing this deformation process 30-50°C above the β-transus allows control of the β grain sizes. As a result, the β grain size of a fully lamellar microstructure is typically about 600μm [22].

The cooling rate from the β phase field is particularly important as it determines the characteristic features of the lamellar microstructure, such as the α-lamellae/laths size, the α colony size, and the thickness of the α layers at the β grain boundaries [22]. α-laths preferentially form at β grain boundaries but once the boundary nucleation sites are saturated, these α-laths begin to grow perpendicularly from the α lined grain boundary and can result in providing larger effective slip lengths, leading to a reduction in fatigue strength and resistance to crack nucleation [124].

Upon completion of the forging, a solution heat treatment is applied to allow the growth and precipitation of HCP α laths throughout the previously entirely β grain structure. This is accomplished by means of heating 30°C below T_β for 1-2 hours and fan air cooling. In performing the solution heat treatment below 25-85°C below T_β, the alloy is able to obtain an optimum balance between ductility, fracture toughness, creep and stress rupture properties [126].

Lastly, the ageing heat treatment of the alloy between 580-605°C for over 8 hours and cooling it in air to room temperature, allows the precipitation of secondary α, α_s. Once the compressor discs are assembled into drums, using a combination of electron beam welding and mechanical fixtures, the components undergo a post weld heat treatment performed under vacuum conditions [124].

4.3 Microstructure

Ti-6246 is a high strength, highly β-stabilised α+β alloy with the molybdenum equivalent of Mo_{eq}~6%. Ti-6246's composition effectively combines the superior high temperature creep resistance of the α alloys with the improved strength and fracture toughness of the β alloys [127]. Additions of tin and zirconium in Ti-6246 have only slight effects on the transformation temperature but increase heat treatability and strength in comparison to Ti-64 via increased solid solution strengthening. Having undergone supra-transus thermo-mechanical processes (β forging followed by subtransus thermal treatments), the microstructure achieved is a largely transformed, Widmanstätten microstructure [125].

4.3.1 Prior β Grains

β forging at 30-50°C above T_β typically results in a prior β grain size of around 600μm [22]. Using light microscopy, the microstructure of the specimens used throughout this investigation was analysed. The areas of 95 prior β grains were calculated, as shown in Figure 4.3 and in assuming the grains to be circular, the equivalent average circle diameter was approximated to be 711μm.

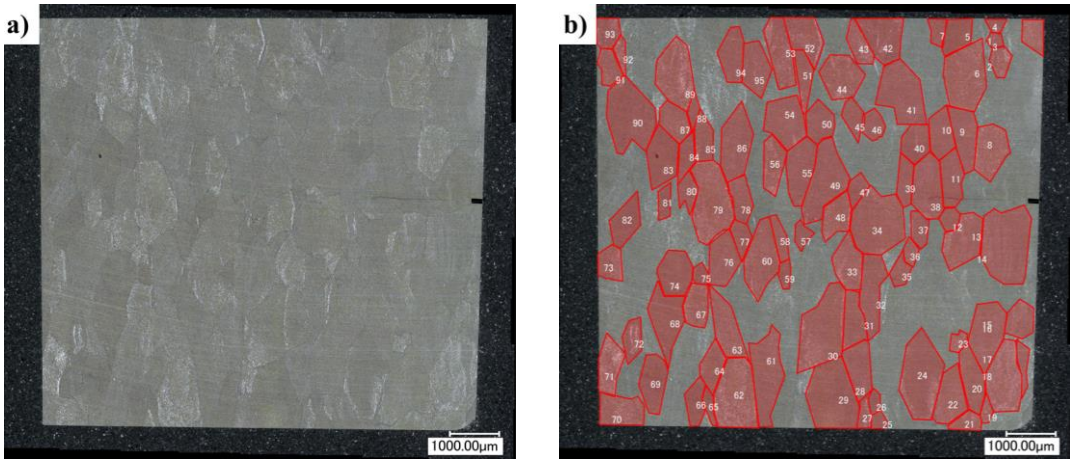

Figure 4.3 a) Micrograph of Ti-6246 using a Keyence b) Prior β grain areas calculated using Keyence software

4.3.2 α Characterisation

Residing within the coarse grain β phase matrix, the microstructure consists of coarse, elongated primary α-lamellae/laths (α_p) measuring between 0.5-2μm in width, as well as much finer secondary α-lamellae/laths (α_s) measuring <0.5μm, as shown in Figure 4.4 [128]. Identified in the remaining β matrix, the finer α_s lamellae creates a bi-lamellar microstructure and greatly benefits a coarse fully lamellar microstructure by reducing the existing slip lengths which has a large impact on the mechanical properties [22].

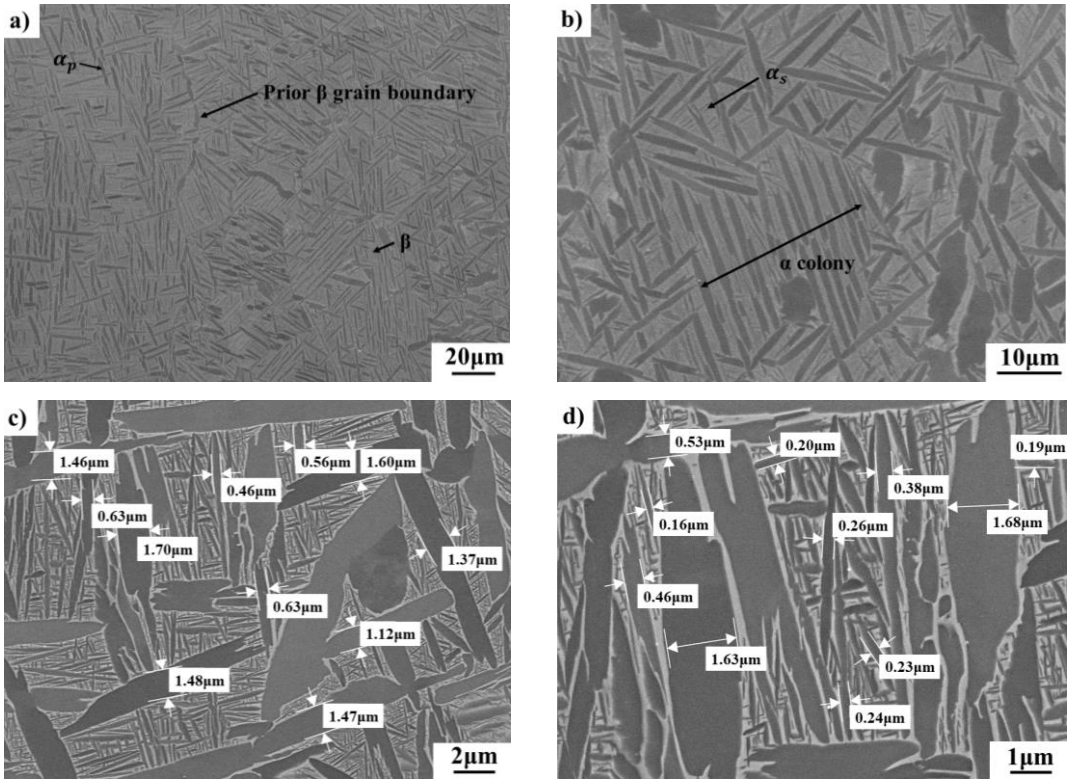

Figure 4.4 Secondary electron (SE) micrographs highlighting microstructural features a) α_p (dark grey), β matrix (light grey), prior β grain boundary, b) α_s in between the α_p, α colony, c) α_p width measurements, d) α_s width measurements

4.4 Specimen Geometry/Identification

The specimens used throughout this investigation are RLH 10042 square corner crack specimens as shown in Figure 4.5. Figure 4.6 shows a 7x7mm cross section and a 20mm parallel gauge length. In order to determine the location of the fatigue crack and to accurately monitor the crack propagation, a 0.35mm starter notched was machined into each specimen.

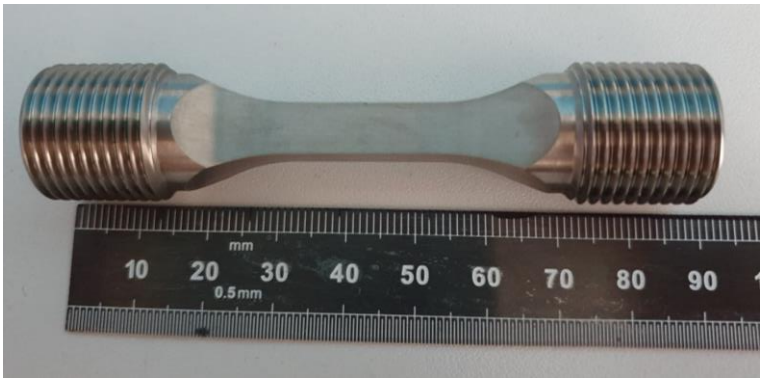

Figure 4.5 Image of Ti-6246 7x7mm corner crack specimens used throughout investigation

The dimensions of the provided specimens are accurate to thousandths of a millimetre. The measurements were confirmed using callipers calibrated to three decimal places in agreement with the calibration requirements outlined by the SMaRT_QS5.4b Calibration Policy (Version 2.2) & SMaRT_QS5.5d Sub-contracted Calibrations (Version 1.12) to ensure accuracy [129][130]. The corner crack measurement was checked using a Keyence optical microscope.

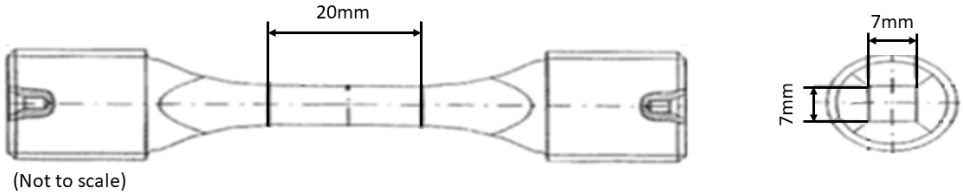

Figure 4.6 Schematic of RLH 10042 specimen.

5 EXPERIMENTAL PROCEDURES

5.1 Previous Setup

Swansea University has seen the development of a TMFCG test facility for characterising the crack growth behaviour of nickel-based superalloy, RR1000 under TMF conditions. The final setup adopted, as shown in Figure 5.1, comprised of the use of an ICS system for rapid heating of the specimen and a single fan cooler to achieve the required cooling rates. The DCPD method was adopted to control and monitor the crack growth and temperature monitoring and control was achieved through spot-welded type-N TCs. This project has seen the evolvement of the previous setup, resulting in a repeatable, reliable TMFCG test facility that is adaptable for the use of different materials.

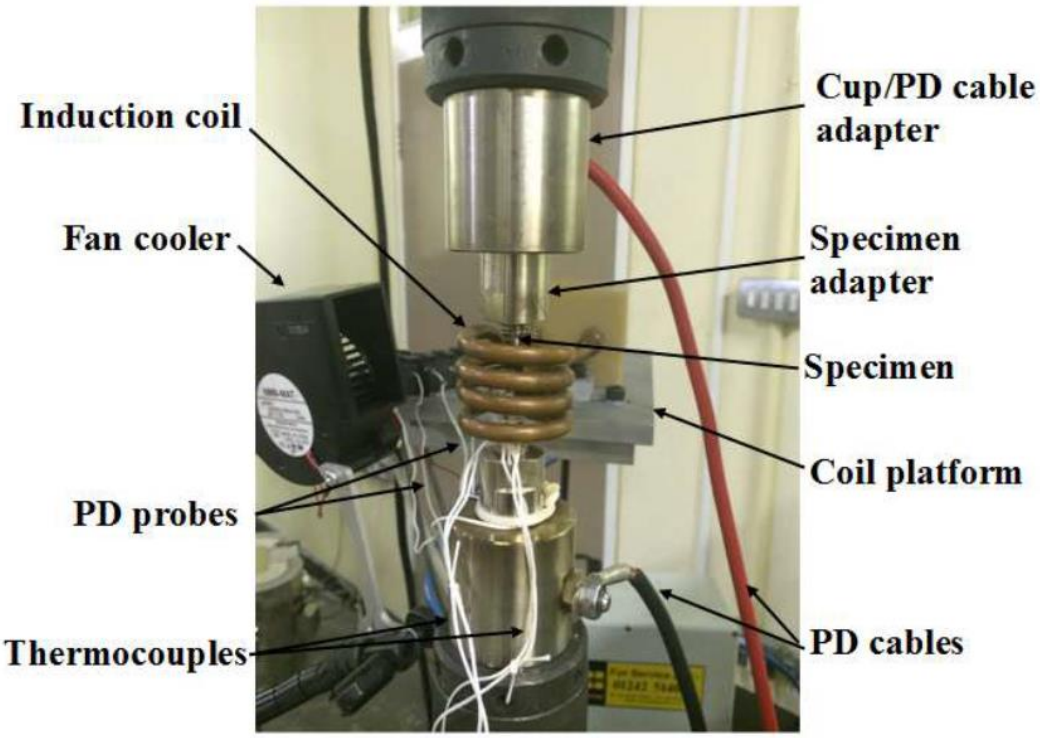

Figure 5.1 Image of previous setup developed at Swansea University, for the testing of TMFCG behaviour in RR1000

5.2 Thermal Profiling

The importance of accurate temperature control and monitoring of the dynamic thermal cycles, required for TMF testing, are emphasised in the current existing standards for strain-controlled testing; ISO12111, and load-controlled testing. The temperature at the centre of the gauge section should be controlled with an accuracy of ±5°C or ±1% or the temperature range ΔT, whichever is greater. The axial temperature gradients within the gauge length should not exceed ±10°C or ±2% of the temperature range [105]. The most important issue in dynamic temperature measurement and control consists in avoiding cold spots at the temperature measurement point due to heat conduction through the TC wires. For induction heating this is particularly important, as the TC is not heated directly by the induction coil, but only indirectly by the specimen [105].

TMFCG specimens require less extensive thermal profiling than strain lifing TMF as the area of interest is localised around a ±2mm area axially above and below a starter notch, whereas up to 25mm gauge sections require profiling during strain lifing TMF. However thermal profiling is still significant in TMFCG enabling the correct conditions and phase angles to be accurately investigated. Various coil designs and cooling methods have been investigated to provide the most appropriate balance between axial and radial thermal gradients, desired heating and cooling rates as well as best line of sight towards the fatigue crack starter notch, enabling additional investigations such as preferential crack tip heating to be conducted.

Pre-test verification of the test setup was conducted, and a thermal profile was recorded. This was achieved by isolating the temperature and recording the thermal cycle using type-N spot-welded TCs. As per the standard, it was ensured that whenever used, the TCs were spot-welded less than 1mm apart and were not overlapping, as shown in Figure 5.2 [105].

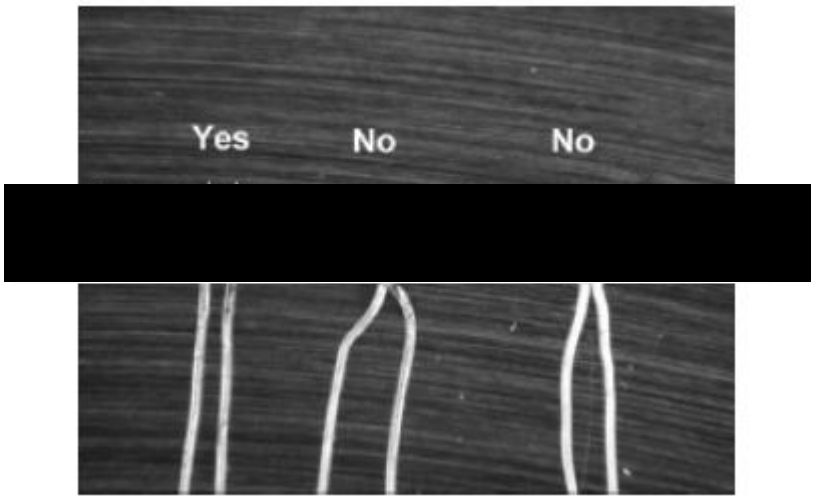

Figure 5.2 Image illustrating the correct spot-welding of a TC [105]

A total of twelve type-N TCs were welded to the gauge of the specimen, as shown in Figure 5.3. TCs C1-C4 were located at the centre of each face, in the crack plane. T1-T4 and B1-B4 were placed 2mm above and below the centre TCs, respectively. The thermal profiling specimen is shown in Figure 5.4.

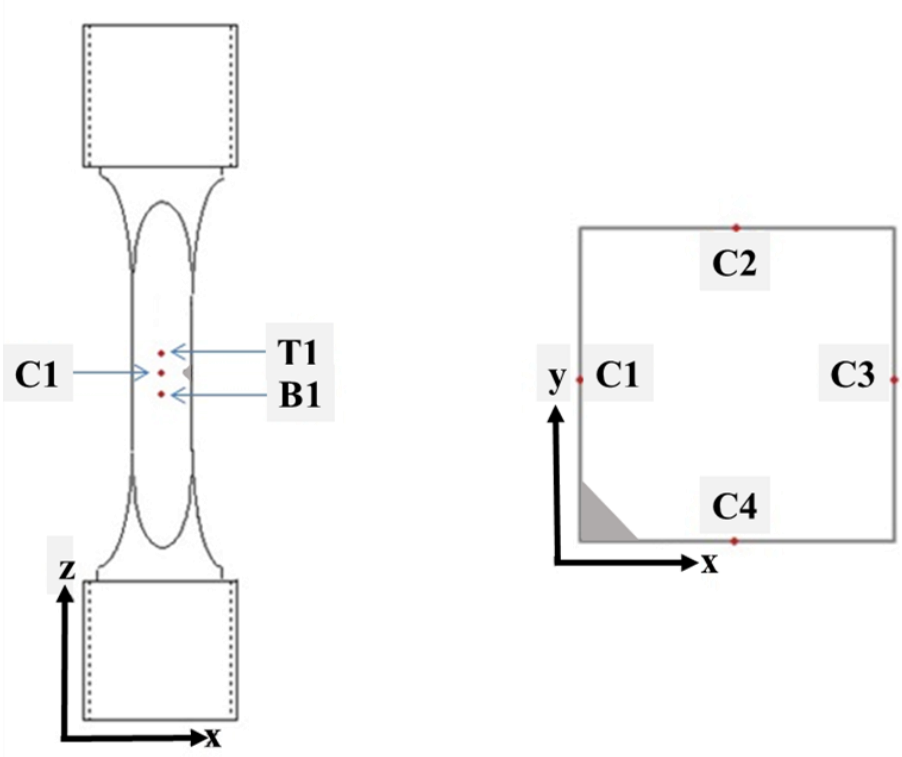

Figure 5.3 Schematic illustrating the TC locations for thermal profiling, in the x-z and x-y planes

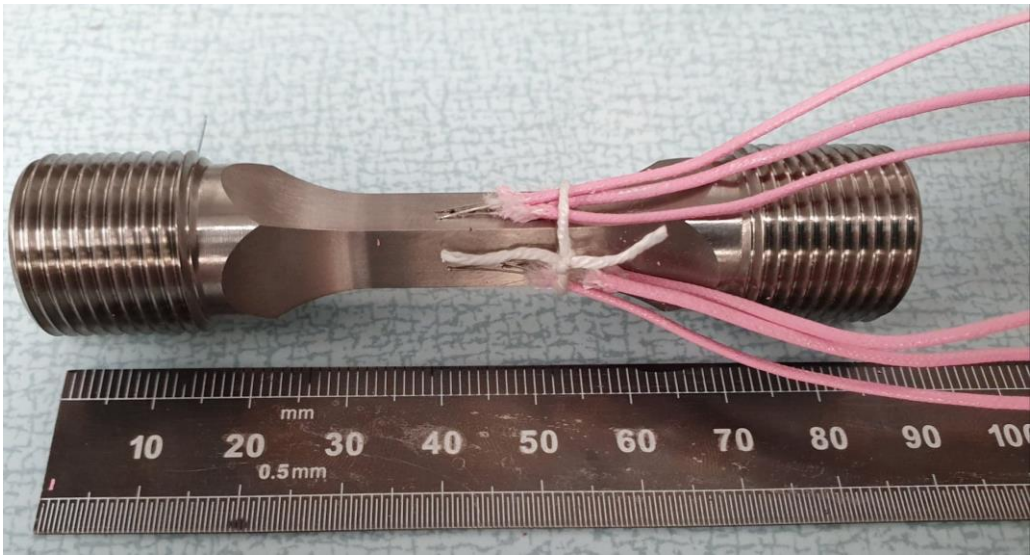

Figure 5.4 Image of Ti-6246 7x7mm corner crack specimen with type-N TCs spot-welded to the gauge for thermal profiling

The specimen was held at the maximum test temperature for a minimum of 30 minutes, before temperature recording was conducted. This was to ensure the specimen had time to heat up uniformly and the temperature had settled.

The thermal profiling cycle used was the same as that used for the TMFCG testing; 80 seconds in duration with the temperature dynamically cycling from the minimum test temperature, 200°C to the maximum test temperature, either 500°C or 550°C. Using the Dirlik DCPD-TMF software, the temperature was monitored and recorded continually throughout the thermal cycling of the specimen, with TC C1 acting as the control in each profile measured.

5.3 Heating Methods

Development of a testing facility for crack propagation testing under TMF loading is a relatively recent requirement from the industrial sector, particularly in titanium alloys, and has mainly been driven by the increased operating temperatures required by the gas turbine industry.

A conventional radiant furnace is unable to produce the rapid thermal cycles required during TMF testing. It was therefore important to ensure a viable alternative was used. Induction heating has proven a popular choice for TMF testing, being employed in several institutes, as it is able to provide rapid thermal cycles and can be used under both load and strain-controlled testing [95].

5.3.1 Induction Coil Comparison

The importance of coil design has been highlighted by Evans et al. [101] and the resultant thermal gradients have been explored by Beck et al. [108]. The same authors highlight concern with current interference when combining induction heating with crack monitoring techniques such as the DCPD method. It was therefore an important part of this investigation to compare ICS and ensure the most suitable was adopted for the use in the final setup. In total, thermal profiling was conducted on five different ICS. The method of thermal profiling is outlined in 5.2. Each ICS was subject to a thermal cycle of 200-500°C.

With the ability to load/unload the specimen with minimum disruption to the test setup, the original preferred design is shown in Figure 5.5 a). Such design not only allows for easy improvement to test repeatability, but also allows for good scope and accessibility to the corner crack, thus making it possible to integrate an infrared camera into the setup or even adapt the setup for strain-controlled/strain-monitored testing. The dynamic temperature deviation from the control TC, for the preferred transversal field split helical coil is shown in Figure 5.5 b).

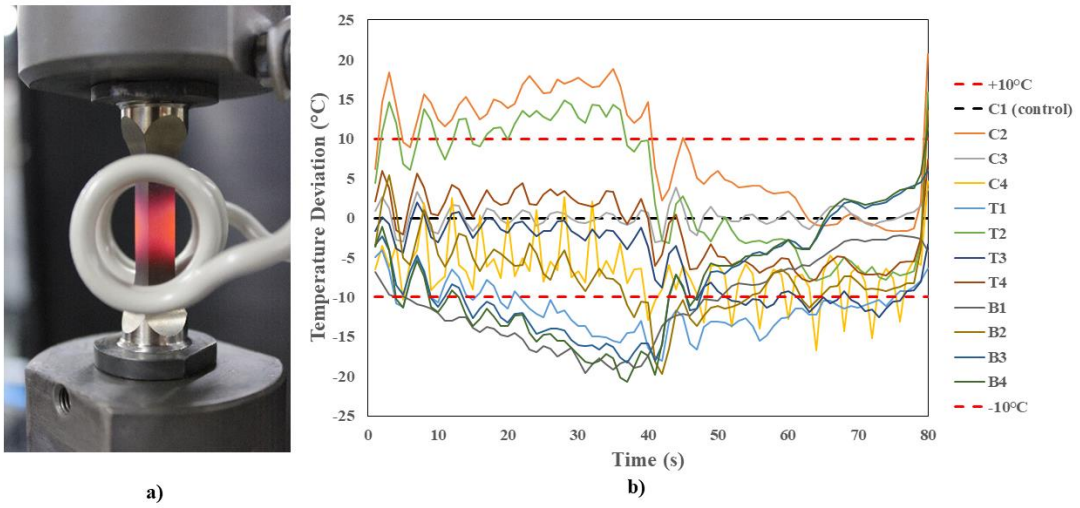

Figure 5.5 a) Transversal field split helical coil b) temperature deviation from the control TC, C1

Figure 5.5 b) shows there is a temperature gradient across the specimen during dynamic heating with the transversal field split helical coil, with a number of the TCs displaying a deviation of more than ±10°C from the control TC. However, as well as good scope for an infrared camera, the coil does not pose as an obstruction, allowing for more uniform cooling to take place.

In an attempt to reduce the temperature gradient experienced during the heating phase of the dynamic temperature cycle, the shift towards a more uniform coil was made, as shown in Figure 5.6 a). Figure 5.6 b) shows more uniform heating and cooling is achieved with the uniform multi-turn longitudinal field helical coil, with a lower proportion of the TCs displaying a temperature gradient greater than ±10°C. It is likely that this temperature gradient could be further reduced with more adjustments to the coil position, however, the lack of space between the turns makes for an unfavourable choice of coil in this setup. The poor scope of the crack plane limits the setup's capabilities, removing the opportunity to implement an infrared camera or extensometers for strain-controlled testing.

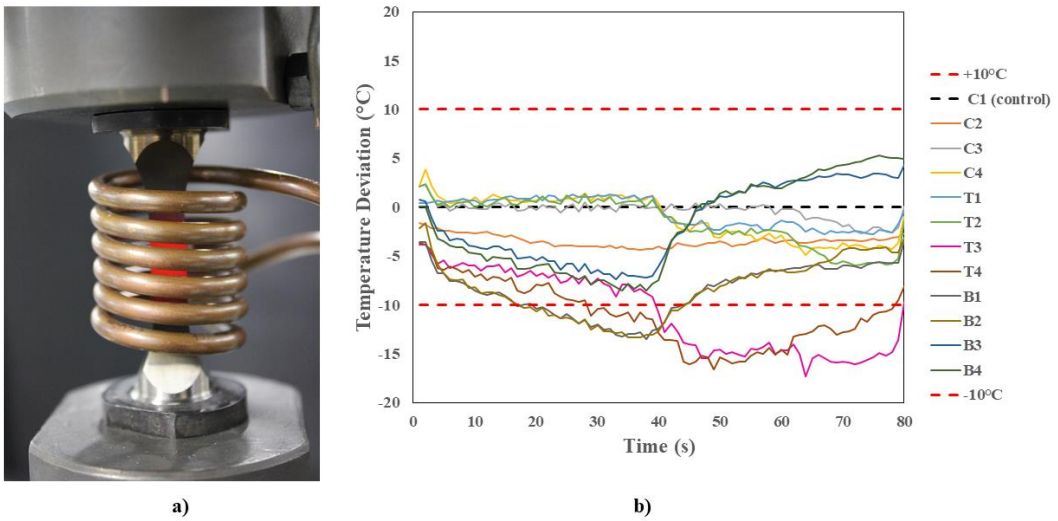

Figure 5.6 a) Uniform multi-turn longitudinal field helical coil b) temperature deviation from the control TC, C1

Figure 5.7 a) shows the move towards a non-uniform multi-turn longitudinal field helical coil, with the thoughts of integrating an infrared camera into the setup in mind. The temperature deviation displayed in Figure 5.7 b) shows a good thermal profile is achievable with such coil. However, it was found that not only does the centre turn interfere with the visibility of the crack plane, but the coil itself proved too powerful resulting in additional heating of the locking rings and cups. This excessive heating was thought to also pose a risk to the infrared camera and cooling technology and thus the coil was not used in the final setup.

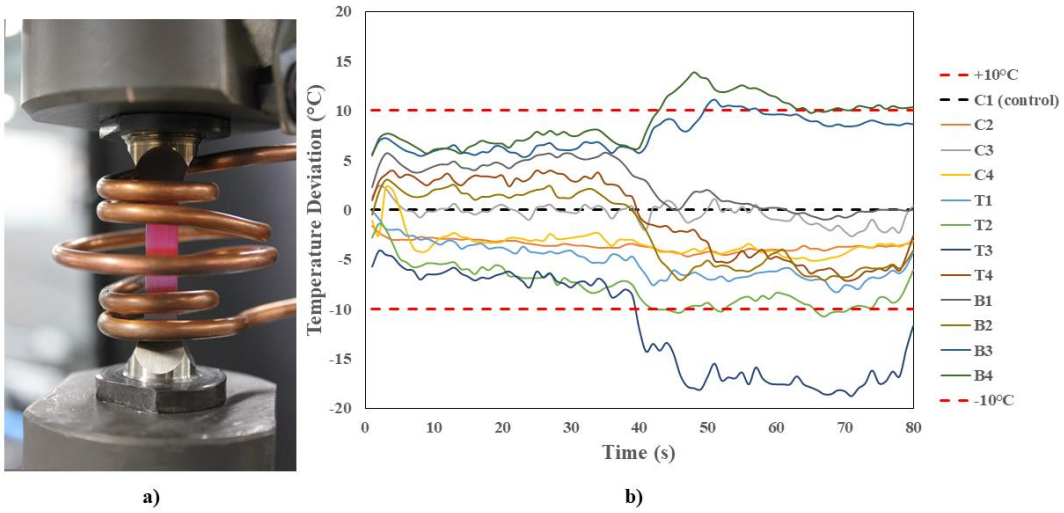

Figure 5.7 a) Non-uniform multi-turn longitudinal field helical coil b) temperature deviation from the control TC, C1

In TMFCG testing, only a small area of the specimen is of interest; the crack plane and thus the use of a more localised coil was investigated. Figure 5.8 a) shows a longitudinal field helical coil with less turns than the previous coils investigated, which can be seen from the heated specimen, the area of heating is more localised around the crack plane. However, the temperature deviation displayed in Figure 5.8 b) shows that this coil design results in severe temperature gradients, where the top and bottom turns are not complete. It is also evident that this design, whilst focusing the heating on the area of interest, it also obstructs the view of the crack plane.

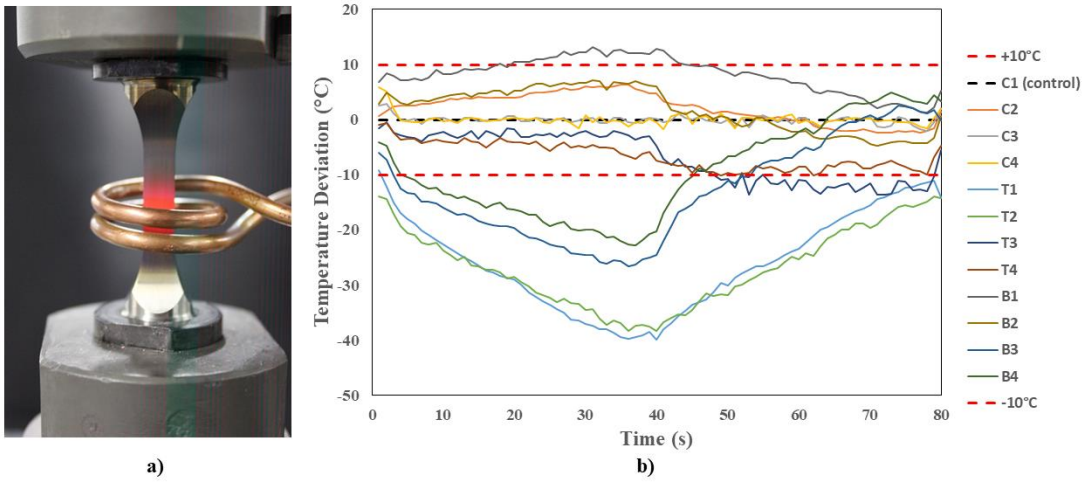

Figure 5.8 a) Non-uniform longitudinal field helical coil b) temperature deviation from the control TC, C1

The final ICS investigated was a non-uniform multi-turn longitudinal field helical coil, as shown in Figure 5.9 a). The increased spacing size of the centre turn allows for good visibility of the crack plane, without having any adverse effects on the temperature distribution of the specimen, as shown in Figure 5.9 b). The ICS shows uniform heating, with little temperature deviation, however, the shielding of the ICS increases the difficulty of the cooling cycle. Although this ICS does provide a less desired cooling profile than some of the other ICS investigated, the temperature deviation is less than ±10°C throughout the cycle and the other benefits of this coil outweigh any drawbacks. Thus, the ICS shown in Figure 5.9 is the one that has been used in the final setup of this investigation.

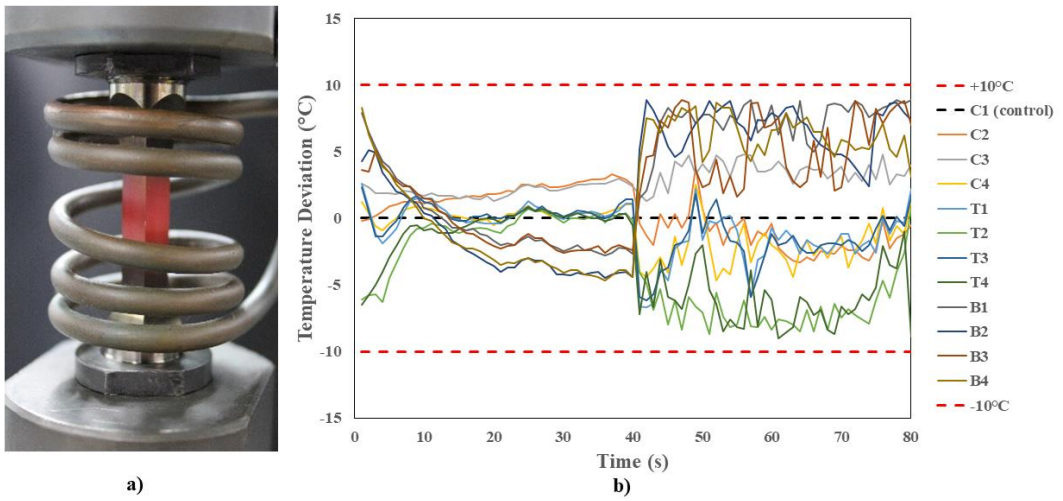

Figure 5.9 a) Non-uniform multi-turn longitudinal field helical coil b) temperature deviation from the control TC, C1

It is clear from this investigation, that and Beck et al. [108] and Evans et al. [101] were correct to highlight the importance of induction coil design, and it is also clear that choosing the best suited ICS is a long and thought-out process.

5.3.2 Isothermal Profile Comparison

A conventional radiant split furnace is unable to provide the desired dynamic thermal cycles required during TMF testing. In order to determine the ICS as a viable heating method, an isothermal comparison between different heating methods was conducted as a part of this investigation. It was therefore deemed necessary to establish a temperature profile of the specimen under isothermal conditions.

As part of this study, two ICS were investigated; that displayed in Figure 5.5 a) and that displayed in Figure 5.9 a). Figure 5.10 shows that, with the transversal field split helical coil (Figure 5.5 a)), that when held isothermally at 500°C, the temperature deviates ±6°C across the critical volume of material.

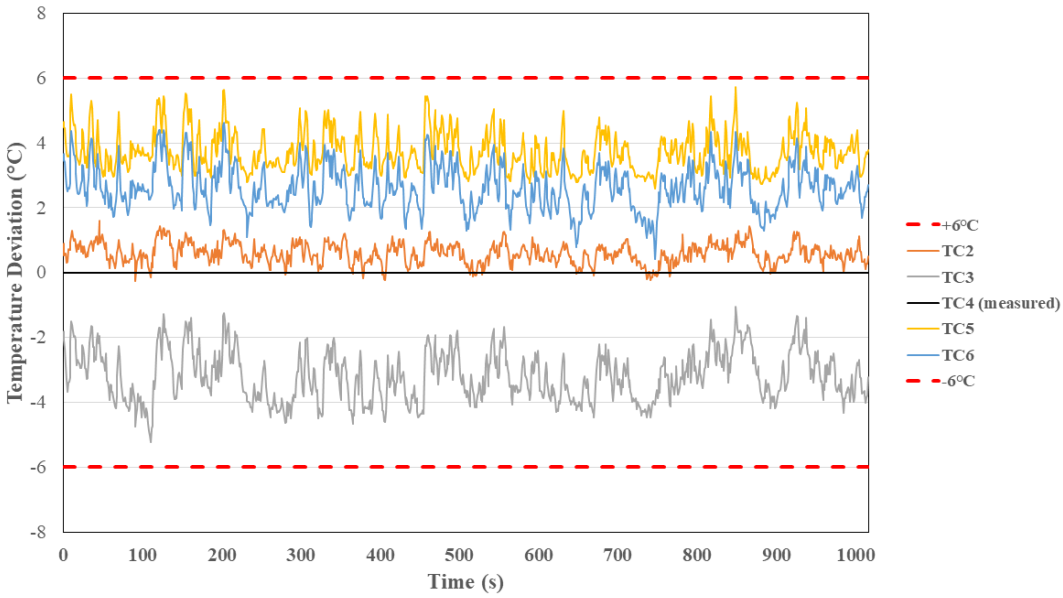

Figure 5.10 Isothermal temperature deviation from the measured TC, associated with transversal field split helical coil, showing spread of ±6°C in temperature across the critical volume of material around the crack and TC location

Shifting to the use of a non-uniform multi-turn longitudinal field helical coil, as shown in Figure 5.9 a), it was possible to achieve a more uniform thermal profile under isothermal conditions. Figure 5.11 shows the coil achieves a much smaller temperature gradient within ±3°C, and is within tolerances outlined in the validated code of practice for strain-controlled TMF testing [105].

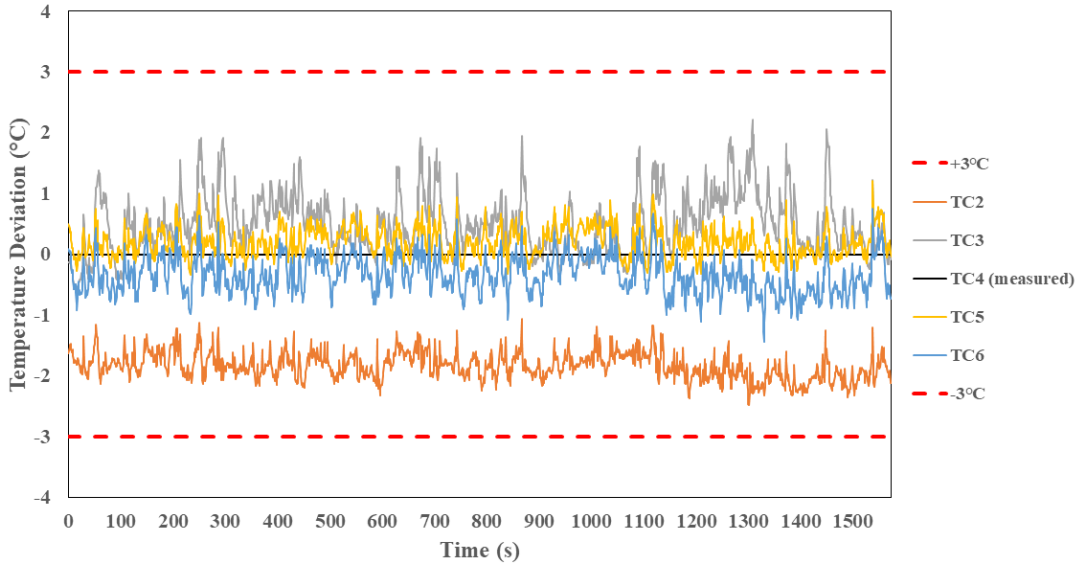

Figure 5.11 Isothermal temperature deviation from the measured TC, associated with non-uniform multi-turn longitudinal field helical coil, showing spread within ±3°C in temperature across the critical volume of material around the crack and TC location

5.3.3 ICS Current Interference

As previously mentioned, concerns with coupling the DCPD method with induction heating have been raised, as it has been thought that the eddy currents produced from the ICS may cause interference with the current required for the DCPD method [101][108]. The orientation of both TCs and DCPD probes can affect the electromagnetic field and thus affect the output. However, unlike TCs, the DCPD probes can only be attached in one orientation, north and south of the starter notch.

A comparison between the DCPD responses using the transversal field split helical coil and the non-uniform multi-turn longitudinal field helical coil is shown in Figure 5.12. As shown, the noise and stability of the DCPD readings was steady when the current was both on and off in the non-uniform multi-turn longitudinal field helical coil. However, it is shown that this was not the case with the transversal field split helical coil which uncovered significant noise. The noise and stability of the DCPD was observed to be at its worst during the heating stages of the thermal cycle when the most power was required from the ICS.

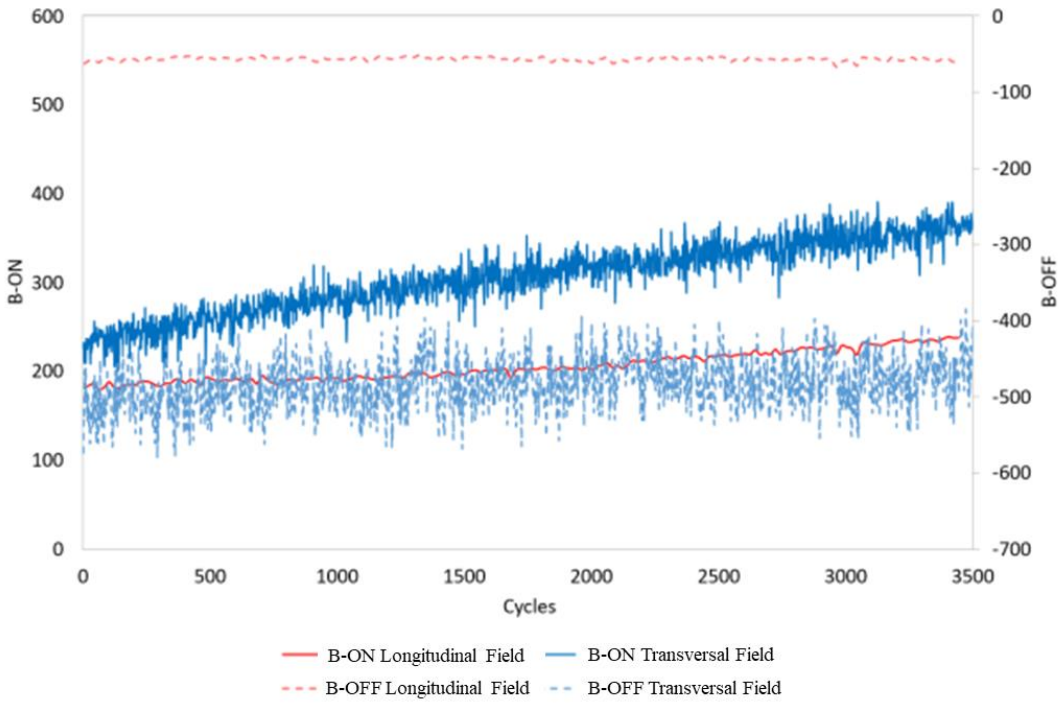

Figure 5.12 Comparison of the DCPD reading stability between the transversal field split helical coil and the non-uniform multi-turn longitudinal field helical coil

5.3.4 Radiant Lamp Furnace (RLF)

With the use of existing facilities in Swansea University [107], a setup using a second generation RLF, designed in collaboration with Severn Thermal Solutions Ltd, was adapted for TMFCG testing. The 12 kW RLF is a standard split body design with each half containing three horizontally mounted lamps. The external surface of the RLF is coated black with araldite to avoid any reflective radiation complications with temperature control via an infra-red thermography camera. Specifically designed to accommodate both an extensometer and a non-invasive temperature measurement device, the setup itself was adapted to also accommodate temperature control using type-N thermocouples. Three independently controllable heating zones allow for accurate temperature control and profiling, whilst built-in internal compressed air cooling delivers rapid cooling rates required by the complex TMF waveforms. The setup used is shown in Figure 5.13.

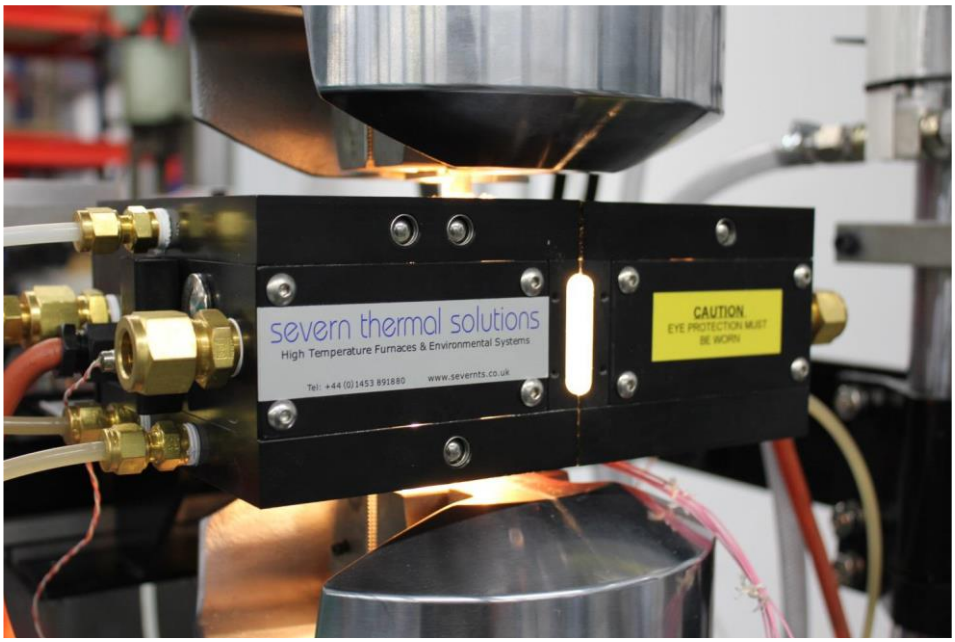

Figure 5.13 Image of the RLF setup adapted for the use of TMFCG testing

5.3.5 Thermal Profile Comparison of TMF Heating Methods

As the induction heating process results in heat being generated inside the specimen itself, it is likely the specimen is uniformly heated throughout during the rapid heating cycle required for TMF testing. However, this is not the case when using a RLF, which relies on heat conduction and thus results in the possibility for thermal gradients during the thermal cycle. To determine such effects, thermal profiling was conducted using both the ICS and RLF. In order to do this, four type-N thermocouples were spot-welded to the centre of each face and one contact type-N thermocouple was placed longitudinally through the specimen to the centre plane by means of a 1mm hole.

As anticipated, Figure 5.14 a) shows that uniform heating is achieved with the ICS and Figure 5.14 b) shows that a temperature gradient from the surface to the centre of the specimen does exist when dynamically cycling the temperature using the RLF. This exercise also highlighted that external forced air cooling, in both cases, also results in a temperature gradient, with the centre of the specimen cooling much slower. This issue is resolvable by increasing the cycle time and thus allowing more time for the specimen to reach a uniform temperature throughout. However, as the area of importance is the crack tip in TMFCG testing, the thermal gradient between the surface and the centre of the specimen does not pose a detrimental issue. It does though, further highlight the complexity of TMF testing, with the cooling section of the cycle proving more difficult to achieve than the heating section.

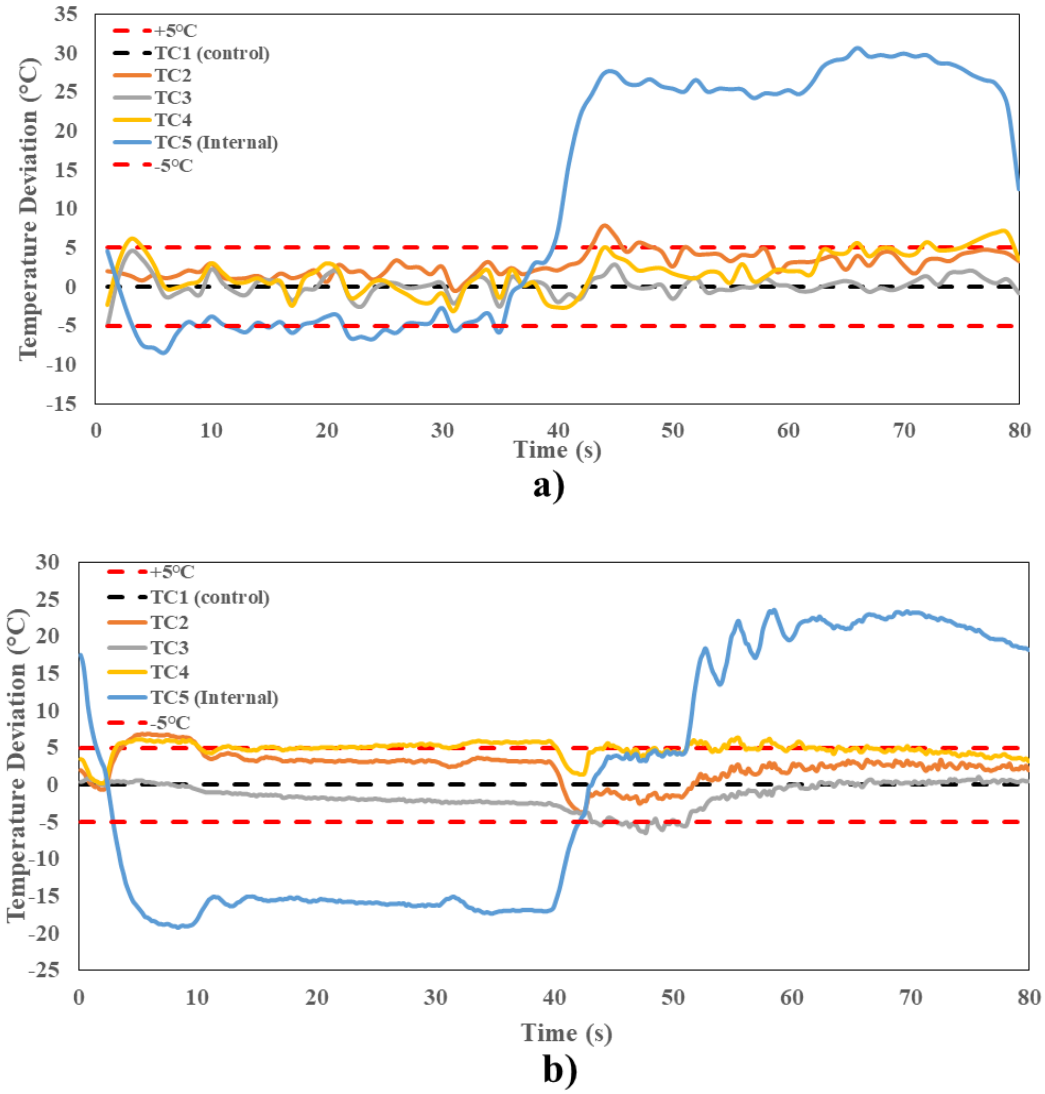

Figure 5.14 Temperature deviation from the control TC over the period of an 80 second cycle using a) ICS and b) RLF, showing a temperature gradient upon cooling of the specimen in both cases

5.4 Cooling Methods/Apparatus

The previous setup utilised a single fan blower, as shown in Figure 5.1, to achieve the required cooling rates. Designed using RR1000 specimens, the fan blower was successful in achieving the desired cooling rate of 10°C/s and was therefore, implemented into the initial setup design used throughout this investigation.

However, it quickly became apparent that the single fan blower, as shown in Figure 5.15, did not provide enough cooling to the Ti-6246 specimens. Nickel alloys are known to possess a thermal conductivity of around 10-12 W/mK [131], whereas the thermal conductivity of titanium alloys is much lower with a value of 7.6 W/mK for Ti-6246 at room temperature [132]. The lower thermal conductivity of Ti-6246 may be the cause for the inability to achieve the same cooling rates with the single fan blower, as achieved in the previous setup. This revelation resulted in other cooling methods being explored.

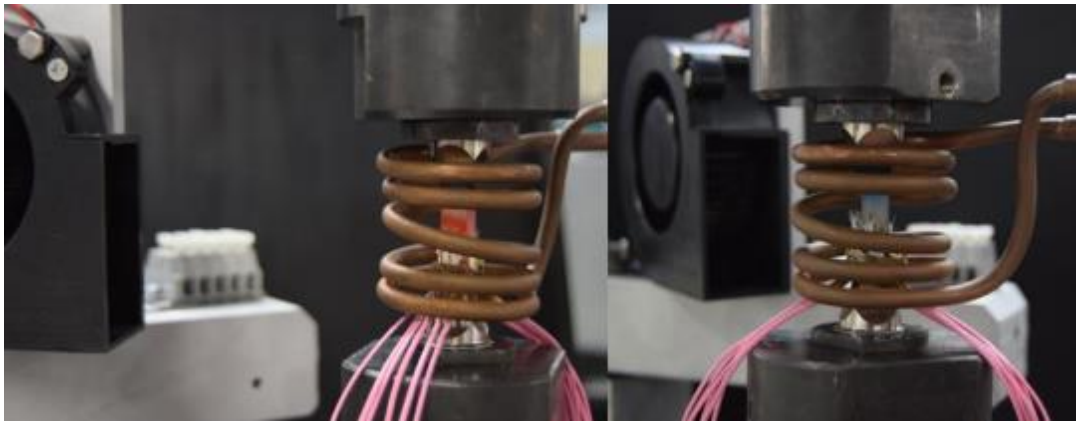

Figure 5.15 Image of TMFCG setup utilising a fan blower

5.4.1 Selection of Cooling Apparatus

To provide rapid, uniform cooling, the shift towards the use of forced air amplifiers was made. Air amplifiers are annular units that work by releasing a small amount of compressed air through an adjustable circular slot inside the air amplifier. This compressed air draws in air from the back of the amplifier which travels downstream, entraining surrounding air and creating an amplified airflow that can provide low noise, energy efficient cooling. An operational schematic is shown in Figure 5.16 [133].

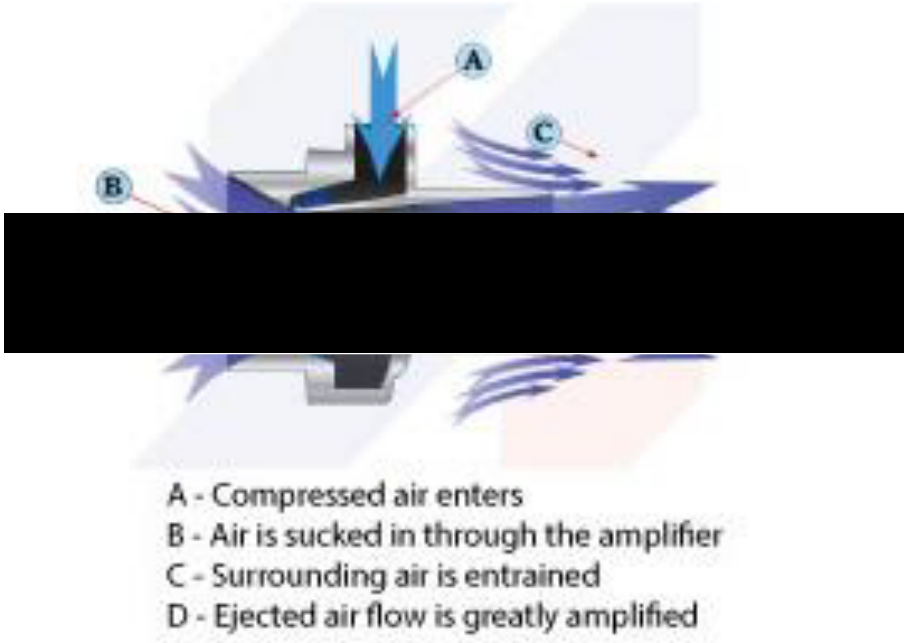

Figure 5.16 Schematic illustrating the operation of an air amplifier [133]

Four Meech air amplifiers were integrated into the test setup, as shown in Figure 5.17. Figure 5.17 shows the initial method of implementation involved the use of adjustable magnetic arms. However, with this setup, it was not possible to obtain a repeatable, reliable positioning of the forced air cooling.

Figure 5.17 Image of the original implementation of air amplifiers. Each air amplifier has a separate compressed air feed and is held in position with an adjustable magnetic arm

The cooling platform shown in Figure 5.18 was designed to enable repeatable positioning of the air amplifiers, and hence repeatable, uniform cooling was achieved. The platform design also reduces the number of outlet ports from the compressed air supply from four to one, with air being directly fed into the platform, feeding all four amplifiers. This contrasts with the original installation, which entailed each amplifier being individually connected to the compressed air supply.

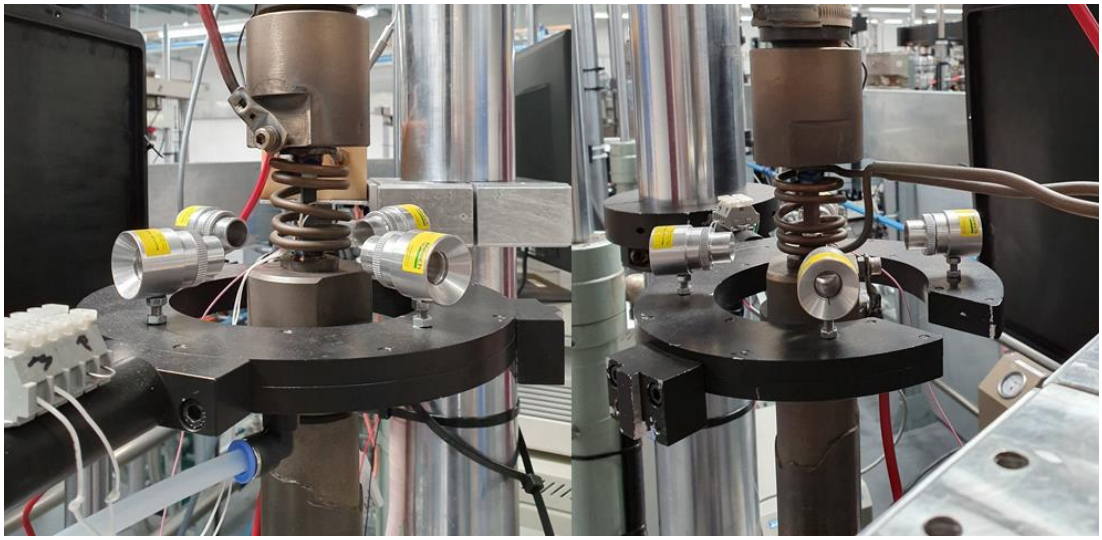

Figure 5.18 Image of bespoke cooling platform designed for the TMFCG setup used throughout this investigation

As shown in Figure 5.18, the platform also provides a useful positioning of the DCPD unit, and a purpose-built platform for an infrared camera.

5.4.2 Comparison of Cooling Apparatus

With the ability to adjust the pressure of air supplied to the air amplifiers, it is possible to increase/decrease the amount of cooling supplied to the specimen and thus provides a more adaptable method of cooling. The cooling rate achieved by the four air amplifiers are compared to that achieved by the single fan blower and that of air cooling (coil only). This comparison is shown in Figure 5.19.

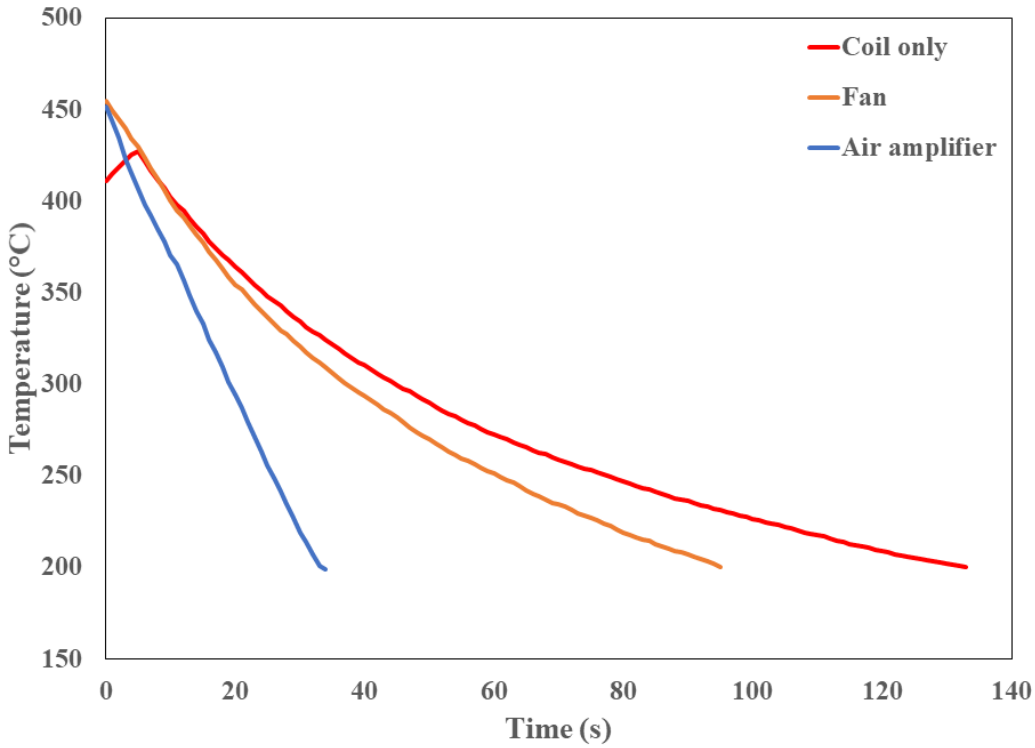

Figure 5.19 Comparison of cooling rates achieved with no external cooling (coil only), fan cooling and air amplifiers

5.5 Infrared Thermography Camera

5.5.1 Localised Crack Tip Heating

One of the controversies regarding induction heating for crack propagation testing is the influence of crack tip heating, which has frequently been seen as a potential setback of this type of testing [134]. It became apparent early on that TC measurement would be inappropriate for this investigation. The localised measurement of temperature does not provide appropriate information for a growing crack and therefore, the issue was investigated using an infrared thermography camera (IRTC).

Measurements were made in the final ICS setup, used for this TMFCG investigation, with the crack plane in the test specimen held at a constant temperature of 500°C, as measured by a spot-welded type-N TC. These measurements were taken slightly ahead of the crack tip to avoid interference from the crack section. It was thought the isothermal condition represents the extreme cases, where power is continually provided through the ICS.

Figure 5.20 shows a thermographic image of the test specimen and provides a longitudinal profile of temperature measured graphically. The data provided slightly ahead of the crack tip clearly shows that the air in the crack as it is held open is heated as expected, but there is no non-uniformity in the temperature distribution across the material, indicating no effect of crack tip heating.

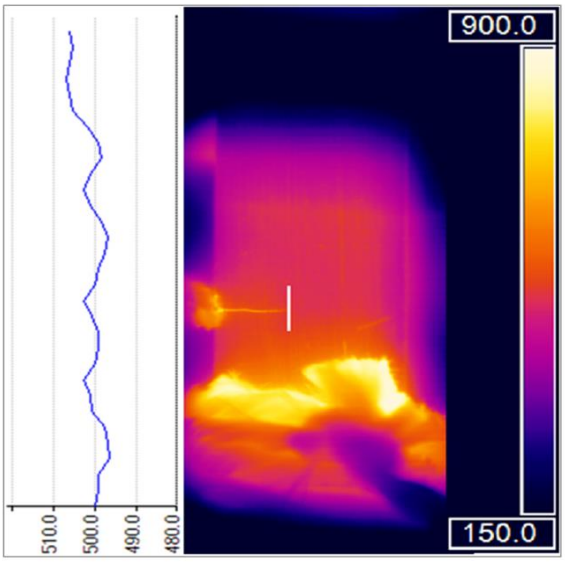

Figure 5.20 Thermographic image of Ti-6246 with the crack plane at 500°C. The longitudinal profile indicates no effect of crack tip heating

5.6 Crack Monitoring and Crack Calibration

The DCPD method has been adopted for crack monitoring throughout this investigation. This has been done so by attaching probe wires, made from hard tempered platinum wire (0.5mm diameter), to either side of the starter notch, as shown in Figure 5.21.

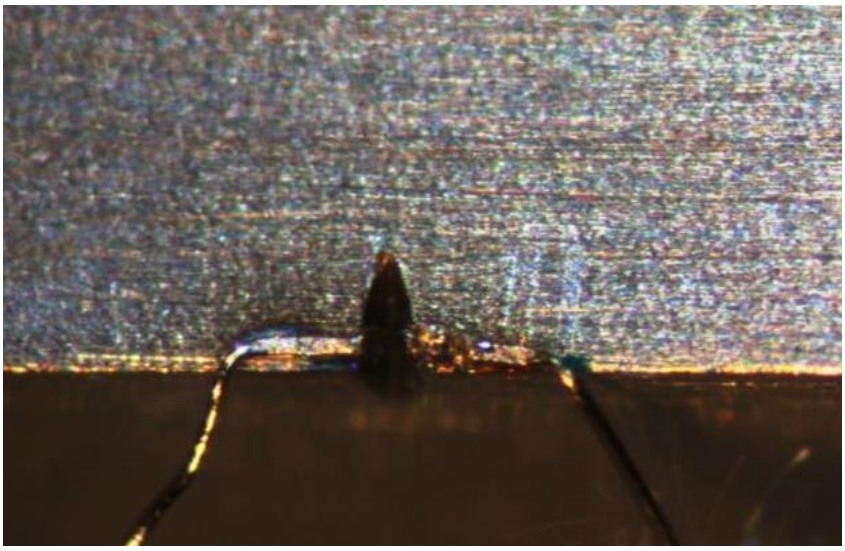

Figure 5.21 Image of DCPD probe wires spot-welded to either side of the starter notch

The crack growth was measured and recorded in μV by the Dirlik DCPD-TMF software during the test. Post-test, the fracture surface was analysed using the Keyence optical microscope, and 11 measurements were taken of the fatigue crack, as shown in Figure 5.22. The resulting crack length was taken to be the average from the 11 surface measurements made. This process of measuring was conducted for both the pre-crack growth and the test crack growth.

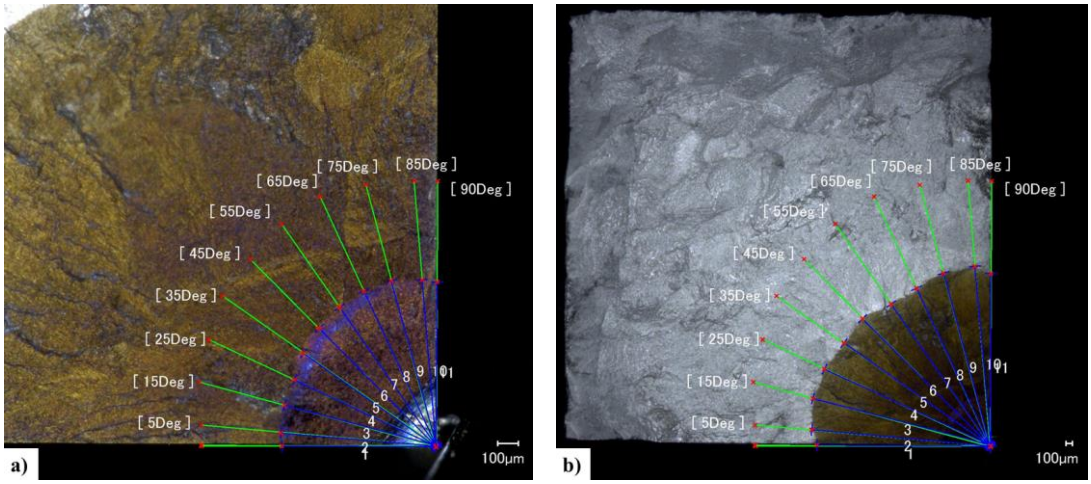

Figure 5.22 Image of measurements taken from the fracture surface a)higher magnification to so show pre-crack and b) lower magnification to show total crack length

In measuring the crack growth post-test, it was possible to correlate such growth as a unit of length with the growth in µV. Thus, it became known that for 150µV under the pre-cracking conditions, ~0.78mm of crack growth occurred and for 950µV, the final crack length was ~2.8mm.

5.6.1 Multiple Crack Initiations

Despite the presence of a pre-existing corner crack, the spot-welded TCs located within the gauge length still proved problematic, resulting in the occurrence of multiple crack initiation sites, as can be seen in Figure 5.23. The spot-welding of TCs to the specimen can create an area of stress concentration and regardless of the pre-existing defect, it is evidenced that caution is still required.

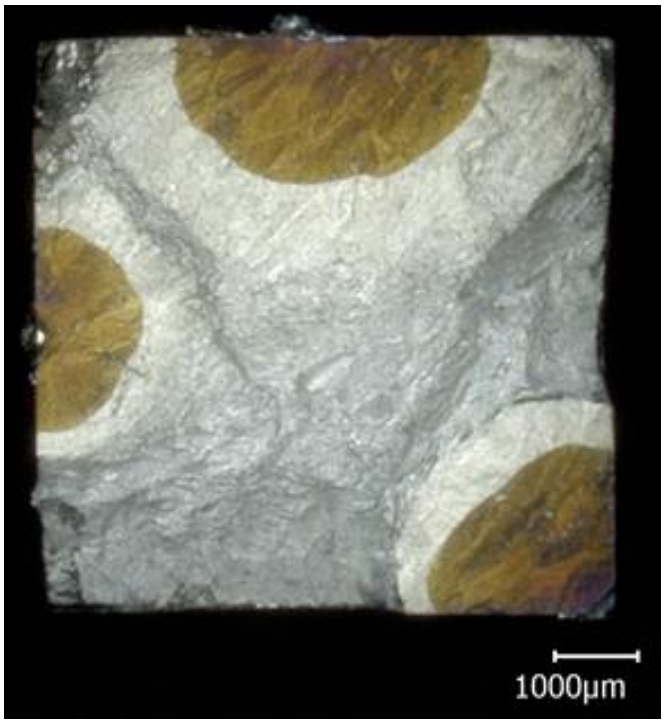

Figure 5.23 An optical image displaying multiple crack initiation sites caused by welded TCs

TCs were originally being attached to the gauge of the specimen using a spot-welding voltage of 8V. To alleviate the occurrence of fatigue cracks initiating from TC locations, this was reduced to 4V. The development of a pre-cracking procedure was also required to rectify this issue.

5.6.2 Pre-cracking Procedure

To ensure the crack initiated from the starter notch, and that no residual effects from machining impacted on the test, an initial pre-cracking stage was essential to the test procedure. The initial pre-cracking procedure adopted is outlined in Table 5.1. The test specimen was pre-cracked with TCs attached (required for the TMF test) and was conducted at the maximum test temperature. However, this procedure contributed to the development of multiple crack initiation sites, namely from the TC locations. Thus, the pre-cracking procedure was modified to eliminate such issue. The finalised 3-stage load-shedding pre-cracking procedure, shown in Table 5.2, was conducted at room temperature and without TCs. Spot-welding the TCs post pre-cracking, as well as pre-cracking at room temperature was necessary to lessen the likelihood of multiple crack initiation sites. The pre-cracking frequency was also altered with the initial stage frequency of 5Hz being reduced to 2Hz. As shown in Table 5.2 Final pre-cracking procedure used for this investigation, with amendments highlighted in red the total pre-crack growth was also increased from 80µV to 150µV.

Table 5.1 Initial pre-cracking procedure

Stage	Load (kN)	R	Frequency (Hz)	Temperature (°C)	Growth (µV)	Waveform
1	30	0	5	T_{MAX}	10	Sine
2	27.5	0	1	T_{MAX}	20	Sine
3	25	0	0.25	T_{MAX}	50	Sine

Table 5.2 Final pre-cracking procedure used for this investigation, with amendments highlighted in red

Stage	Load (kN)	R	Frequency (Hz)	Temperature (°C)	Growth (µV)	Waveform
1	30	0	2	RT	25	Sine
2	27.5	0	2	RT	50	Sine
3	25	0	1	RT	75	Sine

5.7 Final Setup

The final setup used for the purpose of this TMFCG research includes an ESH 100kN servo-hydraulic test machine with a ZwickRoell control cube servo controller and Cubus software system. Application of the thermal cycle was achieved using an internally water-cooled induction coil for heating and four Meech air amplifiers were used to provide sufficient, uniform cooling. Using type-N thermocouples, the temperature was controlled and monitored through Dirlik DCPD-TMF software. Crack monitoring was conducted using the DCPD method. This method has been tested and proven acceptable for monitoring crack propagation and thus, has been adopted for this research and is monitored through Dirlik DCPD-TMF software [91]. The final setup is shown in Figure 5.24.

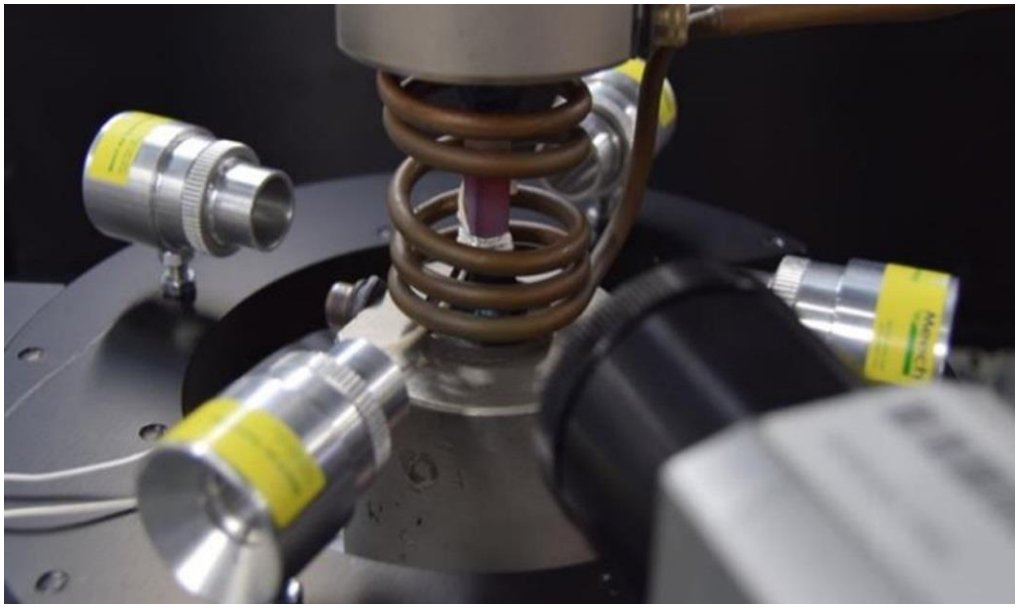

Figure 5.24 Image showing the final setup used for the TMFCG testing conducted throughout this investigation.

As shown, a non-uniform multi-turn longitudinal helical field induction coil is adopted for the heating and four air amplifiers, situated on a platform are used for the cooling. A type-N TC is spot-welded to the gauge of the specimen for temperature control and monitoring and platinum PD wires spot-welded for crack monitoring.

5.7.1 Final Thermal Profile

With the finalised setup, the final thermal cycles 200-500°C and 200-550°C were recorded. Given in Figure 5.25 is the response of the monitoring TCs over a single 80 second cycle for a temperature range of 200-500°C.

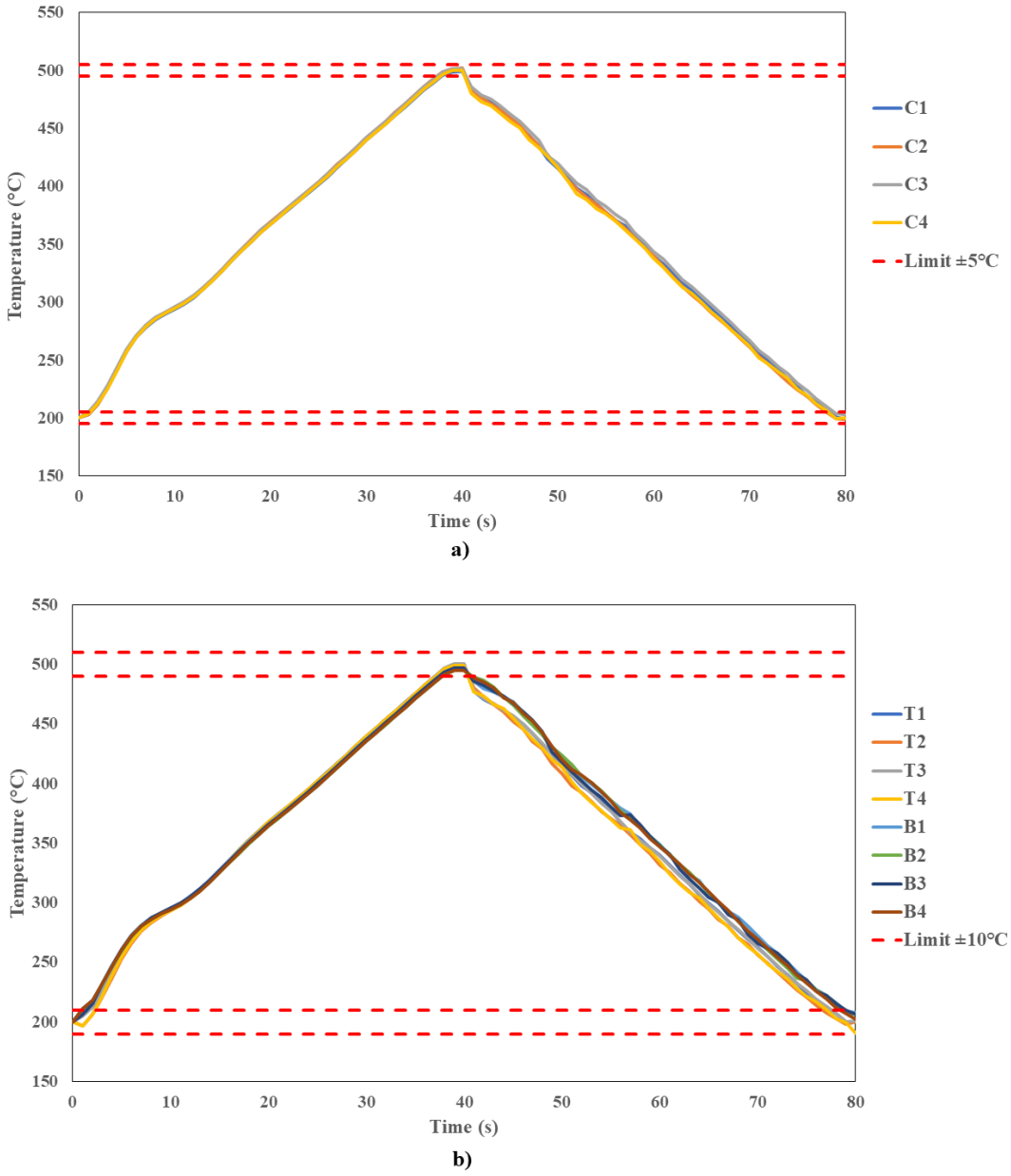

Figure 5.25 200-500°C thermal profile a) centre TCs b) top and bottom TCs

The minimum and maximum peaks are given in Figure 5.26. As shown, the achieved thermal profile is very close to the desired triangular waveform and the temperature limits set by the existing code of practice were achieved across the specimen.

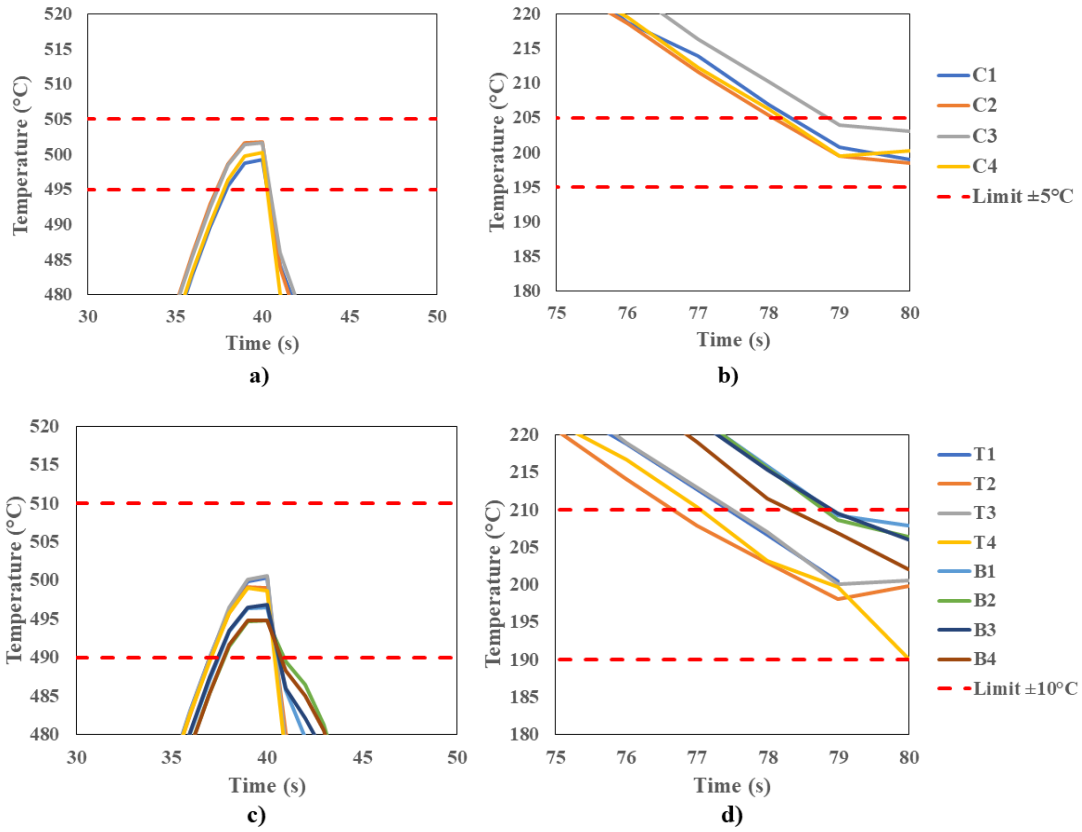

Figure 5.26 200-500°C centre thermal profile a) maximum peak b) minimum peak and axial profile c) maximum peak d) minimum peak

The final thermal profile for the 200-550°C cycle is shown in Figure 5.27 and Figure 5.28.

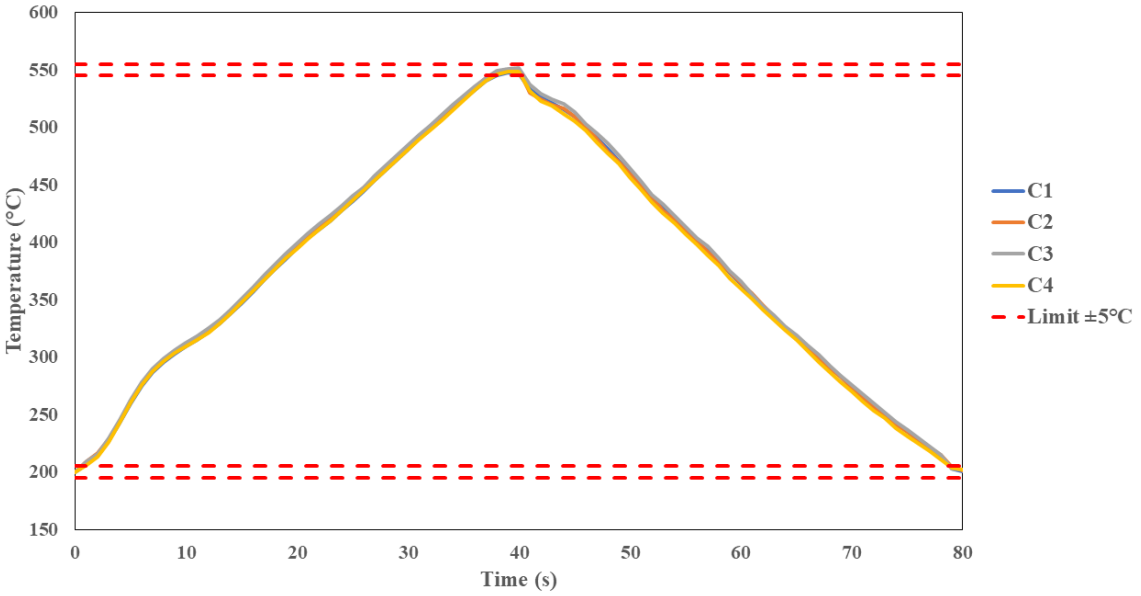

a)

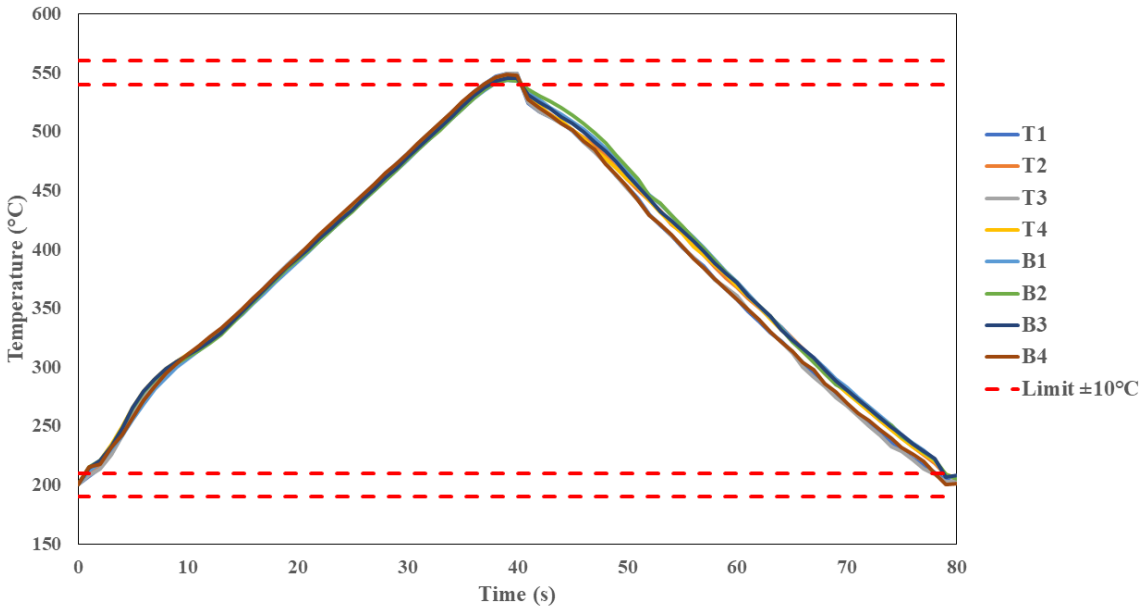

b)

Figure 5.27 200-550°C thermal profile a) centre TCs b) top and bottom TCs

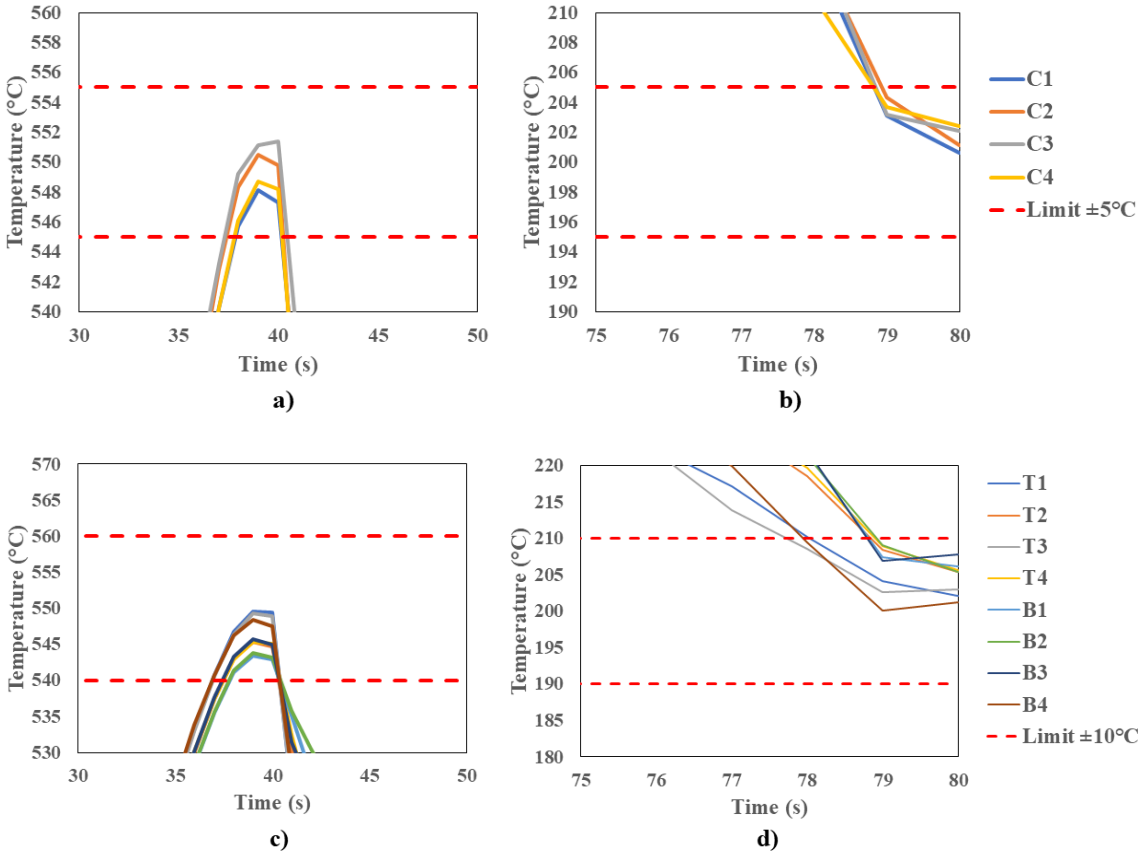

Figure 5.28 200-550°C centre thermal profile a) maximum peak b) minimum peak and axial profile c) maximum peak d) minimum peak

5.8 Test Matrices

5.8.1 Isothermal

A conventional radiant furnace is unable to produce the rapid thermal cycles required during TMF testing. It was therefore important to ensure a viable alternative was used. Induction heating has proven a popular choice for TMF testing, being employed in several institutes, as it is able to provide rapid thermal cycles and can be under both load and strain-controlled testing [95].

With access to existing facilities at Swansea University, the use of a novel quartz lamp furnace setup was also investigated as part of this research. The bespoke radiant lamp furnace (RLF) comprises of three independently controllable heating zones and benefits from built in internal compressed air specimen cooling. Adapted from its original application, this setup provided another possible method for TMFCG testing.

Isothermal fatigue crack growth (IFCG) tests were conducted at 500°C, R = 0 and were load-controlled with a maximum stress of 500MPa using a conventional radiant furnace, an induction coil system (ICS) and a bespoke RLF for the source of heating. The waveform adopted for such tests was a standard trapezoidal 1-1-1-1 waveform. These preliminary tests were conducted to provide a comparison between the heating methods and to aid the validation of the ICS and/or the RLF as viable methods of heating during TMF testing. IFCG tests were also conducted at 200°C, 350°C and 550°C to allow for direct isothermal comparison to TMFCG tests conducted. All tests are outlined in the test matrix presented in Table 5.3.

Table 5.3 IFCG test matrix for tests conducted throughout this investigation

IFCG	**Heating Method**		
Temperature (°C)	Conventional	ICS	RLF
200	1		
350	1		
500	2	1	1
550	1		

5.8.2 TMF

In order to compare heating methods used for TMFCG testing, tests were conducted using both the ICS and the RLF at the two extreme phase angles, IP and OP. Two triangular thermal cycles were employed; 200-500°C and 200-550°C over an 80 second cycle. Such thermal cycles were thought to be most representative of in-service TMF conditions seen by the IP compressor discs, as well as representing extreme temperature eventualities. All TMFCG tests were conducted at a maximum stress of 500MPa and a stress ratio of R = 0. The waveform adopted for the TMFCG testing in this programme was a triangular waveform with a frequency of 0.0125Hz.

The effect of diverse phasing and direction between mechanical stress and temperature of the TMFCG behaviour or Ti-6246 was also investigated. Using the ICS, test conditions included phase angles under CW and ACW diamonds (±90°), -135°, -150° and -170° loading cycles. All phase angles employed throughout this investigation are depicted in Figure 5.29.

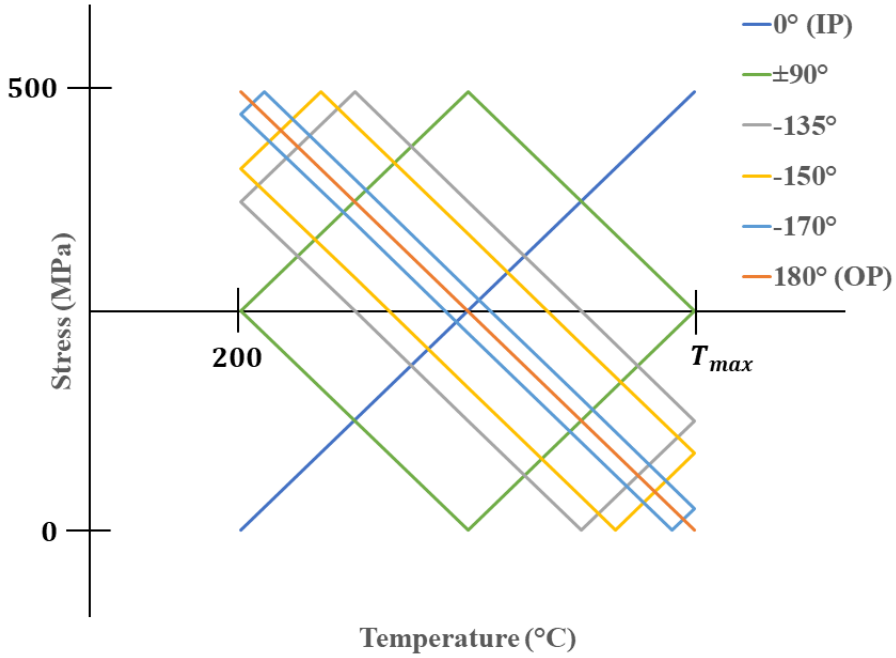

Figure 5.29 TMF phase angle loading conditions

All successful TMFCG tests undertaken are presented in the test matrix, Table 5.4.

Table 5.4 TMFCG test matrix for tests conducted throughout this investigation

TMFCG 200-500°C	**Heating Method**	
Phase Angle (°)	ICS	RLF
0 (IP)	4	2
180 (OP)	3	1
90 (CW)	1	
-90 (ACW)	1	
-135	1	
-150	1	
-170	1	
TMFCG 200-550°C		
Phase Angle (°)		
0 (IP)	1	1
180 (OP)	1	1

5.9 Post Test Metallographic Preparation

A number of specimens were sectioned for post-test analyses. Sectioning was conducted using an ATM Brillant 220 cut-off machine and an abrasive cutting wheel, supplied by MetPrep. For fractography, specimens were sectioned perpendicular to the loading direction in the x-z plane, preserving the fracture surface, as shown in Figure 5.30 a). Specimens for microstructural analysis around the fatigue crack were not cycled to failure after test and were subject to a further section at a 45° angle in the x-y plane, as shown in Figure 5.30 b). This was to ensure the true nature of the crack was being analysed, with no possibility of surface effects. Specimens were cleaned in an ultrasonic bath, washed with water, and dried with acetone.

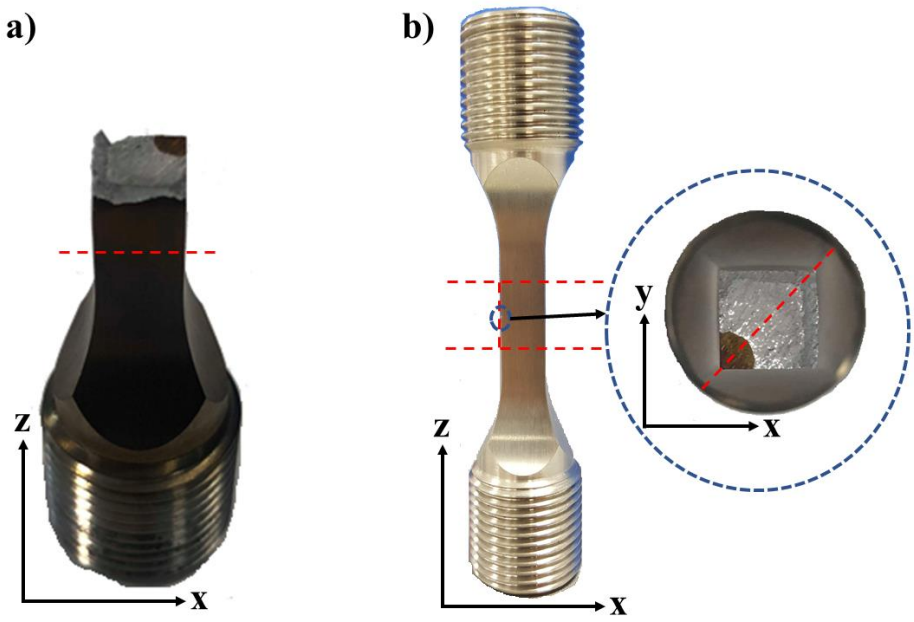

Figure 5.30 a) Image depicting how specimens were sectioned for fractography with the red line being the cut line b) image depicting how specimens were sectioned for microstructural analysis

Specimens that underwent microstructural analysis, electron backscatter diffraction (EBSD) and EDS were mounted in conductive bakelite using an ATM Opal 410 hot mounting press. Mounting was followed by a standard polishing procedure for titanium alloys, outlined in Table 5.5 using an ATM Saphir 550 before undergoing 4-6 hours polishing using a Buelher VibroMet 2 vibratory polisher.

Table 5.5 Polishing procedure used for titanium alloys

	Step 1	Step 2	Step 3	Step 4
Base Cloth	Piano-220	MD-Plan	MD-Chem	Alpha
Media	SiC with water	DiaPro Plan (9µm)	OP-S (0.04µm)	OP-S (0.04µm)
Force (N)	25	30	20	
Speed (rpm)	300	150	150	
Time (min)	1	5	10	4-6 hours

Etching of specimens was conducted to provide better exposure of certain microstructural features. Kroll's reagent (2ml HF, 10ml nitric acid, 88ml water), a useful etchant for most Ti-based materials, was swabbed onto a polished specimen for 20-30 seconds before being rinsed off with water and dried with acetone. This was used to better reveal the general microstructure of the Ti-6246 and allowed for better recognition of the large prior β grains on a macroscopic level. Some specimens underwent a colour tint etch with a modified Weck's reagent (100ml water, 5g ammonium bifluoride). By immersing the specimens for 30 seconds, the colours vary with grain orientation, colouring the α phase and thus allowed for optical analysis of texture within the material [135].

In order to analyse both the fracture surface and microstructure simultaneously, preservation of the fracture surface was required during the mounting and polishing stages of metallographic preparation. Applying 4-5 thin layers of Miccrostop; a liquid masking lacquer at 30-minute intervals, after the initial sectioning and cleaning stages, allowed for preservation of the fracture surface whilst undergoing mounting and polishing. Once standard preparation was complete, the specimen was removed from the bakelite and the Miccrostop layer was dissolved. The Miccrostop layer was dissolved and the specimen was cleaned via soaking in methyl-ethyl-ketone (MEK) and placing in the ultrasonic bath for a total of 30 minutes, changing the MEK at 10-minute intervals.

5.10 Post Test Analysis

5.10.1 FCG Analysis

During testing, the Dirlik DCPD-TMF software measures and records the crack growth in μV and the number of cycles. Having calibrated the FCG and input the initial crack length, the software outputs a crack length in mm, which can be displayed against the number of cycles, as shown in Figure 5.31.

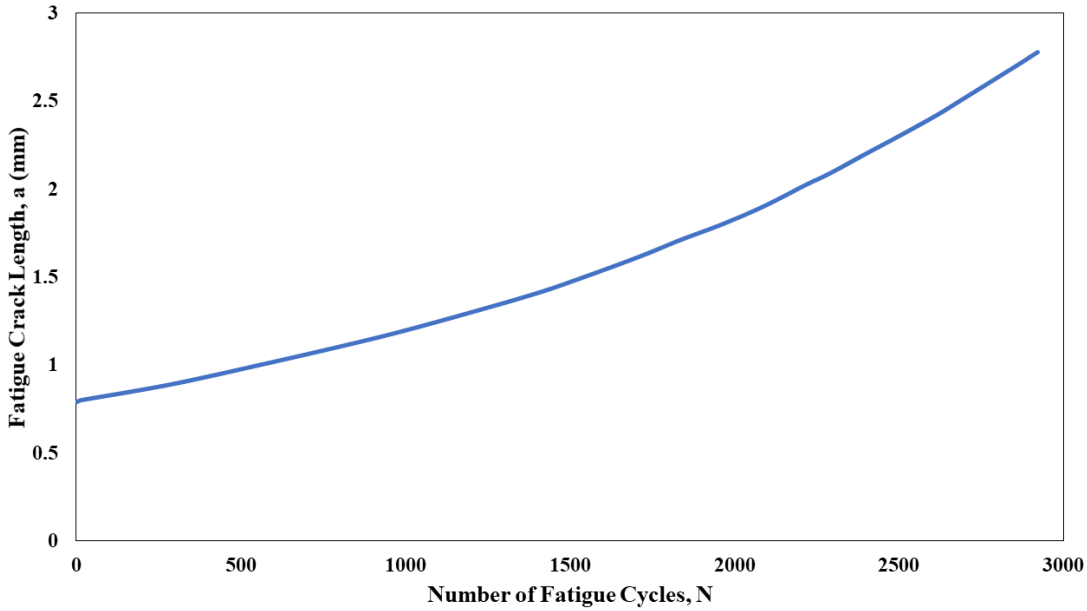

Figure 5.31 Crack length against number of fatigue cycles for a typical TMFCG test

With the data recorded by the Dirlik DCPD-TMF software and the post-test measurements of final crack length, it is possible to compute the FCG rate, da/dN and the stress intensity range, ΔK using Paris' Law in Equation 1, where ΔK is defined in Equation 2.

$$\Delta K = Y\Delta\sigma\sqrt{\pi a}$$

Equation 2

Where Y is a geometrical factor. The computation of da/dN and ΔK was possible through the Dirlik DCPD-TMF software, which is programmed to adhere to ASTM E647-13 [122]. From this, it was possible to present da/dN against ΔK on a log-log plot for the tests conducted.

5.10.2 Fracture Characteriation

A fractographic analysis was conducted on each of the specimens to assess the damage mechanisms occurring under diverse TMFCG loading conditions. Both optical microscopy (Keyence) and scanning electron microscopy were used for the purpose of fractography.

Once a test had reached its target crack growth it was cycled to failure and a high resolution, low magnification image was taken of the specimen's fracture surface using the Keyence microscope. The Keyence operates by taking multiple images of the fracture surface, focusing on different heights. The images are then stitched together, producing a completely in-focus image of the fracture surface, despite topographical differences. This image would be used to conduct 11-point measurement analysis to confirm the desired crack length had been achieved and it would also be used to document any crack initiation sites, other than that from the starter notch.

For the purpose of this investigation, a JEOL 7800F field emission gun scanning electron microscope (FEGSEM) was used to obtain higher magnification images of the specimen's fracture features. Differing from a tungsten source SEM, FEG sources have an electron beam that is smaller in diameter, more coherent and are capable of up to three orders of magnitude greater current density or brightness [136]. Ideal for high resolution and low voltage imaging, both macro and higher magnification images have been taken throughout this investigation.

5.10.3 Profilometry

Profilometry is a technique used to extract topographical data from the surface of a material. Used to obtain the surface morphology, step heights and surface roughness, profilometry can be done using a physical probe or by using light. Stylus profilometry requires force feedback and physical contact with the surface, so while it is extremely sensitive and provides a high resolution, this technique can also be destructive to some surfaces and therefore, optical profilometry was performed for this investigation.

Optical profilometry uses light instead of a physical probe. The light is directed in a way that can detect the surface in 3D. The wave properties of the light are used to compare the optical path difference between a test surface and a reference surface of known flatness [135].

Profilometry was performed on the fracture surfaces of various test specimens, using a Bruker Alicona InfiniteFocus optical microscope; an optical 3D surface measurement system that combines dimensional metrology and surface roughness measurement in one system. The optical microscope is capable of a maximum lateral measurement range of 31.7mm^2 and a vertical resolution of 10nm and relatively fast speeds, making it ideal for taking surface profile dimensional measurements [137].

The surface roughness, S_a measurements were calculated, via the built-in software, in accordance to ASME B46.1-2002, Assessment Surface Topography (Blunt/Jiang 2003), Characterisation of Roughness (Stout 2000) and ISO 25178 Areal – Part 2 [138]–[141].

A surface map was taken for each specimen, covering the fracture surface, as shown in Figure 5.32. The microscope parameters remained constant for each specimen to ensure comparable surface maps were computed. In saying that, all fracture surfaces were analysed using a 5x magnification lens, a lateral step-size of 7.83µm, vertical step-size of 0.13µm and an exposure time of 1.55ms.

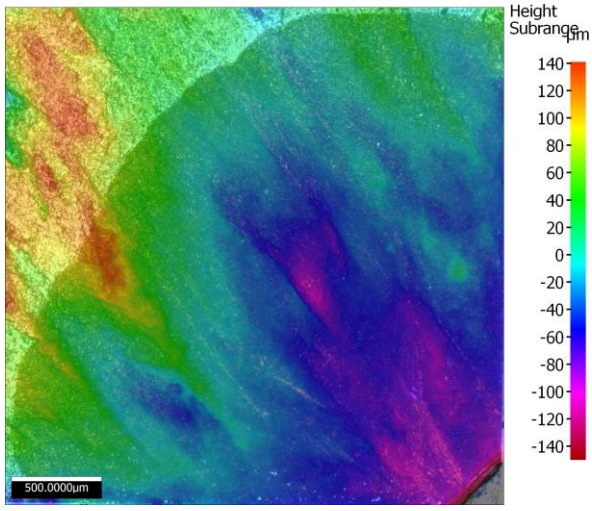

Figure 5.32 Surface map of a specimen fracture surface computed using the Alicona InfiniteFocus optical microscope

5.10.4 Microstructural Analysis

Various microscopy techniques were used to analyse the microstructure post-test. To understand the effects of different TMF test conditions on the microstructure around the crack plane, the test specimens were not cycled to failure and were sectioned as shown in Figure 5.30 b).

Using the Jeol 7800 FEGSEM, it was possible to analyse the general microstructure of the Ti-6246 test specimens used throughout this investigation. The fatigue crack and surrounding area were examined under secondary electron (SE) to aid the characterisation of fracture mechanism and determine if any creep or oxidation effects can be observed under different TMF conditions. Specimens tested under the extreme phase angles (IP and OP) at both temperature cycles (200-500°C and 200-550°C) were microstructurally analysed.

EDS is a chemical microanalysis technique used in conjunction with a SEM. It works through the detection of X-rays emitted from a sample during the bombardment by an electron beam. When the sample is hit by the SEM's electron beam, electrons are ejected from the atoms comprising the sample's surface. The arising electron openings are occupied by electrons from a higher state, and an X-ray is emitted to balance the energy difference between the two electrons' states. The X-ray is a characteristic of the element from which it was emitted and is compared to signals within a database to determine the elemental composition of the sampled volume [142]. EDS was performed on three specimens to determine the development and effects of oxidation under the different TMF conditions.

EBSD is a SEM based microstructural-crystallographic characterisation technique that is commonly used in the study of crystalline or polycrystalline materials. The technique can provide copious amounts of information about a material, including structure, crystal orientation, phase information and any strain within the material. EBSD maps have been produced and post-analysed using Oxford Instrument's EBSD post-processing software, HKL Channel 5. In particular, the phase distribution, crystallographic orientation and local misorientation/strain contouring of the specimens has been studied as part of this investigation. The EBSD maps were produced at the crack tip of the test specimens that had undergone IP and OP test conditions at 200-500°C and 200-550°C, to allow for direct comparison.

The Keyence optical microscope was used to analyse the general microstructure of the test specimens. Observing the specimens after etching with Kroll's reagent enabled general microstructural characterisation of the material and allowed approximations of the prior β grain sizes to be calculated, as shown in Figure 4.3.

Polarised light is a contrast-enhancing technique that improves the quality of an image obtained with birefringent materials, when compared to other techniques such as darkfield and brightfield illumination [143]. Although it is very difficult to quantify crystallography using polarised light microscopy, coupled with the colour tint given by etching with a modified Weck's reagent, it is possible to qualitatively analyse the grain orientation and texture within a material [135]. A Zeiss Primotech light microscope, equipped with a polariser, was used to analyse colour etched specimens to give an indication of effect of any texture on fatigue crack growth behaviour under varying TMF conditions. An example of an unpolarised and polarised image of the colour etched specimens can be seen in Figure 5.33.

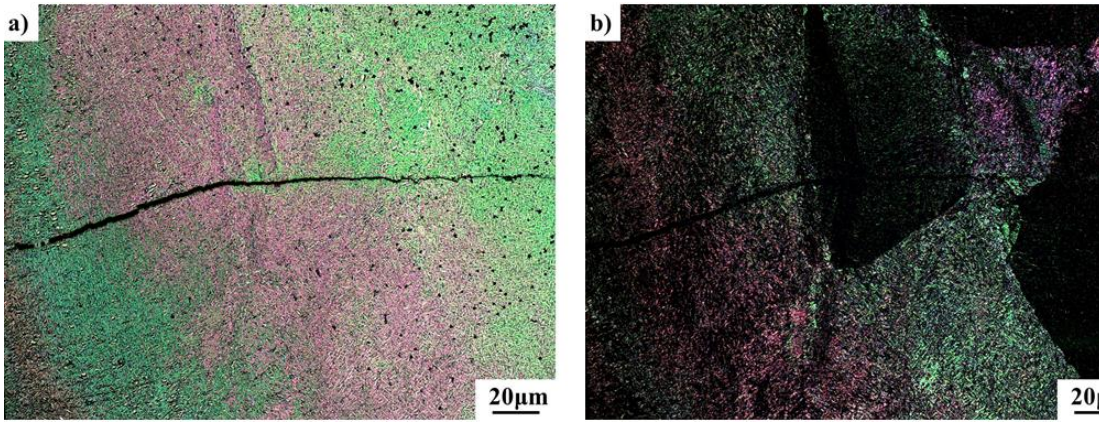

Figure 5.33 Image of specimen that has been colour tint etched with a modified Weck's reagent taken using the Zeiss Primotech, a) unpolarised, b) polarised

6 RESULTS & DISCUSSION

6.1 Testing

6.1.1 IFCG Heating Method Comparison

To compare and validate heating methods, IFCG tests were conducted, as displayed in Table 5.3. The heating methods utilised, as discussed previously, included a conventional radiant furnace, an ICS and a bespoke RLF. The tests conducted for this comparison were load controlled at a maximum stress of 500MPa, a stress ratio R = 0 and were tested using a 1-1-1-1 trapezoidal waveform with a frequency of 0.25Hz. The temperature at which these tests were performed was 500°C, in line with one of the maximum cycle temperatures used during TMFCG testing within this investigation. The Paris curves for the IFCG tests carried out are displayed in Figure 6.1.

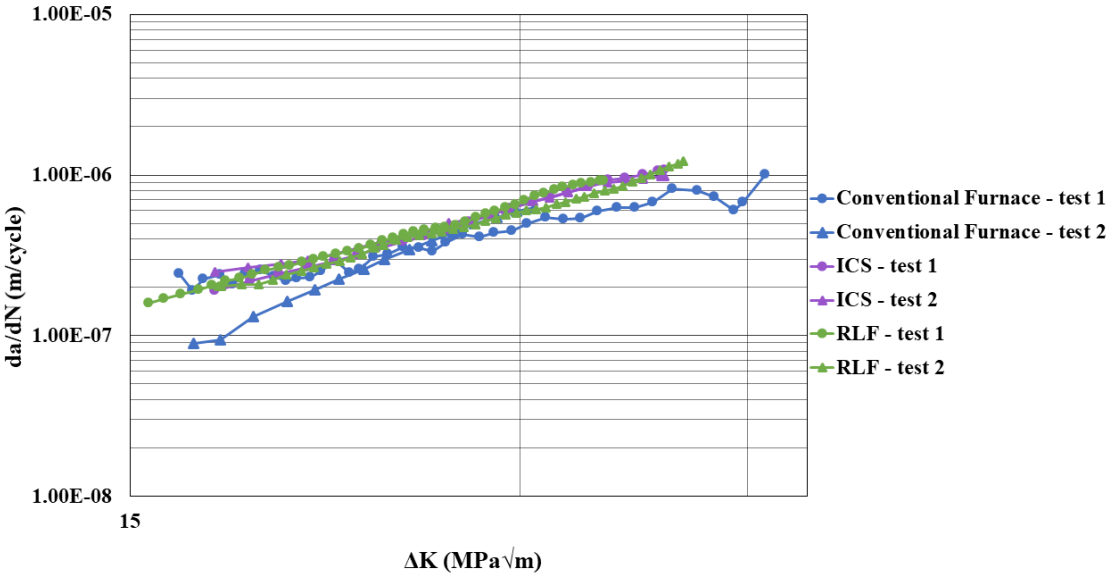

Figure 6.1 IFCG comparison of Ti-6246 at 500°C, 500MPa, R = 0 and f = 0.25Hz. Tests conducted using a conventional furnace, ICS and RLF

As shown in Figure 6.1, the tests conducted using the ICS and RLF provide very similar results, evidencing the repeatability of such tests. When compared to the tests conducted in the conventional furnace, it is evident that all tests follow a similar trend and are within a reasonable degree of scatter from each other.

Unlike the conventional furnace, an ICS and the bespoke RLF can provide the rapid heating rates required during TMF testing. However, the use of the DCPD method for crack monitoring, alongside an ICS has raised concern to some researchers and it is therefore important to ensure such a system is shown to provide comparable results [101][108]. The issue of current interference when coupling an ICS with the DCPD method was also addressed by Pretty (2014), who reported successfully combining the two for the use of TMFCG testing of RR1000. In undertaking this comparison, it is evident that the ICS and RLF do in fact provide comparable, repeatable, and reliable results and when coupled with the DCPD method, it has been possible to eradicate any current interference, through careful ICS selection.

6.1.2 TMFCG Heating Method Comparison

Following the IFCG comparison tests conducted, initial TMFCG tests were carried out using the ICS and the RLF to compare the two systems under TMF conditions. Both IP and OP tests were conducted using an ICS and RLF, with thermal cycles of 200-500°C and 200-550°C, maximum stress of 500MPa and a frequency of 0.0125Hz. The results are displayed in Figure 6.2.

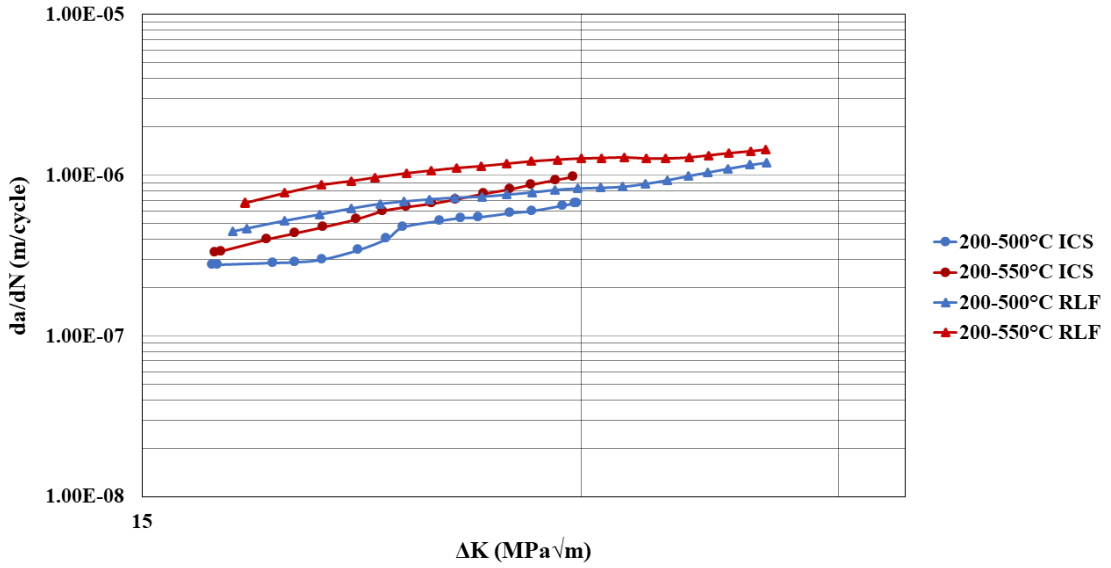

a)

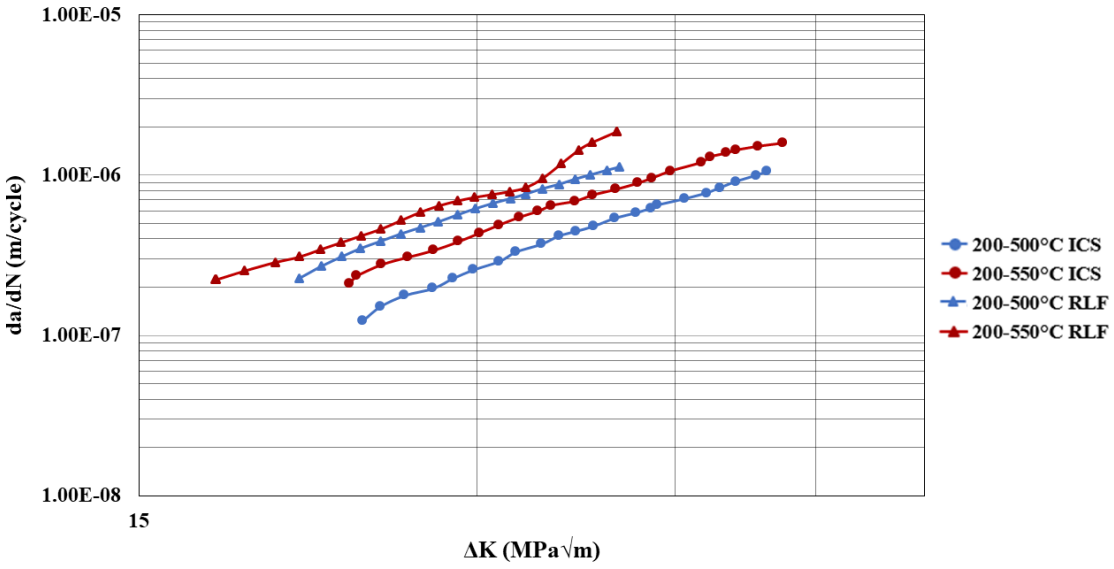

b)

Figure 6.2 TMFCG comparison of Ti-6246 using an ICS and a RLF. The thermal cycles used throughout the test were 200-500°C and 200-550°C. In all tests the maximum stress was 500MPa, R = 0 and f = 0.0125Hz. a) IP b) OP

Comparing the results displayed in Figure 6.2, it is seen that under both IP and OP conditions, the RLF has displayed marginally faster FCG rates. Although this difference is relatively small, it is possible the temperature lag displayed in Figure 5.14 may be inducing thermal stresses which are accelerating the FCG rate in the RLF tests. This difference in FCG rate, therefore, may need to be considered when TMFCG testing and suggests that the two methods may not be used interchangeably. It is also important to analyse the fracture mechanisms to determine the comparability of the two methods.

Figure 6.2 a) and b) both show that for IP and OP conditions in the ICS and RLF, the higher T_{MAX} cycle (200-550°C) displays faster FCG rates than those subjected to the thermal cycle 200-500°C. This increase could be explained as general scatter within the data, however, research by Evans et al. suggests this increase in FCG rate could be explained by the influence of increasing temperature due to creep and the environment [76]. The effect of increasing T_{MAX} from 500°C to 550°C in Ti-6246 is further supported by Jones et al. and Whittaker et al. who have also reported a marked difference in FCG rate at 550°C [144][12].

Comparing the OP results displayed in Figure 6.2 b) to the results of repeated tests using the ICS, under the same test conditions with a thermal cycle of 200-500°C, it does further open the question of temperature effects or general scatter. The additional results, displayed in Figure 6.3 b), would suggest that, within general scatter, the increase in T_{MAX} from 500°C to 550°C may not have a detrimental effect of the FCG rate of Ti-6246 under OP TMFCG conditions. However, with evidence presented in previous research suggesting T_{MAX} does in fact affect the FCG rate of Ti-6246, this has been further investigated through post-test analysis techniques, such as fractography and microstructural analysis.

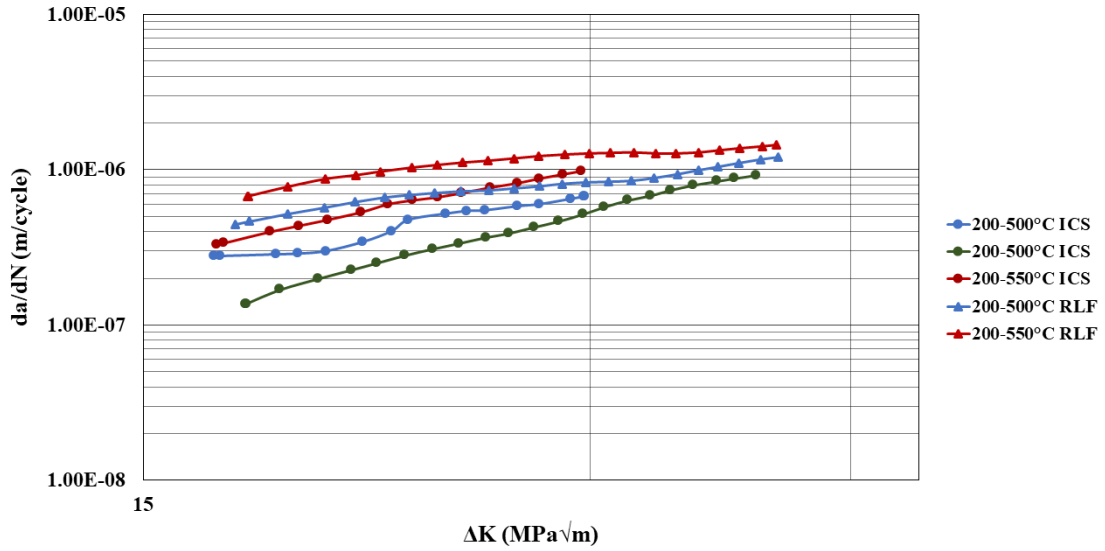

a)

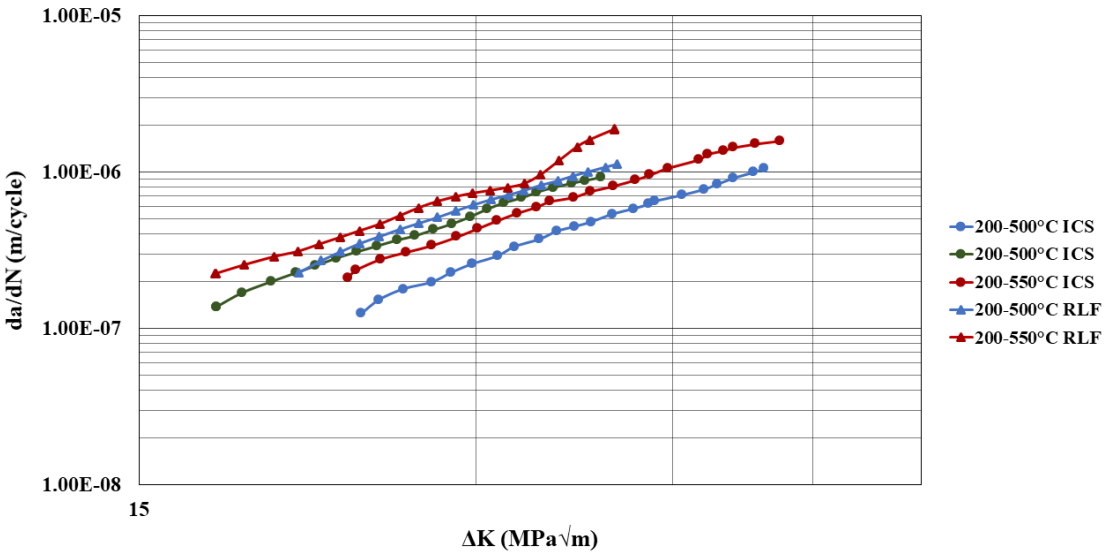

b)

Figure 6.3 TMFCG comparison of Ti-6246 using an ICS and a RLF, including a repeated test. The thermal cycles used throughout the test were 200-500°C and 200-550°C. In all tests the maximum stress was 500MPa, R = 0 and f = 0.0125Hz. a) IP b) OP

6.1.3 TMFCG IP vs OP

TMF is the combined effect of cyclic mechanical loading and cyclic temperature and when testing the TMF behaviour of materials, it is common to test under the two extreme phase angles: IP and OP. Using the ICS, both IP and OP tests at 200-500°C and 200-550°C have been conducted and the results have been compared. The Paris curves are displayed in Figure 6.4.

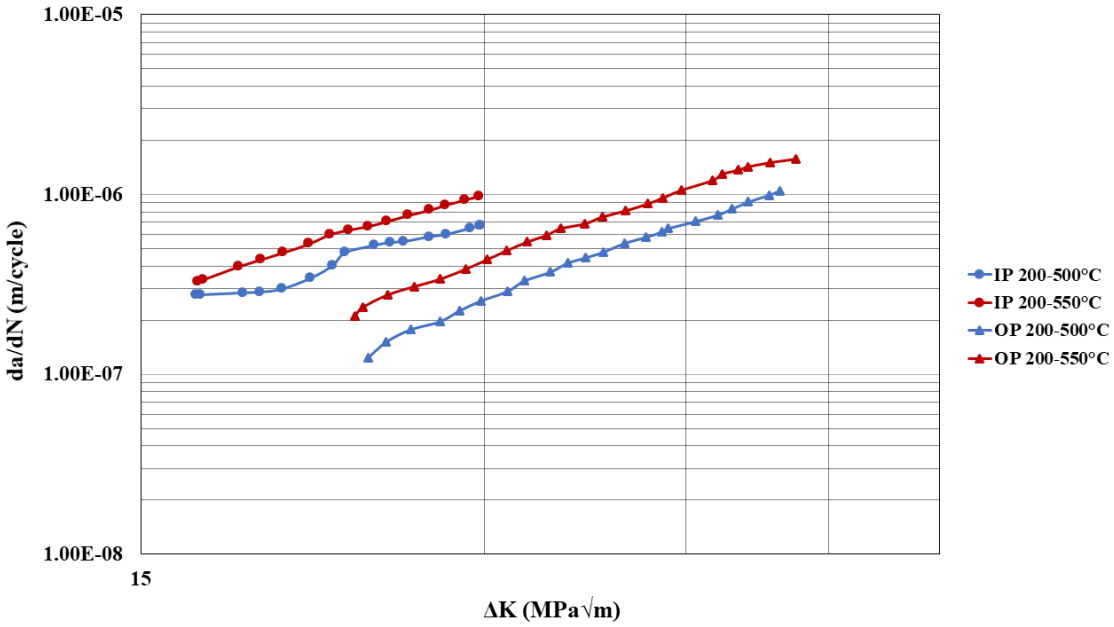

Figure 6.4 IP and OP TMFCG comparison of Ti-6246 using an ICS. The thermal cycles used throughout the test were 200-500°C and 200-550°C. In all tests the maximum stress was 500MPa, R = 0 and f = 0.0125Hz

Figure 6.4 shows that for both temperature cycles, the IP conditions display a faster FCG rate than the OP conditions. This is expected since during IP testing, the specimen is exposed to maximum stress and temperature concurrently. Such conditions are likely to promote time-dependent damage mechanisms, such as creep and oxidation, and thus are likely to increase the FCG rates. This TMFCG trend has been reported by researchers such as Pretty et al. [91]. Pretty reported IP TMFCG rates to be faster than OP during the testing of nickel-based superalloy, RR1000. Pretty was able to conclude that the increase in FCG rates seen were time dependent in nature, further supporting the findings of this investigation [91].

These findings contradict those reported by Prasad et al. [92] who reported seeing, when studying the TMFCG behaviour in Ti-834, the highest FCG rates at 450-600°C under OP TMF loading [92]. The same authors have reported similar findings when investigating the TMF behaviour in Ti-64, concluding the effects of oxidation are more detrimental in OP TMF loading [93]. However, previous research agrees with the findings of this investigation, in that IP conditions seem to be more damaging than OP [81][91]. The damage mechanisms in Ti-6246 under IP and OP TMF loading have been analysed as a part of this investigation to aid the understanding of the TMFCG behaviour in the material.

The FCG rate is higher at T_{MAX} = 550°C under both IP and OP loading. Although this could be within general scatter of the data, based on previous research, it is more than likely this is evidence of increasing temperature influencing the FCG.

6.1.4 TMFCG vs IFCG

As TMF is a complex phenomenon, to gauge a better understanding of the TMFCG behaviour of Ti-6246, IP and OP test results have been compared to IFCG tests. The FCG rates for IP and OP tests at 200-500°C and 200-550°C have been compared to IFCG tests at 500°C and 550°C, respectively. The Paris curves are shown in Figure 6.5.

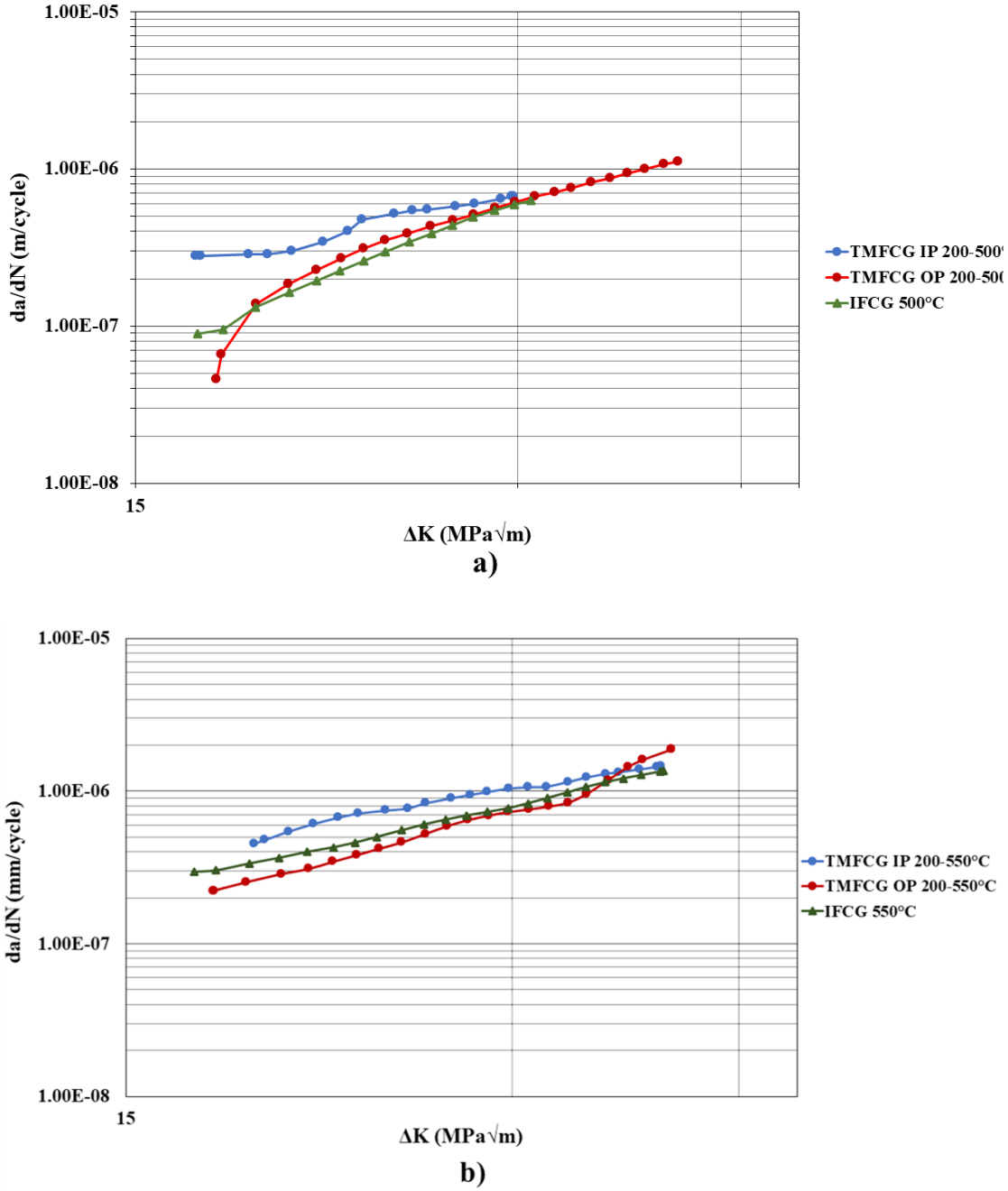

Figure 6.5 IFCG and TMFCG comparison of Ti-6246 using an ICS. In all tests the maximum stress was 500MPa and R = 0. The IFCG tests had a frequency of 0.25Hz and the TMFCG tests had a frequency of 0.0125Hz. a) T_{MAX} = 500°C and b) T_{MAX} = 550°C

In both Figure 6.5 a) and b), it is evident that the FCG rate is higher under IP TMF loading than OP or isothermal loading, albeit more prominent at the lower T_{MAX} of 500°C. It is important to note that the IFCG tests are conducted at a frequency of 0.25Hz, whereas the TMFCG tests are conducted at a frequency of 0.0125Hz and thus a much slower cycle. Pretty et al. [91] investigated the effects of cycle time and concluded that although the temperature varies in the TMF test, the slow cycle results in the material being exposed to higher temperatures for a longer period than that during the IF test. This therefore allows time dependent damage mechanisms, such as oxidation and creep, to take an effect and ultimately increase the FCG rate [91]. This theory of decreasing the frequency at high temperature increases the FCG rate is supported by Ghonem & Foerch [145] who investigated the frequency effects on FCG rates in Ti-1100. However, they believe the damaging effect of lower frequencies seems to depend less on the overall exposure time and more on the duration of the loading part of the cycle [145]. The FCG rates experienced under IP loading would support Ghonem & Foerch's [145] findings, as the increasing mechanical load at a lower frequency than that experienced under IFCG, combined with the increasing thermal loading, not seen concurrently under OP loading, would promote time-dependent damage mechanisms as suggested by Pretty [91].

Figure 6.5 b) shows the difference in FCG across IP, OP, and isothermal loading at T_{MAX} = 550°C is much less than that at T_{MAX} = 500°C. Previous research carried out by Evans et al. concluded that, when exposed to temperatures over 500°C, oxidation becomes the dominating damage mechanism in Ti-6246 [76]. This, therefore, could explain the reason for the reduced effect of phasing at T_{MAX} = 550°C.

Observing the FCG rates in Figure 6.5 a) and b), the largest disparity between the loading conditions occurs at the lower ΔK values. As ΔK increases, the FCG rates under IP and OP loading become similar and phasing is no longer a dominating factor. This contrasts the behaviour of nickel-based superalloy, RR1000, as reported by Pretty [146], who saw a parallel shift in FCG rate with differing phase angles. This finding in the behaviour of RR1000 suggests the effects of environment and creep are constant [146]. However, this does not appear to be the case in Ti-6246 and at higher ΔK values, environment and creep seem to have a different impact on the FCG rate than at lower ΔK values. It is possible that oxidation results in a certain crack increment per cycle, irrespective of ΔK. At low ΔK values, such affect is noticeable, but at higher ΔK values, the affect is beset by the dynamic fatigue growth. Similar findings have since been reported in RR1000, by Jones et al. [147].

6.1.5 TMFCG CW & ACW

If deviating from the phase angles 0° (IP) and 180° (OP), the additional factor of loading direction needs to be considered. Typical alternative phase angles investigated are the CW (+90°) and ACW (-90°), as shown in Figure 3.8. For both +90° and -90°, the highest stress appears at the mean temperature, whereas at the highest and lowest temperatures the stress magnitude is low. In CW tests, tensile loading takes place in the low temperature regime while compressive loading occurs in the high temperature regime, as shown in Figure 3.8. In ACW tests, it is the opposite situation.

To determine the effects of loading direction, CW and ACW TMFCG tests were conducted as part of this investigation. The thermal cycle used was 200-500°C. The maximum stress was 500MPa, R = 0 and f = 0.0125Hz, as with all TMFCG tests carried out as part of the investigation. The Paris curves are shown in Figure 6.6.

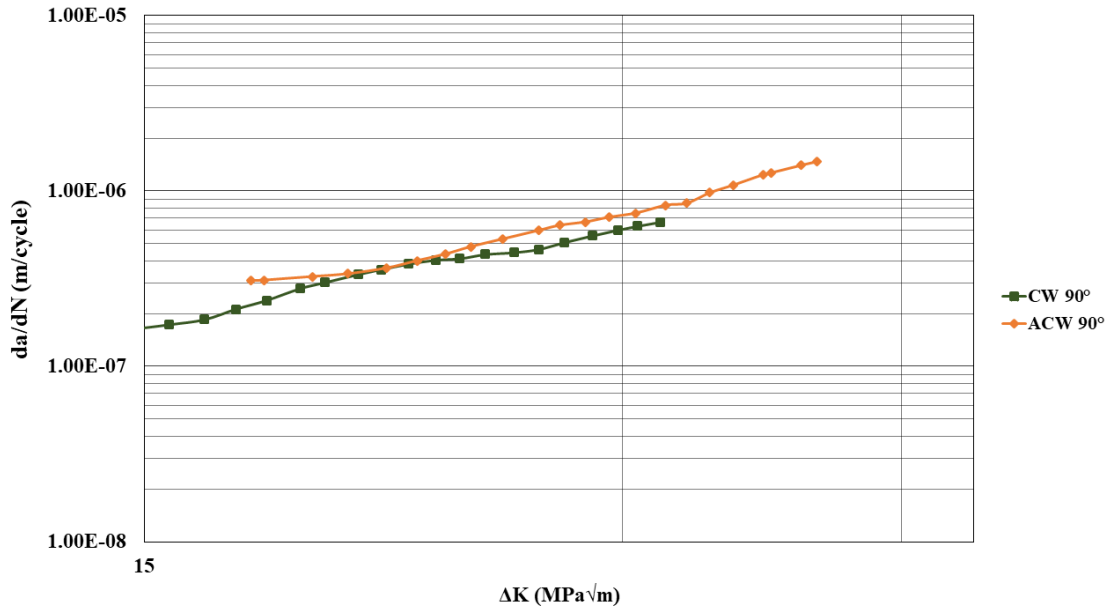

Figure 6.6 CW and ACW TMFCG comparison of Ti-6246 using an ICS. The thermal cycles used throughout the tests was 200-500°C. In all tests the maximum stress was 500MPa, R = 0 and f = 0.0125Hz

Figure 6.6 shows the FCG rates for both the CW and ACW tests are very similar, suggesting the loading direction does not have an effect in Ti-6246. The lack of directional effects on fatigue life, during CW and ACW phasing has been reported previously by Jones et al. [81]. Investigating the effects of phase angle in RR1000, Jones et al. concluded that +90° and -90° tests resulted in very similar fatigue lives. It was reported that for +45° and -135° tests conducted as part of the same study, the fatigue lives were mirrored, with +45° phasing resulting in a fatigue life closer to that of resulting from IP testing and the fatigue life under -135° closer to OP [81]. These findings are also support by Guth et al. [83], whom investigated the impact of phase directionality on the nickel alloy Mar-M247 [83].

6.1.6 TMFCG CW & ACW vs IFCG

As shown in Figure 3.8, the 90° phase angle results in the maximum and minimum stress occurring at the mean temperature and the maximum and minimum temperature occurring with the mean stress in the cycle. Therefore, the CW and ACW TMFCG rates have been compared to IFCG tests conducted at 200°C, 350°C and 500°C, shown in Figure 6.7.

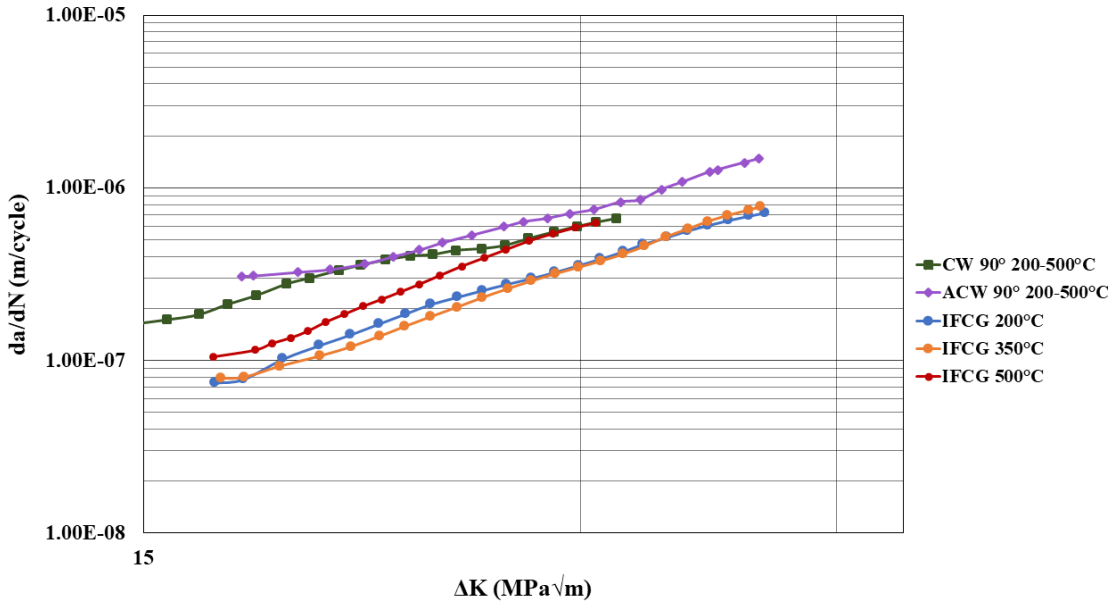

Figure 6.7 CW and ACW TMFCG and IFCG comparison of Ti-6246. In all tests the maximum stress was 500MPa and R = 0. The IFCG tests had a frequency of 0.25Hz and the TMFCG tests had a frequency of 0.0125Hz

Figure 6.7 shows the FCG rate is highest under the TMF test conditions and lowest under isothermal conditions at 200°C and 350°C. The resulting FCG rates at 200°C and 350°C are very similar, suggesting these temperatures are below that in which time dependent damage mechanisms, such as creep and oxidation, influence the crack growth in Ti-6246. Studying the IFCG behaviour of Ti-6246, Jones et al. noted creep and environmental effects begin to impact the FCG at temperatures of 400°C and above [144]. Therefore, explaining the increase in FCG rate at 500°C.

Again, the largest disparity in FCG is at the lower ΔK values. As ΔK increases, it is seen that the FCG rate under isothermal conditions at 500°C increases and becomes similar to the FCG rate experienced under the CW and ACW TMF conditions. Similar to the behaviour shown in Figure 6.5, this convergence in FCG could be that the effects of oxidation forming, resulting in an incremental crack growth each cycle, is beset by dynamic fatigue at higher ΔK values and thus is less marked than at lower ΔK values.

6.1.7 Phase Angle Comparison

As a part of this study, the effect of phase angle has been investigated. The motivation for this investigation is to better understand the TMFCG behaviour of Ti-6246 used for the intermediate-pressure compressor discs in the gas turbine. In particular, the area of interest is the circumferential loading slot, as shown in Figure 3.3. The closest representation of the stress condition seen by the circumferential loading slot of the disc is the phase angle -135° and thus it is important to determine the material's behaviour in relation to such phasing.

As part of this investigation the additional phase angles tested were in the ACW direction. Other than the four phase angles previously shown, TMFCG tests were conducted at -135°, -150° and -170°. The Paris curves comparing the different phase angles are displayed in Figure 6.8. The test conditions adopted include a thermal cycle of 200-500°C, maximum stress of 500MPa, R = 0 and f = 0.0125Hz.

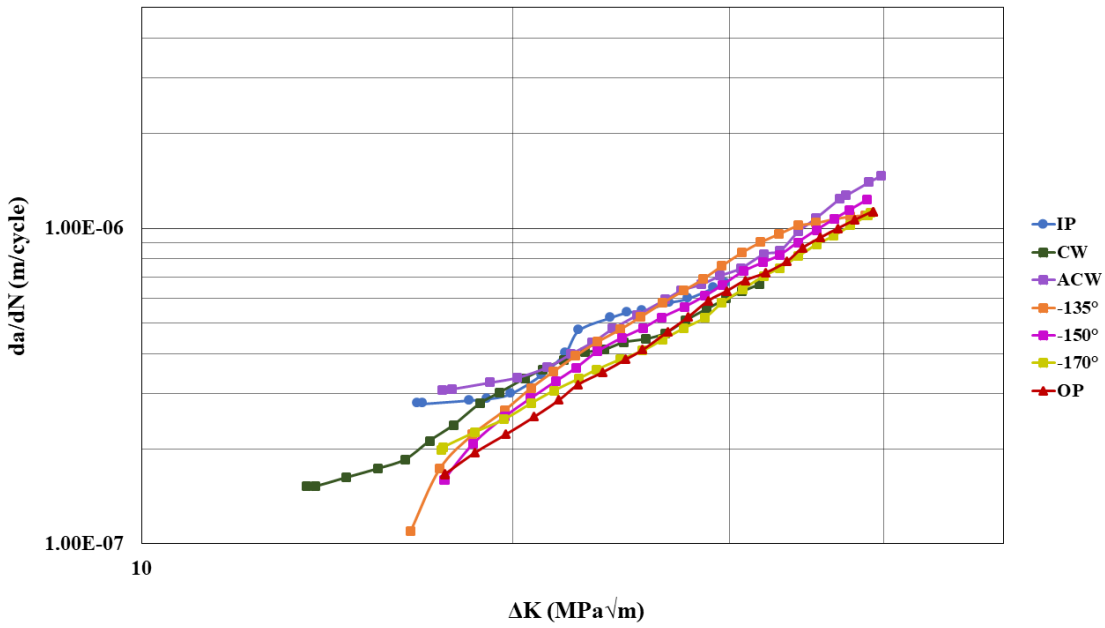

Figure 6.8 TMFCG comparison of tests conducted at different phase angles. The thermal cycle used for all tests was 200-500°C. In all tests the maximum stress was 500MPa, R = 0 and f = 0.0125Hz.

The FCG rate is fastest under IP conditions and slowest under OP conditions. Previous research agrees with this finding, with increasing stress and temperature concurrently under IP conditions proving more damaging than OP [81][91]. Figure 6.8 shows that although there is little disparity between the FCG rates at the varying phase angles, the FCG rate decreases as the phase angle increases towards OP (-180°). In studying the TMFCG behaviour of RR1000 at varying phase angles, Pretty found a similar trend, however, the disparity between FCG rates at varying phase angles was larger than those seen in this investigation of the TMFCG behaviour of Ti-6246 [146]. Jones et al.'s investigation into the influence of phase angle on the TMF crack initiation behaviour of RR1000 also saw that IP was more damaging than OP. They were able to report that when deviating from the two extremes, the fatigue lives are situated between IP and OP, with very similar fatigue lives in the CW (90°) and ACW (90°). The study also found that an almost symmetrical relationship, with the fatigue response in the CW (45°) being closer to the IP response and ACW (135°) being closer to the OP response [81].

Although the effects of phase angle on the TMFCG behaviour of Ti-6246 appear to be less than those reported in RR1000, the subtle differences suggest that phase angle is an important factor and that there must be a difference in damage mechanisms between IP and OP TMF conditions.

6.1.8 Testing Summary

IFCG tests conducted using a conventional furnace, ICS and RLF resulted in comparable FCG rates. However, TMFCG tests using the ICS and RLF resulted in slight variations, with the RLF resulting in consistently faster FCG rates. It is likely that this variation is caused by the temperature lag displayed in Figure 5.14 which may be inducing thermal stresses which are accelerating the FCG rate in the RLF tests.

In comparison to IFCG, TMFCG test conditions are shown to be more detrimental to a component's life. Investigating the effects of phase angle has shown that IP test conditions are more detrimental than OP, resulting in a faster FCG rate at both 200-500°C and 200-550°C. Phase angles between the two extremes resulted in subtle differences in FCG rates that were between IP and OP. This suggests that there must be a difference in damage mechanisms between IP and OP TMF conditions.

6.2 Fracture Characterisation

6.2.1 IFCG Heating Method Comparison

This study has compared heating methods under isothermal conditions. As well as analysing the IFCG rates when using the conventional furnace, ICS and RLF, the fracture surfaces have been studied to aid the characterisation of fracture mechanisms. Using an SEM, Figure 6.9 a)-c) shows that under isothermal conditions, all three heating methods have resulted in transgranular fracture.

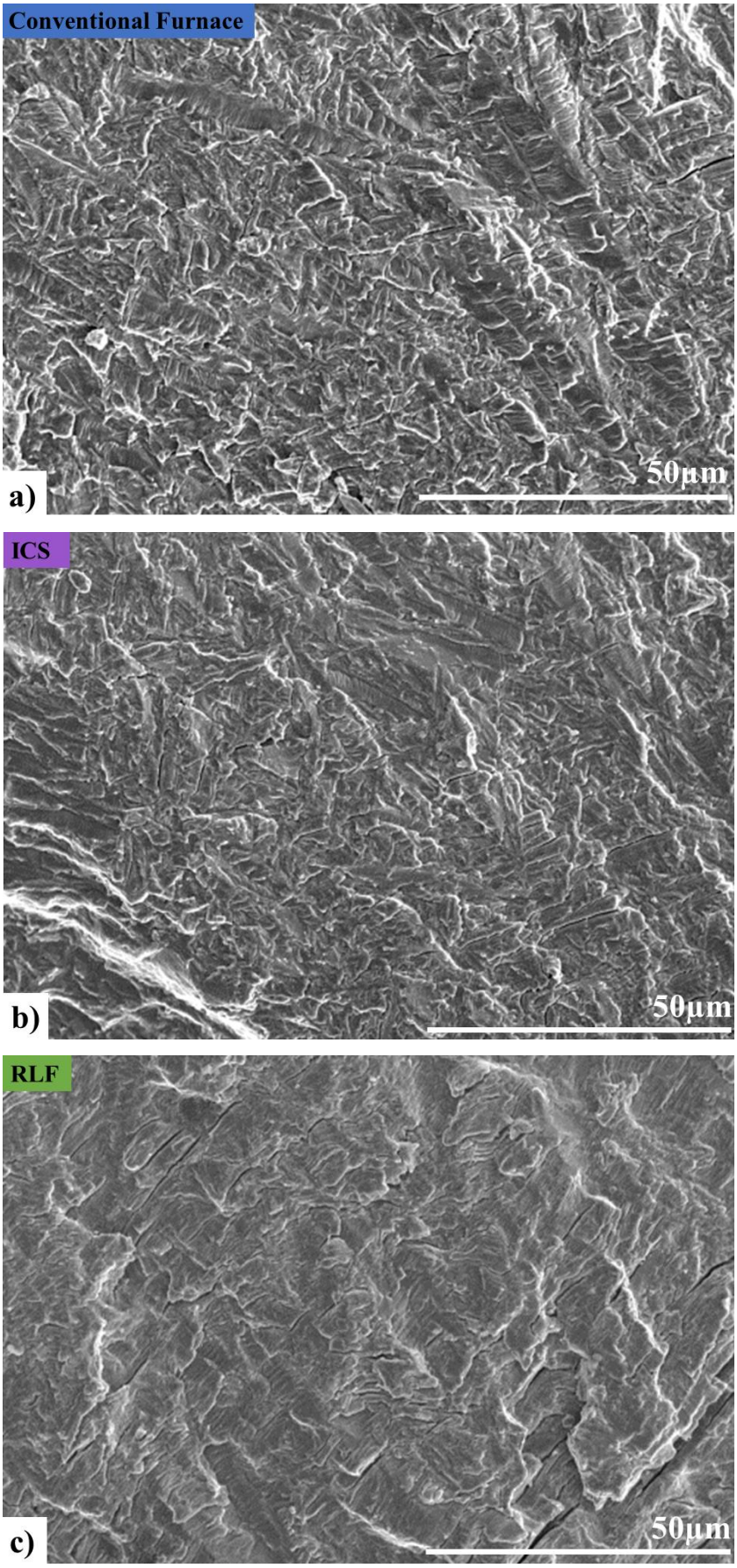

Figure 6.9 Fractography comparing a) conventional furnace, b) ICS and c) RLF fracture surfaces tested under IFCG conditions at 500°C

The evidence of all three heating methods resulting in transgranular fracture under the same test conditions supports the IFCG results presented in Figure 6.1. This finding also further confirms the comparability and repeatability of the results produced from the different heating methods.

6.2.2 TMFCG Heating Method Comparison

The fracture surfaces of test specimens that have been subject to IP TMFCG conditions at 200-500° in the ICS and RLF were analysed and are shown in Figure 6.10. Figure 6.10 shows that testing under IP TMFCG conditions using both the ICS and RLF results in very similar fracture surfaces with both fracture mechanisms appearing to be predominately transgranular. The very similar modes of fracture presented in the fractography would support the comparability in the two heating methods, suggesting that deviations in the results could be within general data scatter. However, the differences in FCG would still suggest that the ICS and the RLF may not be used interchangeably for TMFCG testing, and thus one of the two methods should be adopted for the entirety of an investigation.

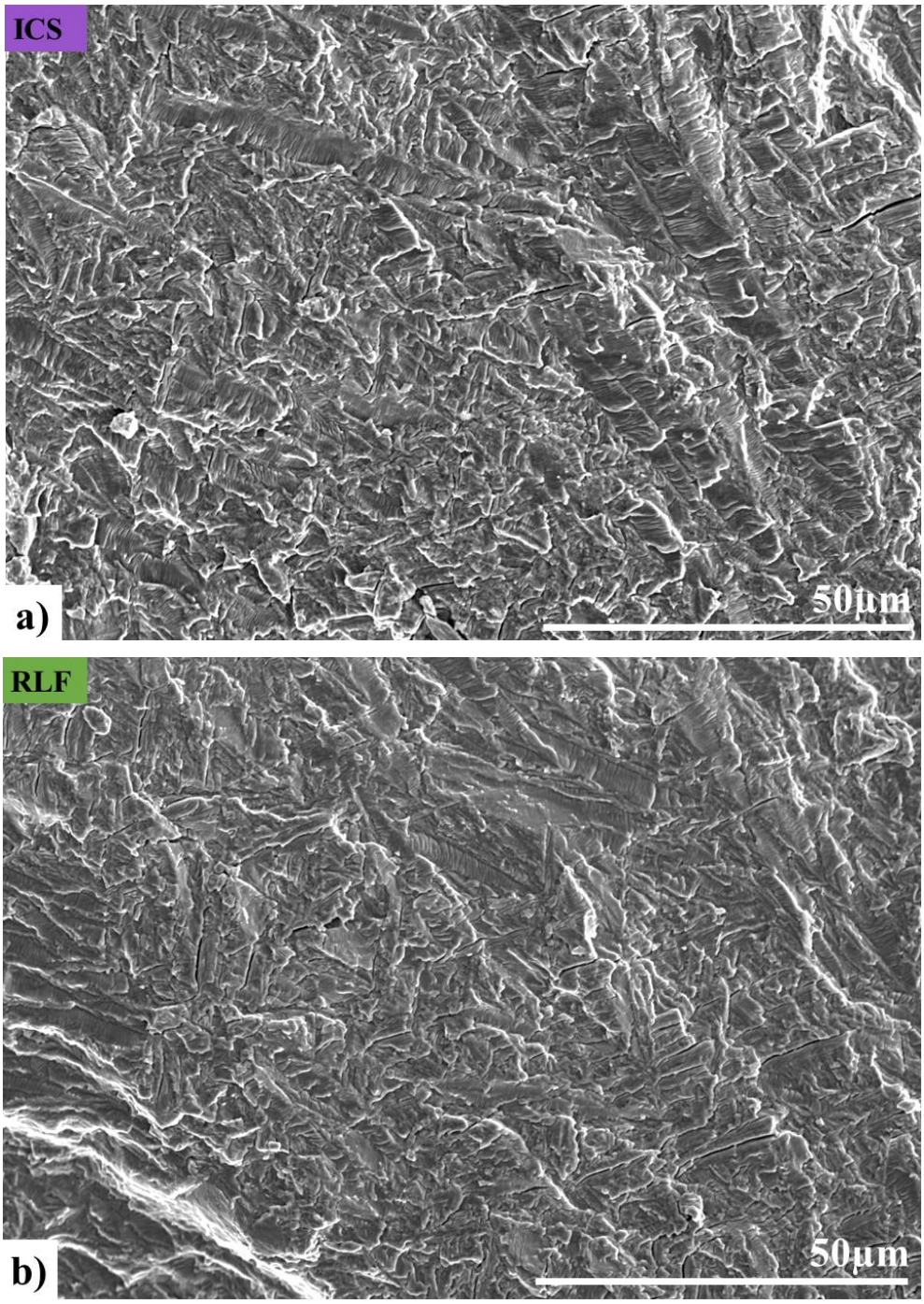

Figure 6.10 Fractography comparing a) ICS and b) RLF fracture surfaces tested under IP TMFCG conditions at 200-500°C

6.2.3 TMFCG IP vs OP

The fracture surfaces of test specimens subjected to IP and OP TMFCG conditions at 200-500°C and 200-550°C were analysed and compared, in order to characterise the fracture mechanisms present under the different loading conditions. The fractographs displayed in Figure 6.11 and Figure 6.12 were taken at similar locations on the fracture surfaces, at approximately 1.4mm from the corner notch, allowing for fair comparison of the mechanisms present.

Figure 6.11 shows initial imaging of the fracture surfaces of test specimens subject to the thermal cycle of 200-500°C. As can be seen, both fracture surfaces, on initial inspection look very similar, with both the IP and OP TMFCG conditions displaying predominately transgranular fracture.

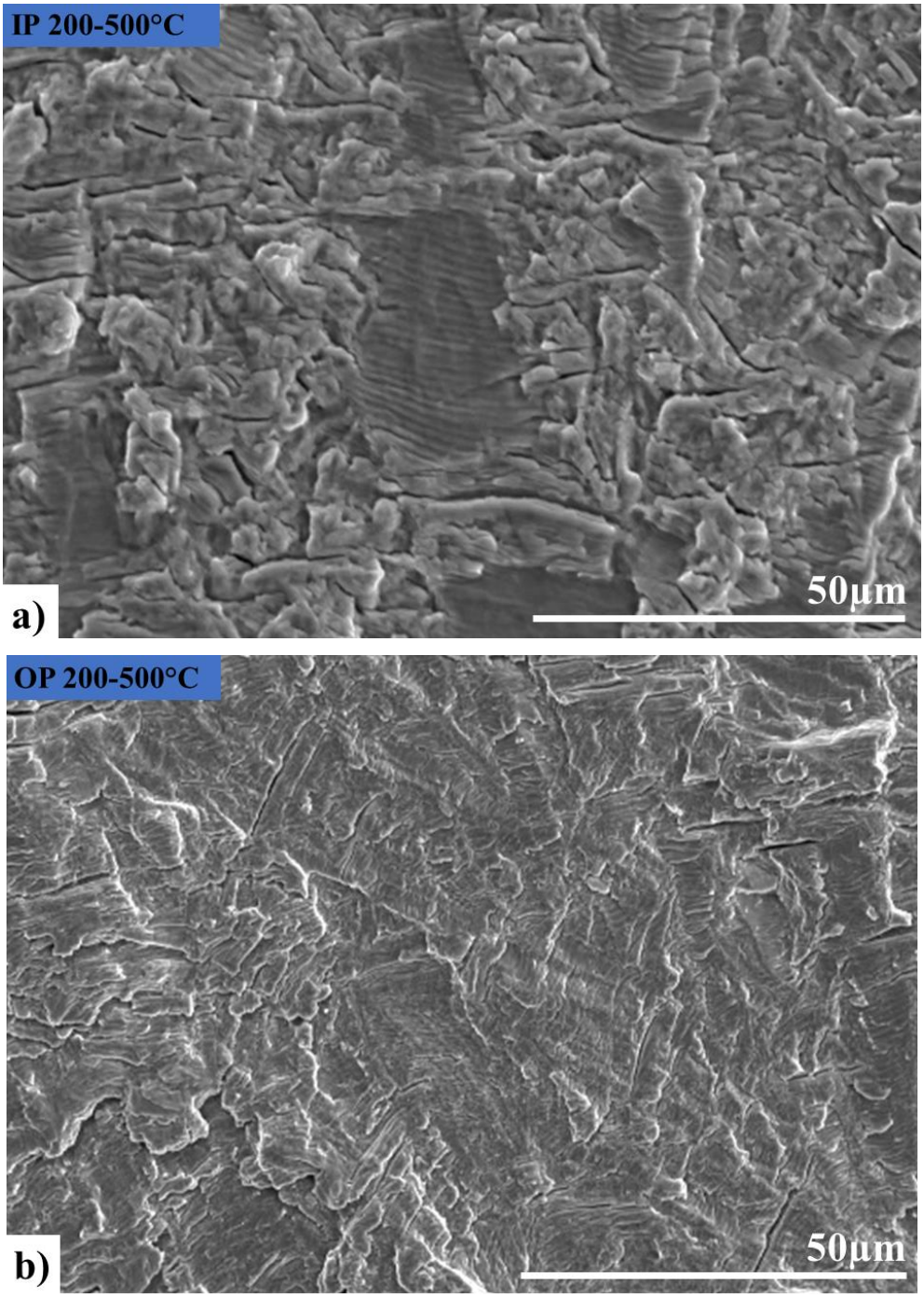

Figure 6.11 Initial fractography comparing a) IP and b) OP TMFCG conditions at 200-500°C

Previous research into the TMF behaviour of nickel-based superalloys reports a distinct change in damage mechanism, with IP resulting in a predominately intergranular fracture, and OP presenting as predominately transgranular [81][91][89]. Jones et al. attributes creep and oxidation damage on grain boundaries to accelerated intergranular crack propagation in IP testing of RR1000. The researchers believe the increased transgranular cracking under OP conditions in RR1000 is due to the high stress at low temperature [81]. However, Figure 6.11 does not show such transition in Ti-6246 and with limited research into the TMFCG behaviour of titanium alloys, it is difficult to determine if such a transition is expected.

Hyde et al. also observed a transgranular to intergranular transition in RR1000 with increasing temperature, further supporting the influence of creep and oxidation on the change in damage mechanism [89]. A similar transition with increasing temperature has been observed by Lerch et al., for another nickel-based superalloy, namely, Waspaloy. At temperatures up to and including 500°C, cracks were observed to initiate in a transgranular manner, whilst above 800°C the cracking mechanism was predominately intergranular [90].

Observing the initial fractography in Figure 6.12, it could be argued that the increased T_{MAX} has resulted in a rougher fracture surface under IP TMFCG conditions than OP. The rougher fracture surface shown in Figure 6.12 a) could evidence a more intergranular fracture than that shown in Figure 6.12 b), and would support the findings of temperature influence on FCG behaviour of nickel alloys. However, if this is the case, the mechanism change is far more subtle in the Ti-6246, with the IP test specimen shown in Figure 6.12 a), still presenting a predominately transgranular fracture.

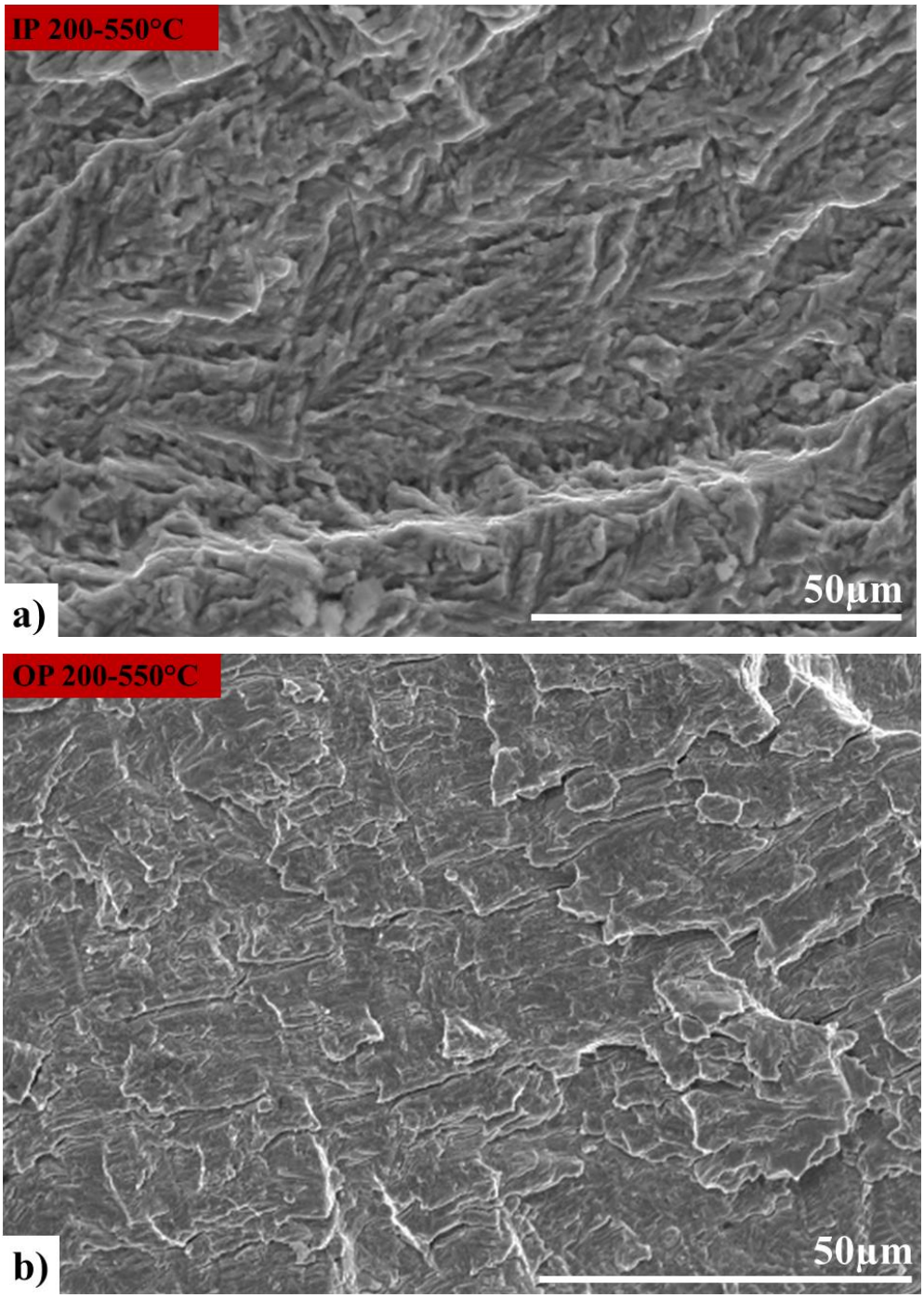

Figure 6.12 Initial fractography comparing a) IP and b) OP TMFCG conditions at 200-550°C

The reason for a transition in nickel alloys, from transgranular cracking in OP TMF testing, to intergranular crack in IP TMF testing is thought to be attributed by creep and oxidation under the high temperature, high stress condition experienced during IP TMF testing. Thus, if this is the case, it is thought that such transition should be present in Ti-6246 under similar loading conditions. However, the lack of such transition could be attributed to by several factors, such as the alloy composition and the microstructure. With the Ti-6246, used in this investigation, displaying a fine Widmanstatten microstructure, further fractographic analysis was conducted.

The initial fractography, displayed in Figure 6.11 and Figure 6.12 was conducted at a scale too large to achieve high definition of the finer microstructural features, such as the α-laths. Thus, to obtain a better understanding of the damage mechanisms present, finer scale fractography was conducted.

Still investigating the FCG behaviour of IP and OP conditions, fractographs were taken in three locations; near the pre-crack region (~0.8mm), towards the middle of the crack (~1.4mm) and near the crack tip (~2.8mm). The fracture surfaces of the IP and OP TMFCG test specimens at 200-500°C are compared in Figure 6.13.

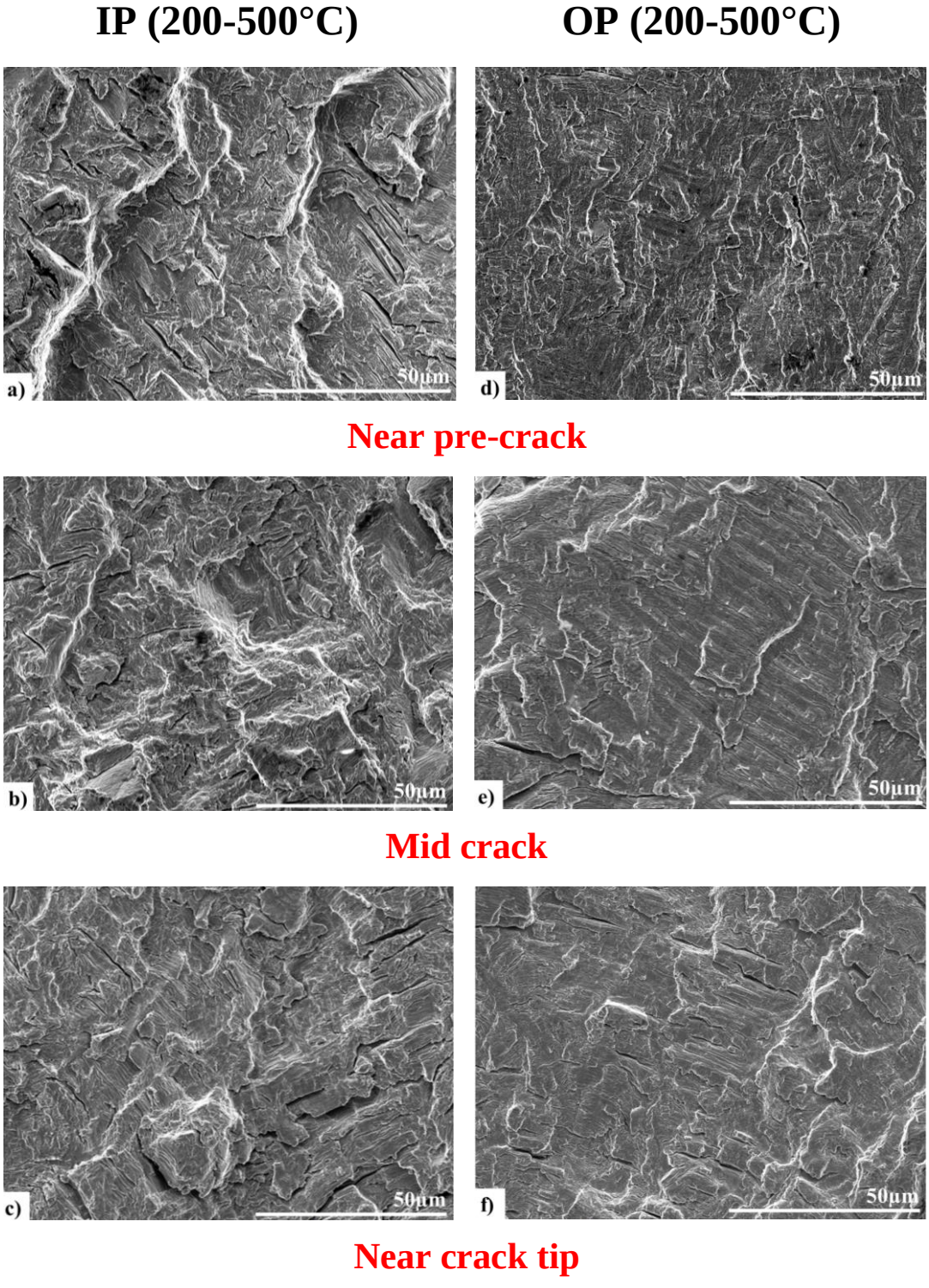

Figure 6.13 Fractography of TMFCG IP 200-500°C a) near pre-crack, b) mid crack, c) near crack tip and TMFCG OP 200-500°C d) near pre-crack, e) mid crack and f) near crack tip

Interestingly, on a finer scale, Figure 6.13 a) displays a rougher fracture surface, whereas, Figure 6.13 d) is very flat in nature. It is further evident that the IP TMFCG test specimen appears to result in a rougher, more jagged fracture surface throughout the fracture surface, from near the pre-crack to near the crack tip. Such findings, during IP TMFCG conditions at 200-500°C, may in fact present evidence of interlamellar cracking as well as translamellar cracking which on a larger scale presents as predominately transgranular in nature.

This finer scale difference that shows IP TMFCG testing to result in possible mixed fracture mechanisms with evidence of rougher, interlamellar cracking, and OP TMFCG testing to show as predominately translamellar/transgranular would suggest that there is a difference between the two conditions. Although the differences are very subtle, these findings would further support the conclusions of increased influence of creep and oxidation during IP loading, made by researchers previously mentioned [81][91][89].

Figure 6.13 d) and e) shows the OP TMFCG test specimen at 200-500°C displays a very flat, translamellar fracture near the pre-crack and toward the middle of the crack region. However, nearing the crack tip, where the ΔK is higher, the fracture surface appears rougher, possibly displaying evidence of interlamellar cracking, as well as translamellar. As previous researchers have attributed the presence of intergranular/interlamellar to the increased effects of time-dependent damage mechanisms during high temperature and high stress loading conditions, this finding could support the results displayed in Figure 6.5 and Figure 6.7 [81][91]. As reported by Evans et al., creep has a high stress dependency so that a high peak tensile stress and high K_{MAX} creep damage will be promoted at the crack tip [76].

Further analysing the features present on the fracture surface of the IP TMFCG test specimen, it is evident that secondary cracking is seen from near the pre-crack through to near the crack tip. This secondary cracking is likely to be attributed by oxidation and is supported by findings of Whittaker et al. who reported cracking between α and β interfaces at 500°C in Ti-6246 [12]. As the fatigue crack is subject to tensile loading and is held open as the temperature increases to T_{MAX} during IP loading, oxygen can penetrate the surface, resulting in a brittle oxide layer, which when cycled, results in secondary cracking. Figure 6.13 f) shows that the secondary cracking is present near the crack tip during OP TMFCG testing. This further supports that time-dependent damage mechanisms become more dominant at higher ΔK values during OP TMFCG conditions.

To establish a reliable trend, the fracture surfaces of repeat test specimens, subjected to the same test conditions; IP and OP TMFCG at 200-500°C, were analysed. Figure 6.14 shows similar trends to those highlighted in Figure 6.13, with IP conditions resulting in a more mixed fracture mode, showing evidence of interlamellar and translamellar cracking, whereas OP conditions are predominately translamellar/transgranular throughout.

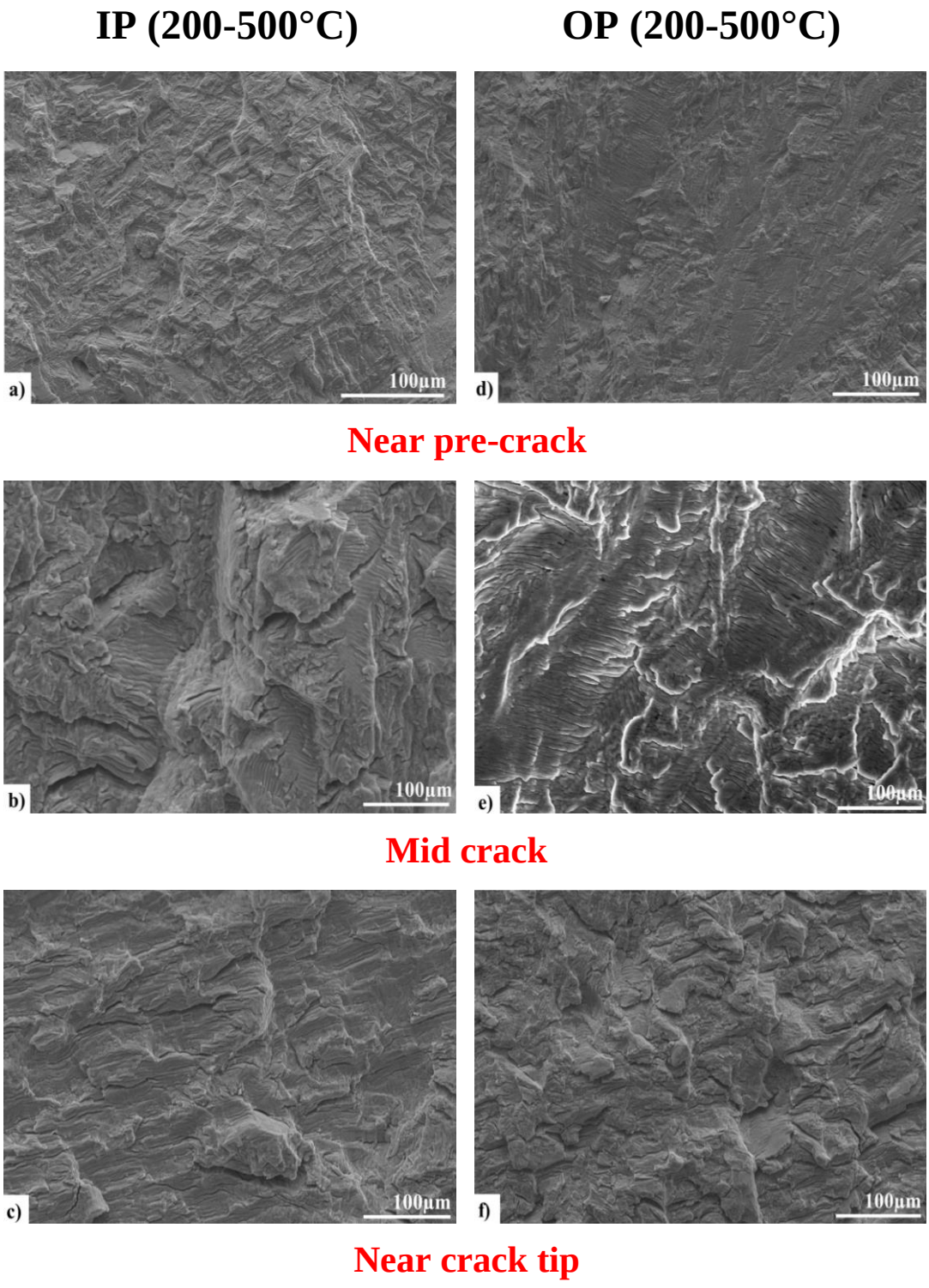

Figure 6.14 Fractography of repeated tests: TMFCG IP 200-500°C a) near pre-crack, b) mid crack, c) near crack tip and TMFCG OP 200-500°C d) near pre-crack, e) mid crack and f) near crack tip

Lerch et al. [90] reported a transition from transgranular cracking to intergranular cracking with increasing temperature in nickel alloys. The increasing influence of time-dependent damage mechanisms at higher temperatures in Ti-6246 has been reported by several researchers [76][144][12]. With both findings in mind, the fracture surfaces of Ti-6246 specimens tested under IP and OP TMF conditions at 200-550°C have also been investigated as part of this study. As with the tests conducted at 200-500°C, fractographs have been taken near the pre-crack, towards the centre of the fatigue region and near the crack tip and are displayed in Figure 6.15.

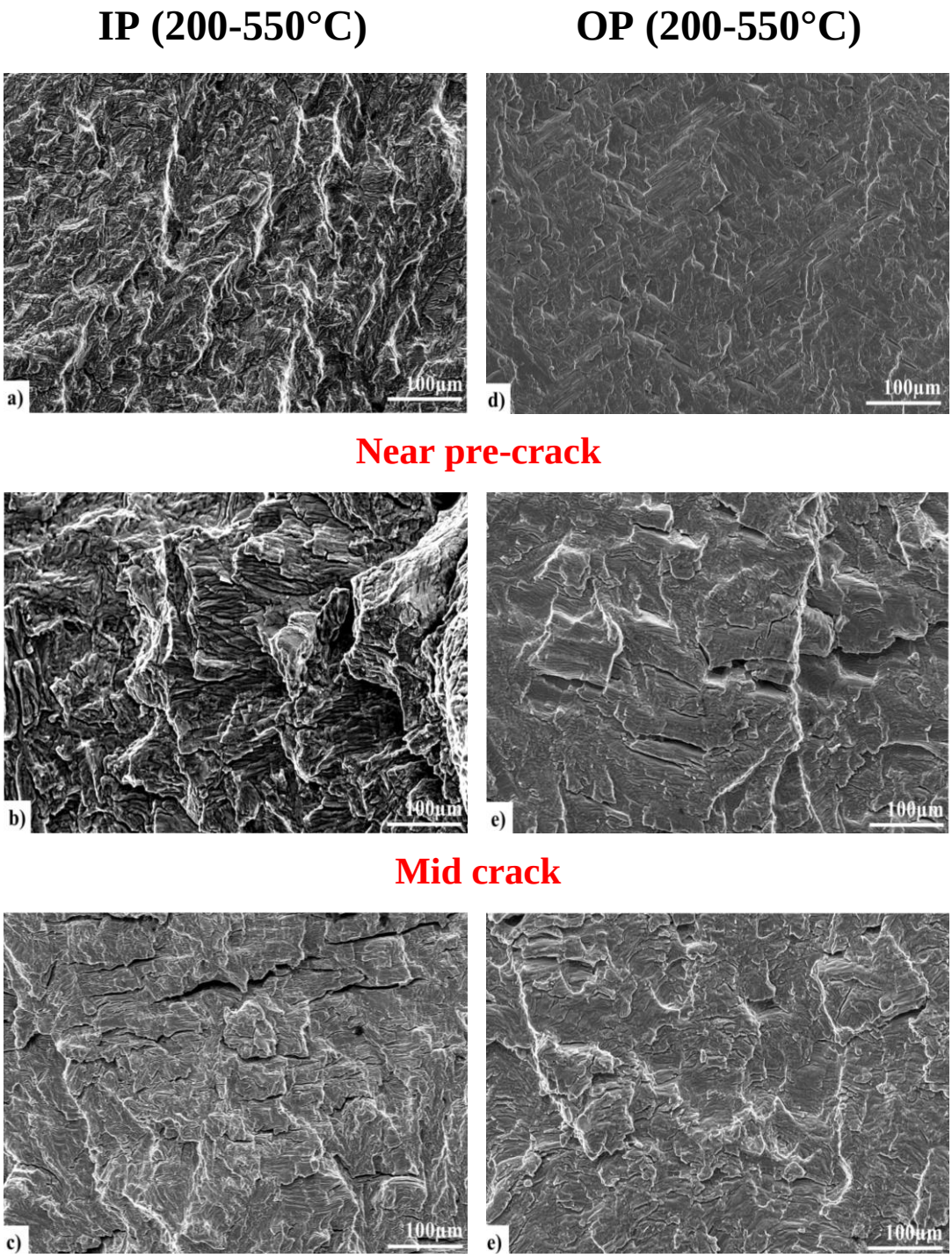

Figure 6.15 Fractography of TMFCG IP 200-550°C a) near pre-crack, b) mid crack, c) near crack tip and TMFCG OP 200-550°C d) near pre-crack, e) mid crack and f) near crack tip

Figure 6.15 a) – c) shows that during IP TMF conditions at 200-550°C, the fracture surface is again mixed with interlamellar and translamellar cracking. The rough, jagged fracture surface, along with the secondary cracking, is likely to evidence environmental damage [12]. Figure 6.15 d) shows the fracture surface near the pre-crack region, during the earlier stages of the test, is flat and predominately transgranular/translamellar. However, Figure 6.15 e) shows that as the crack progresses, there is evidence that the fracture becomes more dominated by environmental factors, with a rougher fracture surface and secondary cracking. The evidence of increased influence of time-dependent damage mechanisms at T_{MAX} = 550°C supports the conclusions of researchers, such as Evans and Jones [76][144]. Thus, also supporting that the increased TMFCG rates at 200-550°C, displayed in Figure 6.2, are due to increased effects of time-dependent damage mechanisms at higher temperatures in Ti-6246, and not just a case of general scatter within the data.

6.2.4 CW & ACW

Figure 6.6 showed that under CW and ACW loading conditions, the TMFCG rates were very similar. This suggests that the direction of the diamond cycles, CW (+90°) and ACW (-90°), has no influence on the TMFCG behaviour of Ti-6246. To further determine if this is the case, the fracture surfaces have been analysed and are displayed in Figure 6.16.

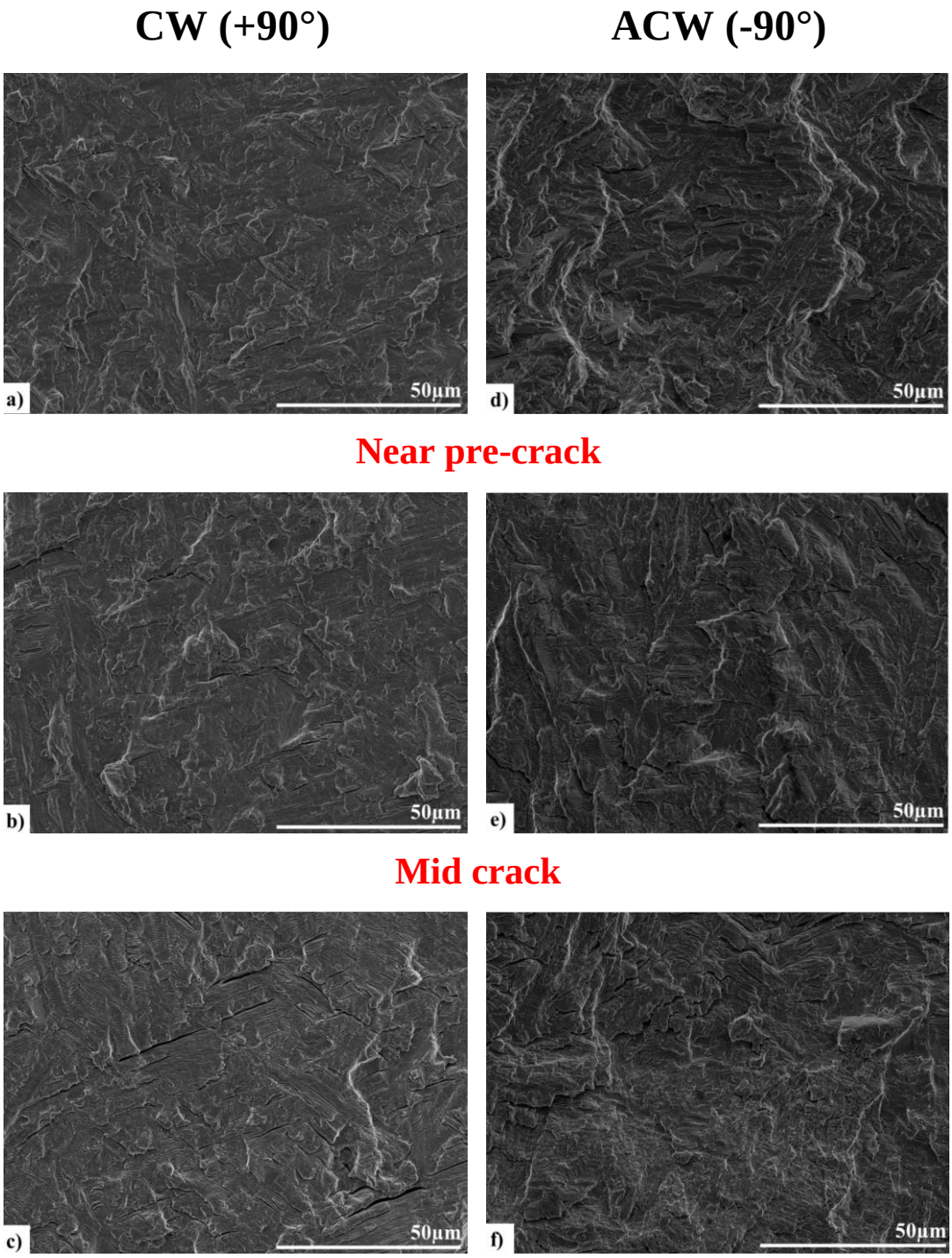

Figure 6.16 Fractography of TMFCG CW (+90°) 200-500°C a) near pre-crack, b) mid crack, c) near crack tip and TMFCG ACW (-90°) 200-500°C d) near pre-crack, e) mid crack and f) near crack tip

Similar to the fractographs of the IP and OP test specimens, Figure 6.16 shows the fracture surface near the pre-crack region, towards the middle of the crack and near the crack tip, of the CW and ACW test specimens. Figure 6.16 shows throughout the crack region there is very little difference between the two fracture surfaces. Both present as predominately transgranular, with no distinctive features to suggest loading direction of the diamond cycles influence the TMFCG behaviour of Ti-6246. This finding compliments the Paris curves displayed in Figure 6.6. Jones et al. noted during TMF testing of RR1000, both fracture surfaces of the CW and ACW test specimens displayed a wavy morphology. This suggests the crack propagated by repeated plastic blunting and resharpening [81]. However, the flat morphology of the fracture surfaces presented in Figure 6.16 cause difficulty in definitively determining the fracture mechanism in the diamond cycles of Ti-6246.

6.2.5 Fatigue Striations

Striations are indicative of fatigue and can provide insight into the FCG rate as the fatigue crack progresses. When studying the fracture surfaces of TMF specimens, researchers have reported fatigue striations formed are less oxidised and are clearly visible in test specimens that have undergone OP loading [81][146]. This is believed to be due to the crack surface being closed and not actively growing under compressive loading at maximum temperature. The surface oxide, reported by researchers, during IP loading conditions is believed to make fatigue striations less visible.

However, analysing the fracture surfaces of both IP and OP specimens tested at 200-500°C, as part of this investigation, fatigue striations are clearly visible in both. Such striations are displayed in Figure 6.17.

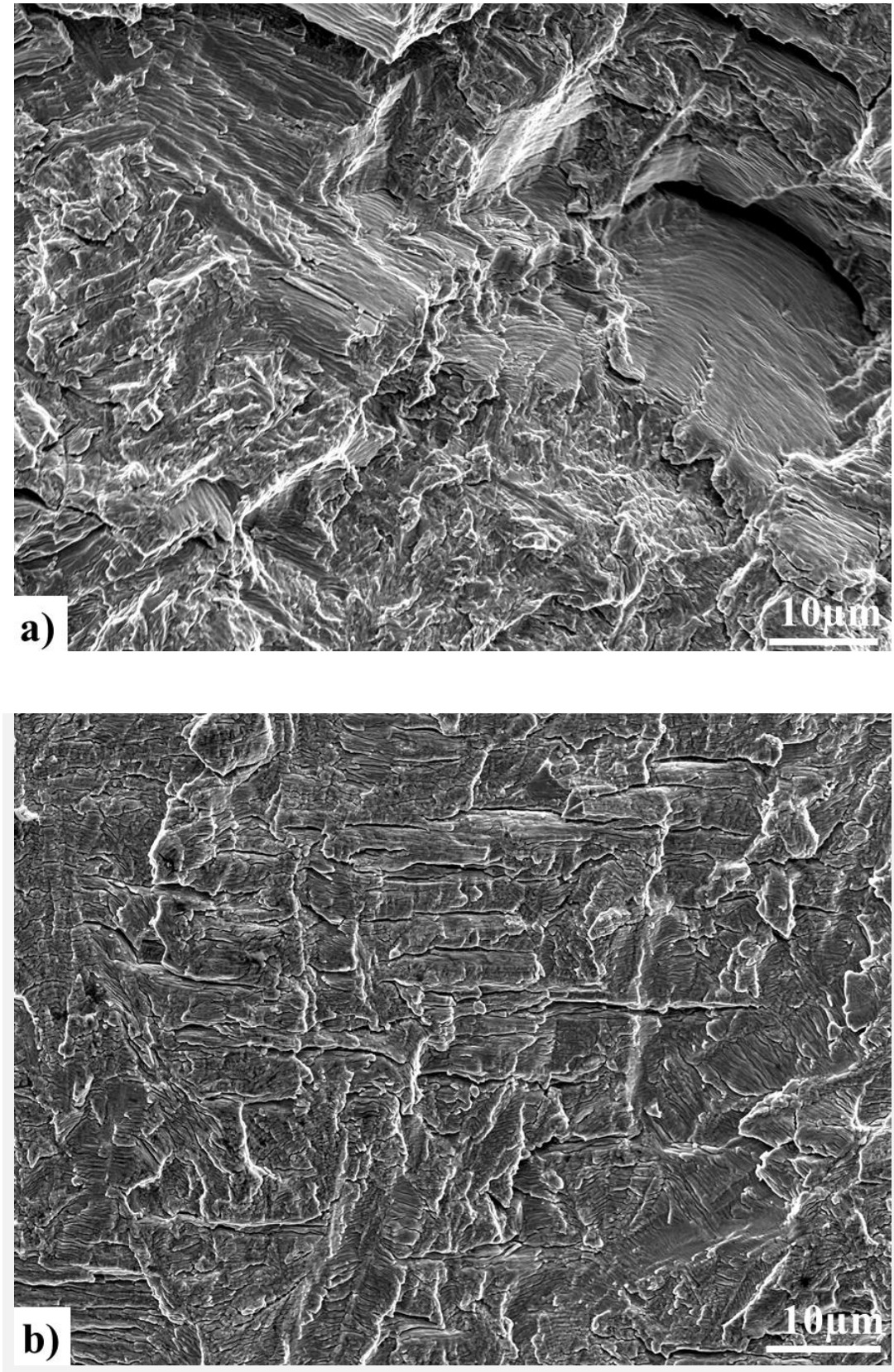

Figure 6.17 Fractography showing fatigue striations on fracture surface of specimens tested under TMFCG conditions 200-500°C, a) IP and b) OP

Analysing the striation spacing as the crack progresses through the specimen, shown in Figure 6.18, it is evident that the spacing increases. Earlier in the crack the striation spacing averages at 0.23µm, shown in Figure 6.18 a), whereas the striation spacing is almost double at an average of 0.4µm nearer the crack tip in Figure 6.18 b). The increased spacing between striations is indicative of the FCG rate increasing and corresponds to the nature of the Paris curves presented as part of this investigation.

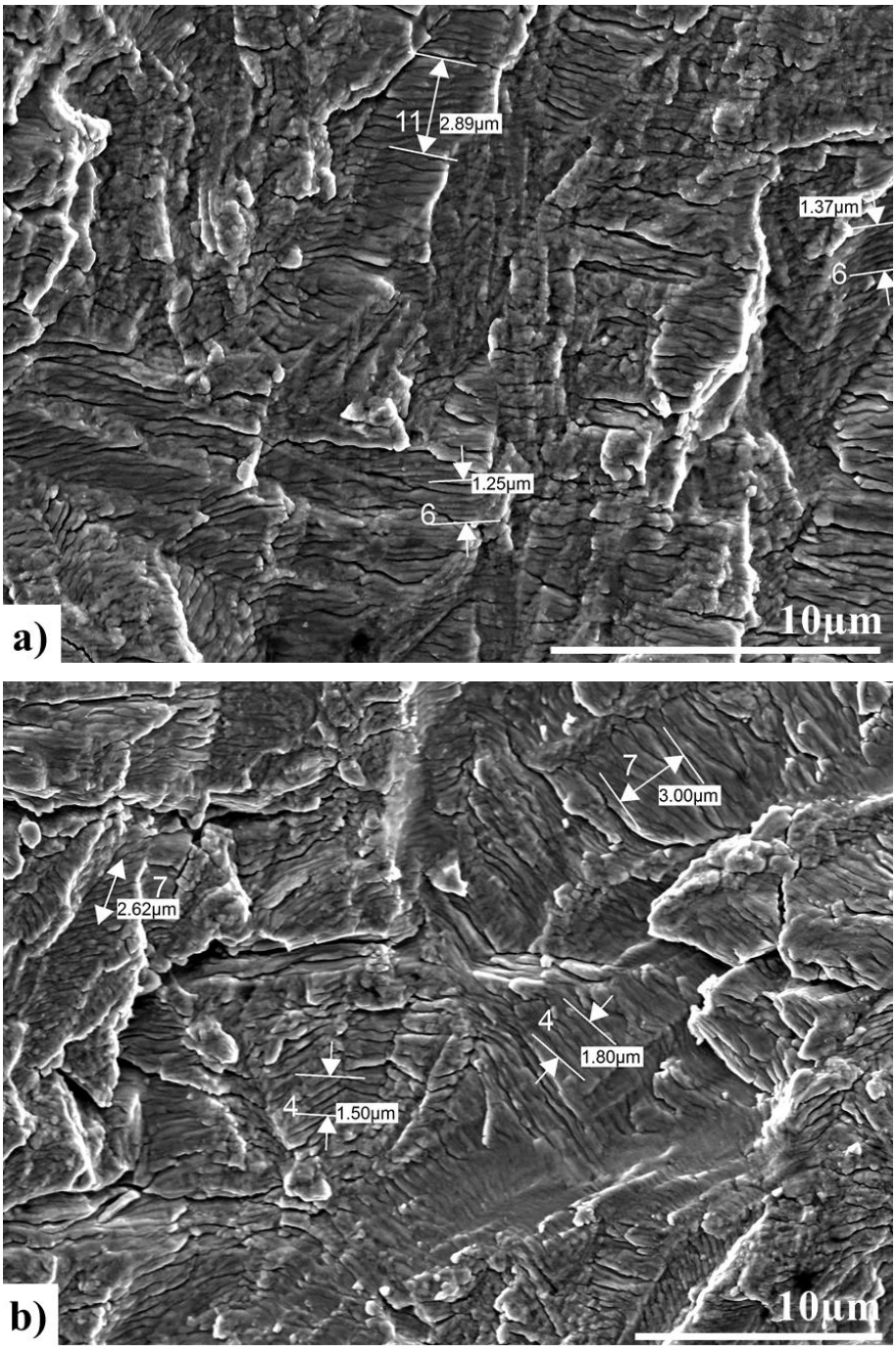

Figure 6.18 Fractographs in which striations have been analysed and the striation spacing measured at a) near the pre-crack and b) near the crack tip

6.2.6 Profilometry

To determine if a difference exists in the roughness of fracture surfaces, profilometry was performed on the fracture surfaces of an IP and OP specimen tested at 200-500°C and 200-550°C, using a Bruker Alicona InfiniteFocus optical microscope. The surface roughness measurements were calculated in accordance to ASME B46.1-2002, Assessment Surface Topography (Blunt/Jiang 2003), Characterisation of Roughness (Stout 2000) and ISO 25178 Areal – Part 2 [138]–[141].

Figure 6.19 shows the surface profiles of specimens tested IP and OP at 200-500°C. It is shown that the IP test condition results in a rougher fracture surface with an average surface roughness (S_a) value of 91µm. This is more than double that of the OP test condition which has a S_a value of 43µm.

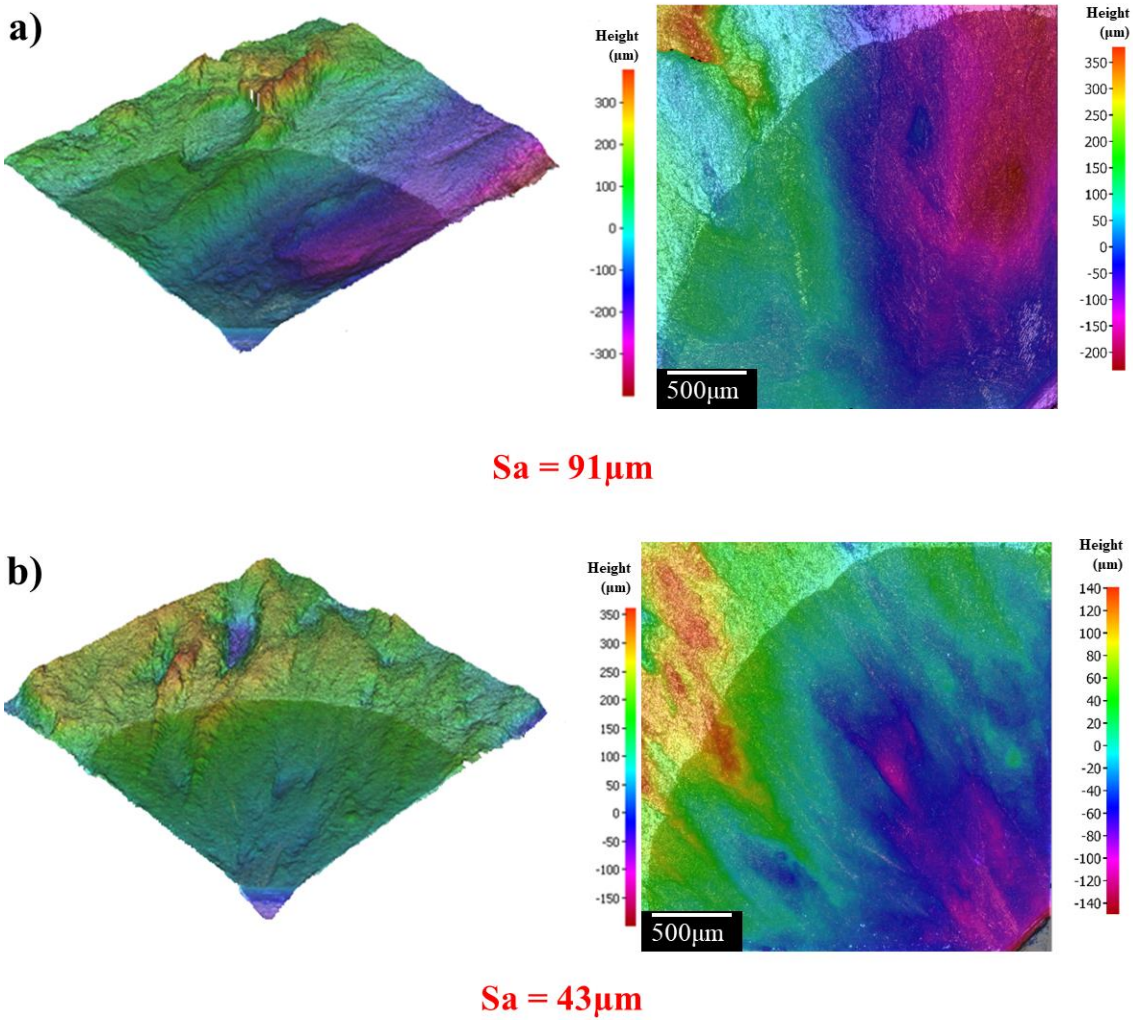

Figure 6.19 Profilometry of TMFCG fracture surfaces a) IP and b) OP at 200-500°C

Figure 6.20 shows at 200-550°C the IP condition results in a rougher fracture surface than OP, with S_a values of 95µm and 40µm, respectively.

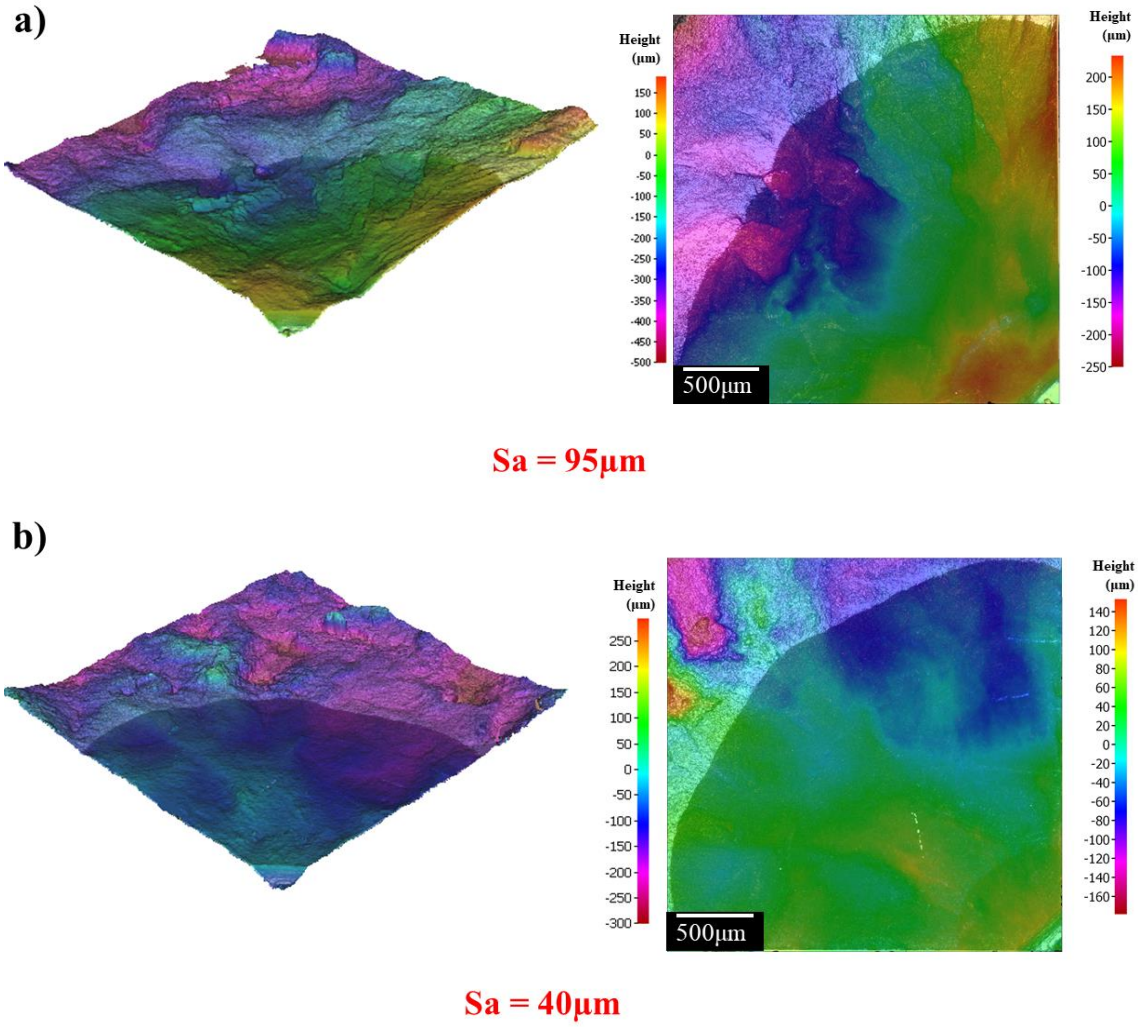

Figure 6.20 Profilometry of TMFCG fracture surfaces a) IP and b) OP at 200-550°C

To determine if this finding is a characteristic of the TMFCG behaviour of Ti-6246 when subject to IP and OP loading conditions, profilometry was performed on repeat IP and OP specimens tested at 200-500°C. Figure 6.21 shows again that the specimen subject to IP loading resulted in a rougher fracture surface with a S_a value of 70µm, whereas the S_a value of the OP test is 29µm.

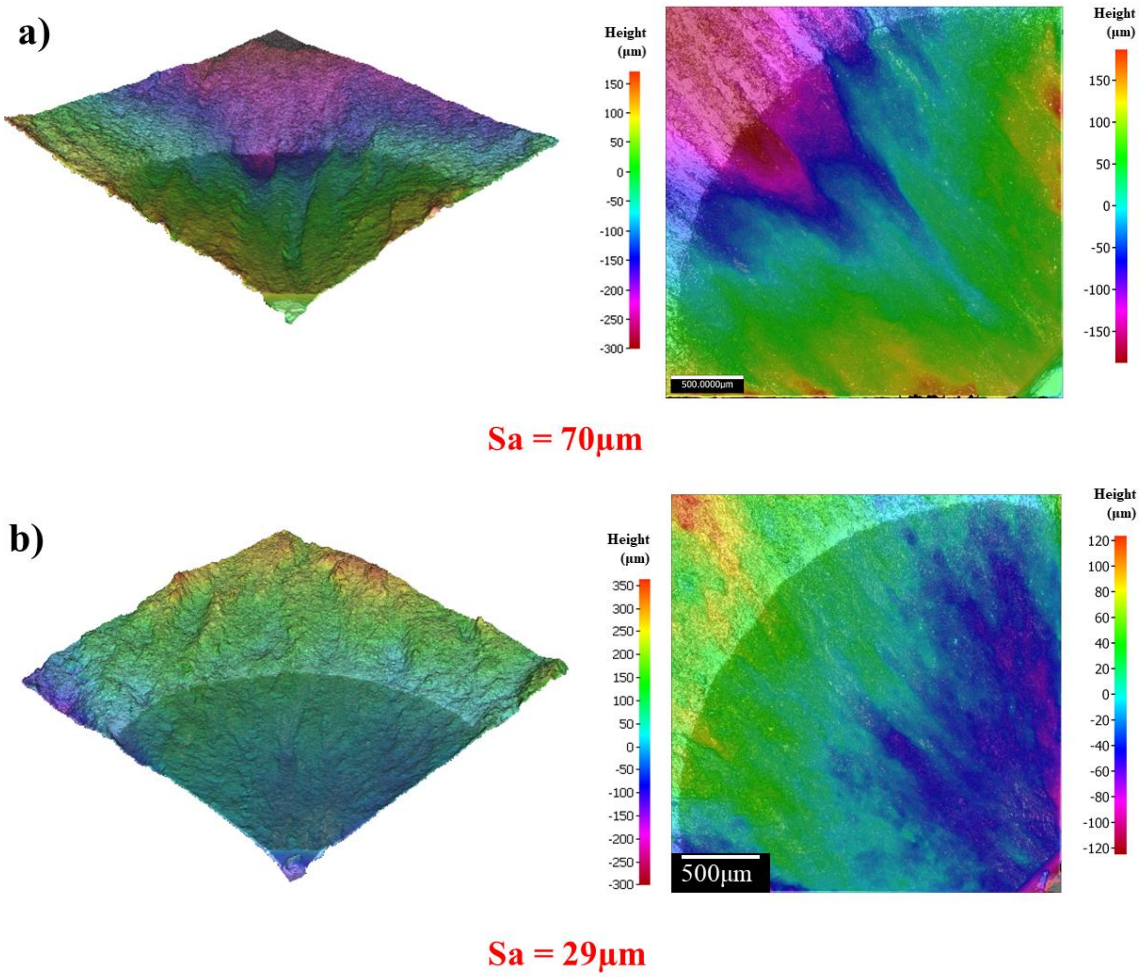

Figure 6.21 Profilometry of repeat TMFCG fracture surfaces a) IP and b) OP at 200-500°C

The profilometry analysis presented as part of this investigation may support the findings that there is a difference in fracture mechanism between IP and OP test conditions. However, to confirm this, more fracture surfaces should be analysed.

The fractography displayed in Figure 6.16 showed no distinguishingly different fracture mechanisms during the CW and ACW diamond cycles, with both presenting as predominately transgranular. Profilometry was performed on the fracture surfaces to determine the resulting surface roughness. The surface profiles are shown in Figure 6.22.

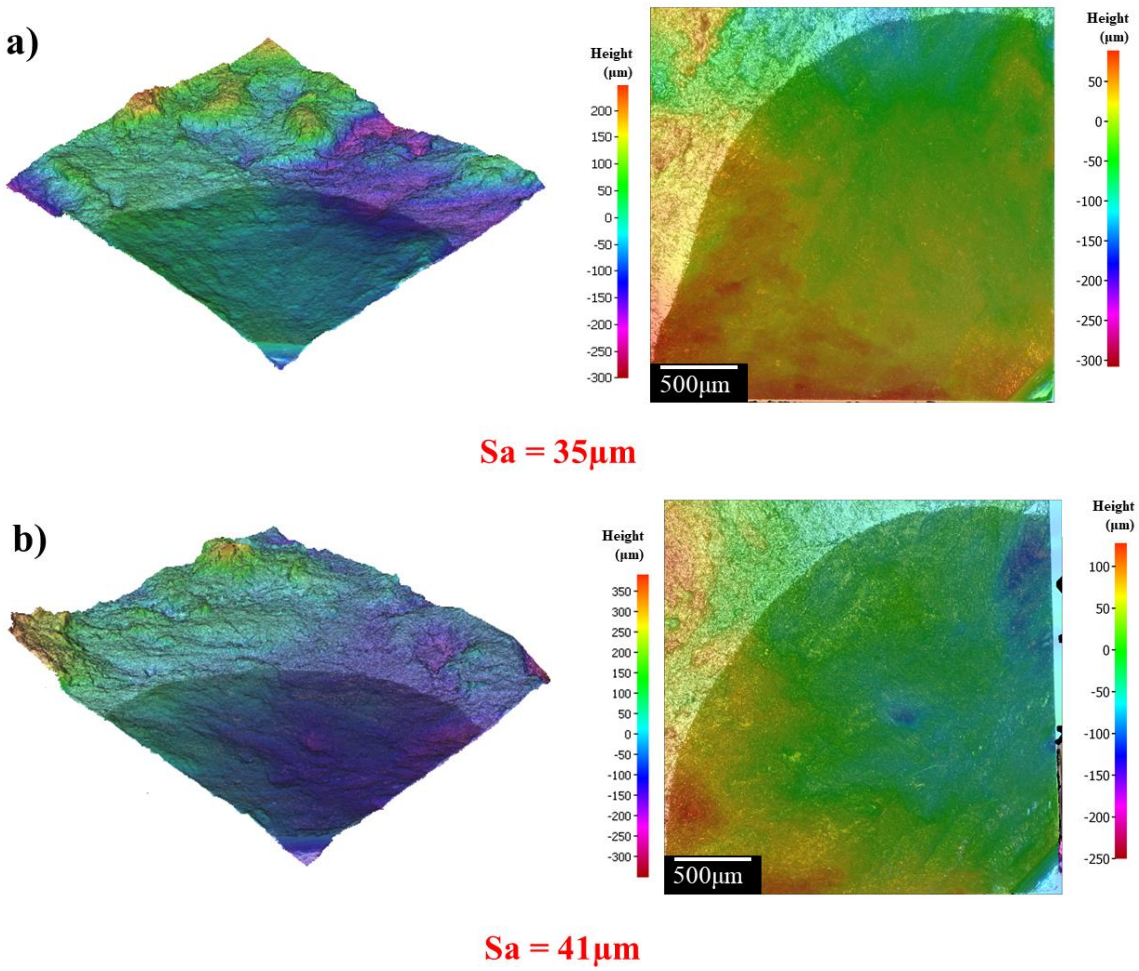

Figure 6.22 Profilometry of TMFCG fracture surfaces a) CW (+90°) and b) ACW (90°) at 200-500°C

Figure 6.22 shows the average surface roughness of the fracture surfaces for CW and ACW test conditions is similar to that obtained from OP test conditions. Along with the fractography displayed in Figure 6.16, the profilometry suggests the fracture mode during the 90° (CW and ACW) tests is predominately transgranular.

6.2.7 Fracture Characterisation Summary

Analyses of the fracture surfaces of Ti-6246 specimens tested under IF and TMF conditions has been conducted in order to characterise the TMFCG behaviour of the alloy. The fractographs show, upon initial inspection that despite the test conditions, Ti-6246 fractures in a transgranular manner. Previous research into nickel superalloys showed a marked transition in fracture mode from intergranular under IP TMF conditions to transgranular under OP TMF conditions. Further fractography of Ti-6246 specimens tested under TMFCG conditions showed that, although predominately transgranular, there are subtle differences between IP and OP. IP test conditions showed to be more interlamellar in nature, whereas OP more translamellar. Initial profilometry also supports this finding, with IP test conditions resulting in a rougher fracture surface than OP test conditions.

6.3 Microstructural Analysis

As part of this investigation, post-test analysis of the microstructure has been conducted. IP and OP TMFCG conditions pose as the two extreme cases and thus, the primary focus of the microstructural analysis was to better understand the damage mechanisms involved during IP and OP testing at 200-500°C and 200-550°C.

The fractography displayed in Figure 6.13 - Figure 6.15, showed subtle differences in the fracture surfaces between IP and OP loading conditions. Thus, by studying the microstructure through which the crack has propagated, a better understanding of the damage mechanisms involved may be achieved. Figure 6.23 of the crack propagating through the IP specimen tested at 200-500°C, shows secondary cracking branching from the primary crack. These cracks are shown to form at α-β interfaces, and as suggested by Whittaker et al. [12], is likely to be due to the environment. During IP conditions, the crack is opened under tensile loading as the temperature increases to a maximum. These conditions promote processes, such as oxidation, which embrittle the surrounding material, resulting in secondary cracking along the weaker α-β interfaces when cycled. The evidence of this cracking along the α-lath boundaries also supports the subtle interlamellar cracking seen in the fractography presented earlier.

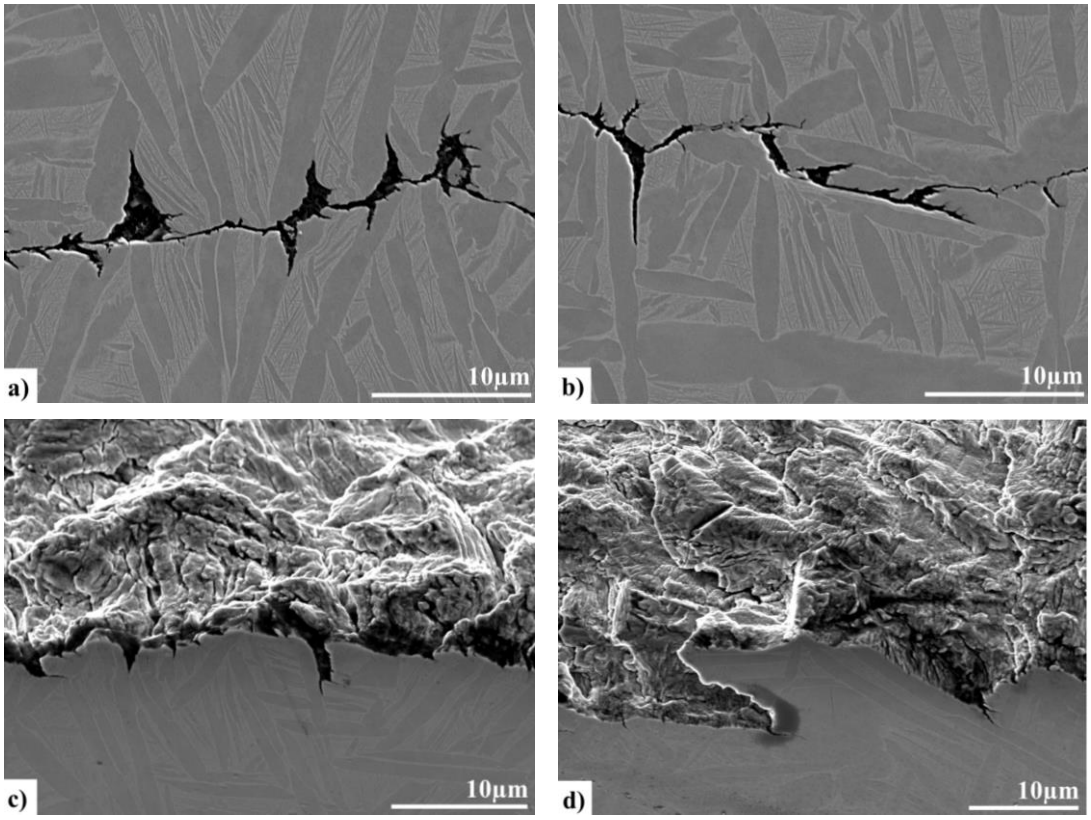

Figure 6.23 Micrographs along the fatigue crack of an IP TMFCG specimen tested at 200-500°C. Both a) and b) show evidence of interface cracking at different locations. c) and d) capture the fracture surface and microstructure and display interface cracking

As well as branching, Figure 6.23 a) also shows microstructural distortion near the crack plane. This phenomenon is shown more clearly in Figure 6.24 and suggests severe plastic deformation exists within this region [148].

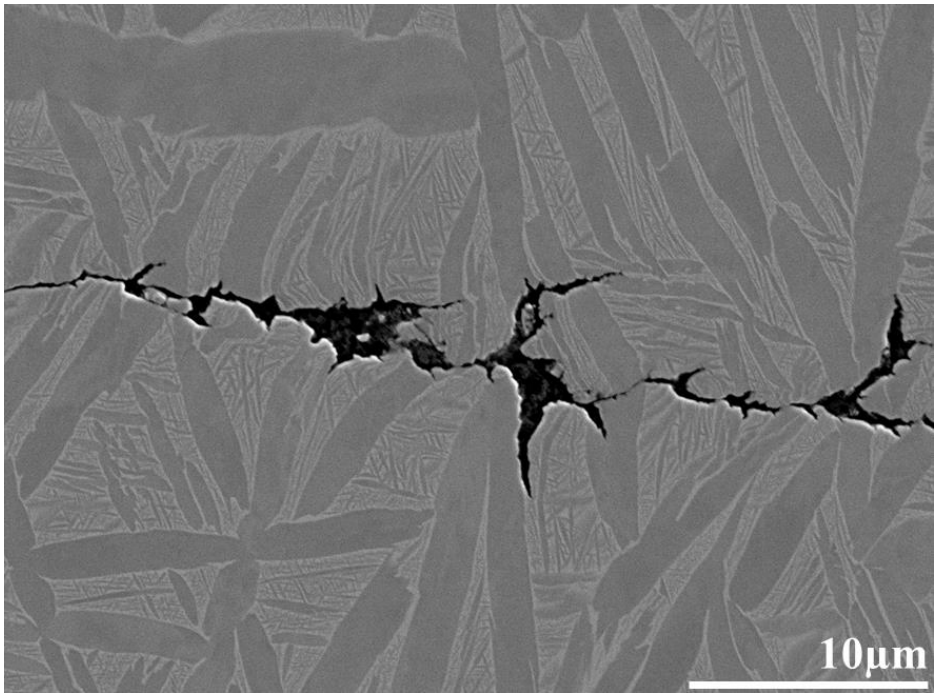

Figure 6.24 Micrograph along the fatigue crack of an IP TMFCG specimen tested at 200-500°C, showing microstructural distortion near the crack plane

Figure 6.25 shows that as the crack progresses to intermediate ΔK values, the crack path begins to look more destructive with evidence of more severe crack branching, as well as the primary crack diverting. Some of the longer branched cracks appear to occur along α-lath boundaries, whereas others appear to propagate through α-laths.

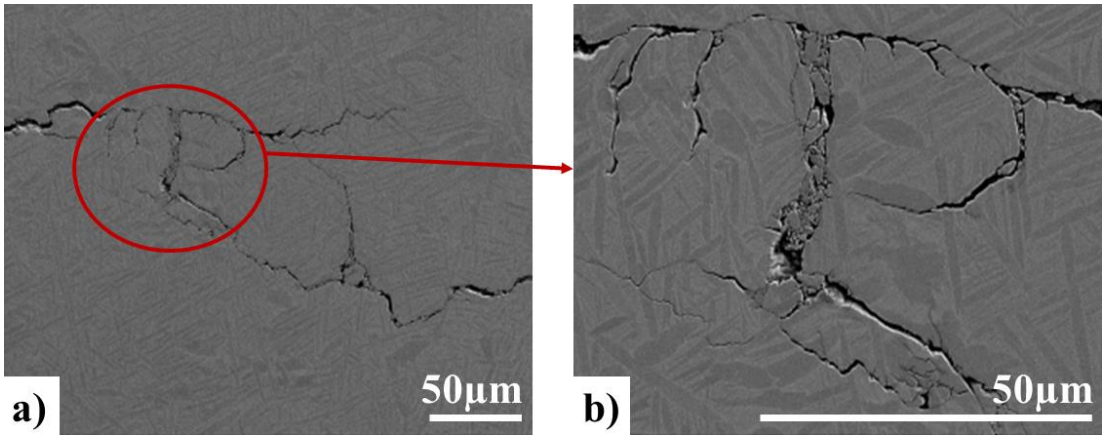

Figure 6.25 Micrographs along the fatigue crack of an IP TMFCG specimen tested at 200-500°C. a) shows secondary crack as well as the primary crack diverting. b) shows the region outlined, in more detail

Figure 6.26 shows evidence of tearing, away from the primary crack. This could be indicative of creep and environmental damage. Similar features were reported by Evans et al. in their study of fatigue and creep behaviour of Ti-6246 and such damage emphasises the nature of environmental damage, whilst highlighting the importance of stress in promoting the damage [76]. This is particularly true in the case of IP loading conditions.

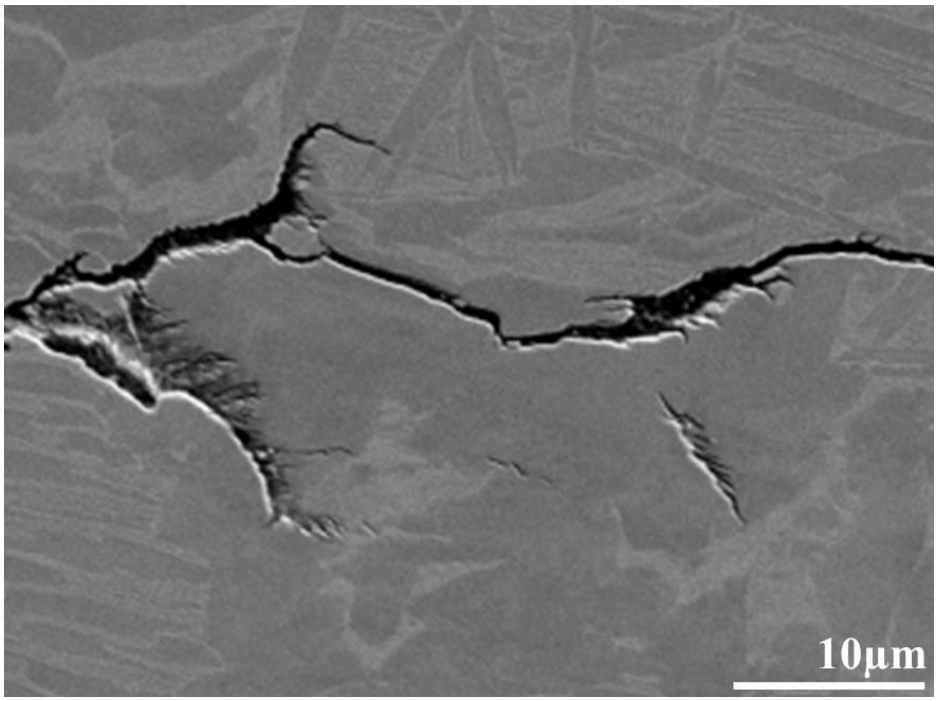

Figure 6.26 Micrograph along the fatigue crack of an IP TMFCG specimen tested at 200-500°C, showing tearing away from the primary fatigue crack

Figure 6.27 shows that OP testing at 200-500°C experiences a much less severe degree of secondary cracking and crack branching, compared to IP. It is also evident that the crack is propagating predominately through the α-laths, particularly during the earlier stages of FCG, as shown in Figure 6.27 a) and b). This finding compliments the fractography of the OP TMFCG specimen, which shows a flatter, more translamellar fracture mechanism.

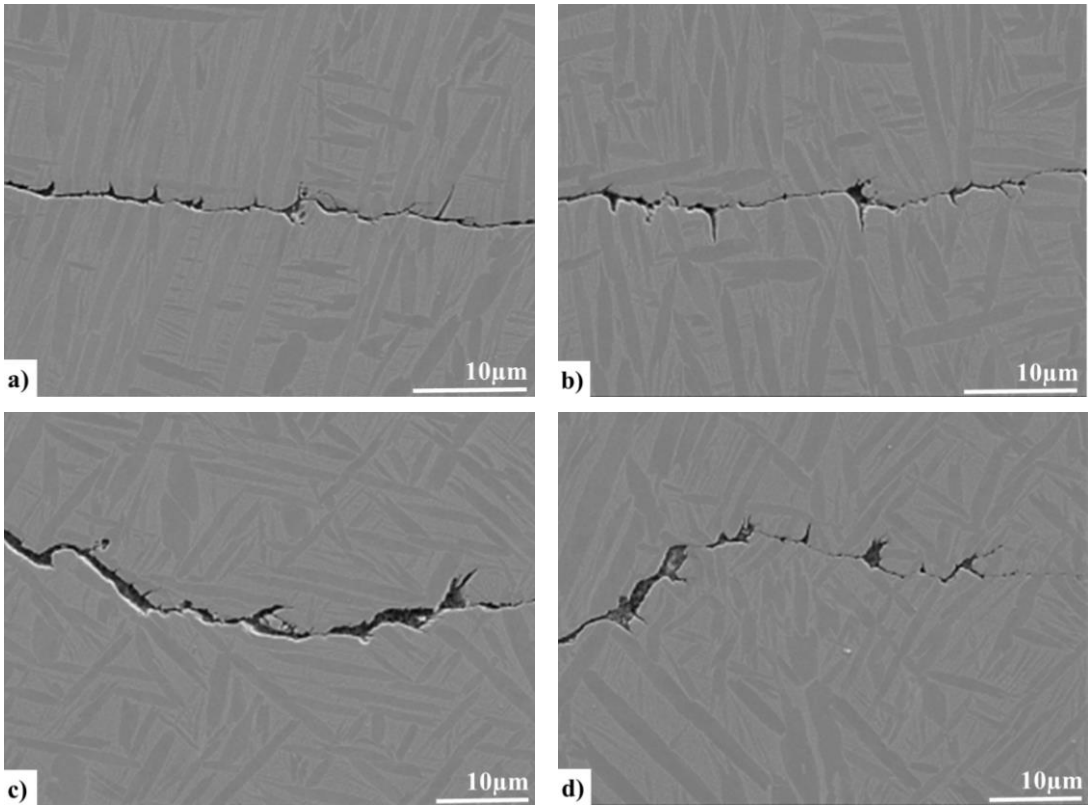

Figure 6.27 Micrographs along the fatigue crack of an OP TMFCG specimen tested at 200-500°C. All images show short secondary interface cracking

The micrographs displayed in Figure 6.27 also show distortion in the microstructure near the primary fatigue crack. This again suggests high levels of strain around the crack plane [148].

Figure 6.27 b) and c) also show evidence of the formation of creep damage ahead of the crack tip [76]. The formation of creep voids is shown more clearly and appears more prominent at higher ΔK values, as shown in Figure 6.28.

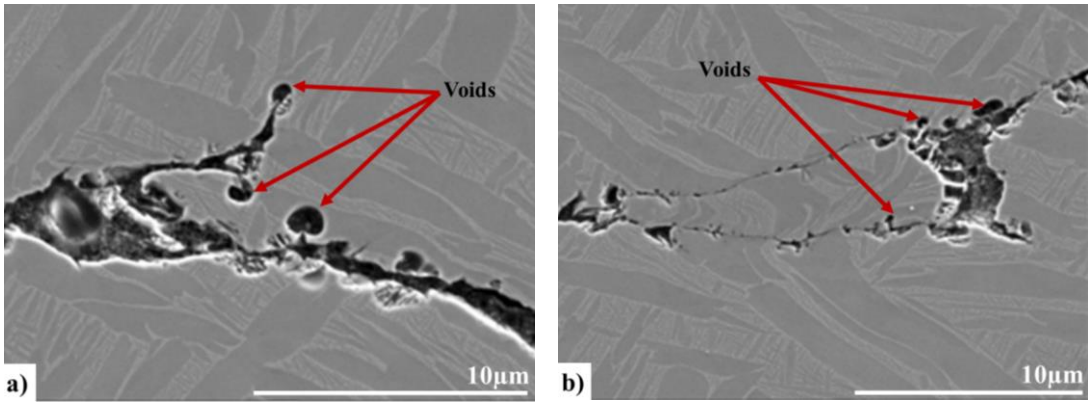

Figure 6.28 Micrographs along the fatigue crack of an OP TMFCG specimen tested at 200-500°C. Both a) and b) show evidence of creep damage ahead of the crack tip, with the formation of voids

The evidence of creep becomes more prominent as the crack progresses during OP conditions and compliments the FCG rates displayed in Figure 6.4. This evidence of creep damage under OP test conditions is interesting, as it would suggest that the creep voids are forming at high temperature and minimum stress which further demonstrates the complexity of TMFCG conditions.

Figure 6.29 shows at 200-550°C, the resulting crack path during IP conditions is more tortuous than at T_{MAX} = 500°C. Titanium alloys have a high affinity to oxygen, and when exposed to higher temperatures, the rate at which an oxide layer can form is accelerated. Under IP loading at T_{MAX} = 550°, it is likely that a brittle oxide layer has formed, to a greater extent than at T_{MAX} = 500°C.

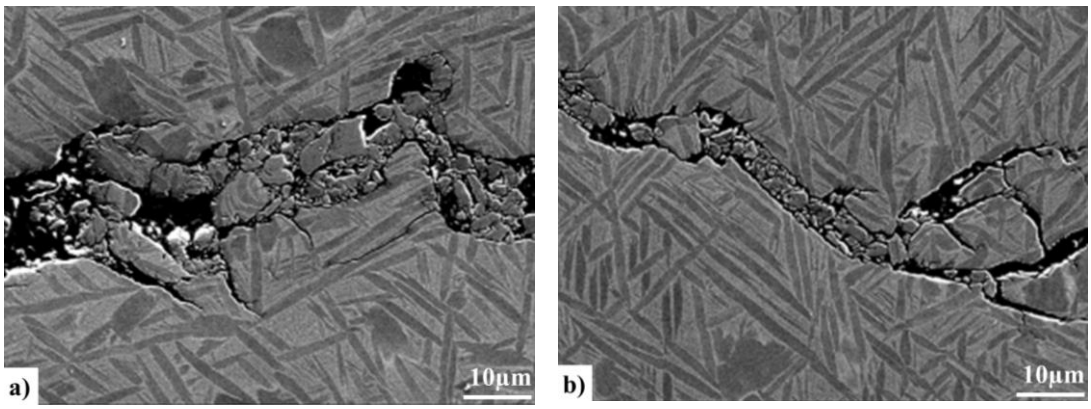

Figure 6.29 Micrographs along the fatigue crack of an IP TMFCG specimen tested at 200-550°C. Both a) and b) show evidence of oxidation damage

Figure 6.30 a) shows that during IP loading at 200-550°C, as the fatigue crack propagates, the secondary cracks have been able to grow for longer. This could be evidence of increased creep interaction ahead of the crack tip. As the frequency of the TMFCG tests is slow (0.0125Hz), it is likely the time the specimen is held above a particular level of stress is allowing for the conversion of elastic strain to plastic strain, i.e., stress relaxation occurs. This stress relaxation results from the creep deformation that occurs ahead of the crack tip, forming features such as voids, as shown in Figure 6.28. These creep features can in turn interact with a propagating fatigue crack to result in an enhanced crack growth rate [149].

The distortion in the microstructure around the crack, shown in Figure 6.30 b) again, suggests the material has undergone extensive plastic deformation.

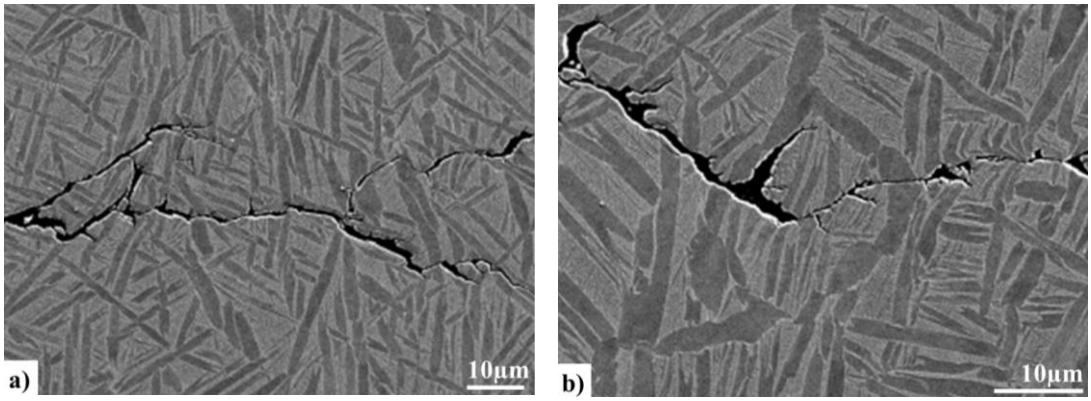

Figure 6.30 Micrographs along the fatigue crack of an IP TMFCG specimen tested at 200-550°C. Both a) and b) show evidence of possible creep interaction ahead of the crack tip, resulting in secondary cracking

Figure 6.31 shows how the crack has propagated through a specimen tested under OP TMFCG conditions at 200-550°C. It is shown in Figure 6.15 that at T_{MAX} = 550°, OP test conditions result in more environmental damage than at T_{MAX} = 500°C. It is evident from Figure 6.31 that secondary cracking is far more prominent at T_{MAX} = 550°C and unlike that shown in Figure 6.27, is more interlamellar. This α-β interface cracking is suggested by Whittaker et al. to be due to the environment and such evidence also further supports the conclusions of Evans and Jones [12][76][144].

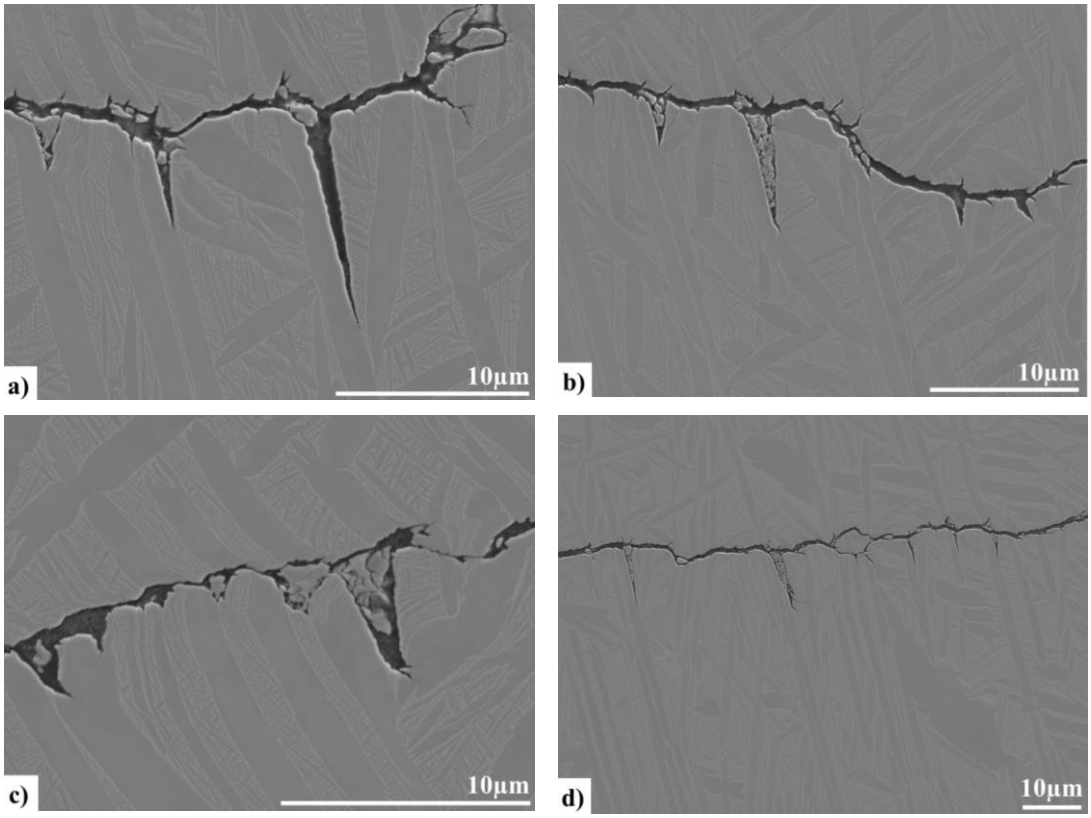

Figure 6.31 Micrographs along the fatigue crack of an OP TMFCG specimen tested at 200-550°C. a) – d) show secondary cracking along the α-β interfaces, as well as material debris due to the environment

Figure 6.32 shows that during OP TMFCG testing at T_{MAX} = 550°C, the primary crack has been able to deviate as it propagates, demonstrating a higher energy, more damaging crack than that seen at T_{MAX} = 500°C. Such evidence further supports the increased FCG rates displayed in Figure 6.4.

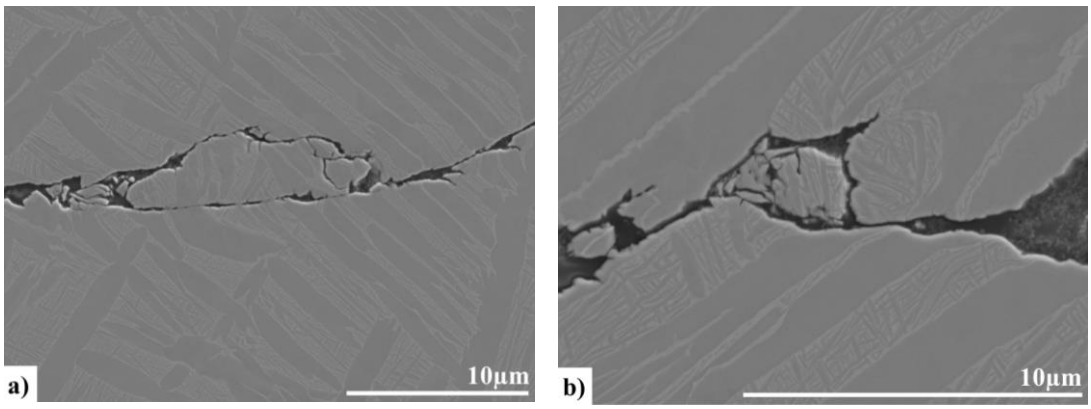

Figure 6.32 Micrographs along the fatigue crack of an OP TMFCG specimen tested at 200-550°C. Both a) and b) show evidence of the primary fatigue crack deviating

6.3.1 Optical Texture Analysis

In general, when subjected to fatigue, the mechanical properties of titanium alloys are largely dependent on the microstructure and the crystallographic texture of the material [150]. It has been reported that fatigue crack initiation and growth is greatly influenced by the microstructure, grain size, grain orientation and grain boundary geometry [151].

It is common practice to etch a specimen to reveal microstructural features of interest. In an attempt to analyse the crystallography of the Ti-6246 specimens used in this investigation, polarised light microscopy was coupled with a colour tint etch, achieved using a modified Weck's reagent. It is very difficult to quantify the crystallography of a material using polarised light, however using a colour tint etch, it can be possible to qualitatively analyse the grain orientation and texture within a material [135]. Figure 6.33 shows optical images of a Ti-6246 specimen, tested IP at 200-500°C that has been etched with a modified Weck's reagent, resulting in a colour tint.

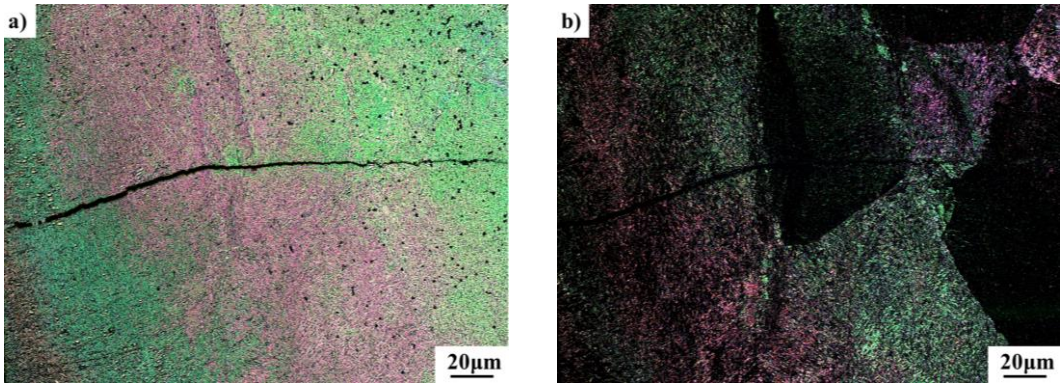

Figure 6.33 Image of IP 200-500°C Ti-6246 specimen that has been colour tint etched with a modified Weck's reagent taken using the Zeiss Primotech, a) unpolarised, b) polarised

Figure 6.33 a) shows the etched Ti-6246 specimen in an unpolarised light. The colour tint has exposed different colours throughout the specimen. According to research, such colours can correspond to grain orientation [152][153]. Figure 6.33 b) shows the specimen under a polarised light, and it is possible to qualitatively analyse the variation in lath orientations, with the difference in shading across the specimen. Under polarised light, differently orientated packets of α-laths that have emerged from prior β grains are made visible. The crack has propagated through areas of different colours, as well as both lightly illuminated packets of α-laths and dark packets of α-laths (under polarised light). This would suggest that α-lath orientation has not had a great influence on the crack path. However, to fully appreciate this approach to analysing a material's texture, further investigation and understanding into the qualitative technique is required.

6.3.2 EBSD Analysis

EBSD is a microstructural-crystallographic characterisation technique that can provide quantitative microstructural information about the crystallographic nature of both crystalline and polycrystalline materials. The technique can provide copious amounts of information about a material, including structure, crystal orientation, phase information and any strain within the material and has been used as part of this investigation to aid the characterisation of the TMFCG behaviour of Ti-6246.

6.3.3 Inverse Pole Figure (IPF) Maps

Inverse pole figure (IPF) maps show the crystallographic orientations in terms of sample coordination system, thus allowing for easy interpretation in relation to applications such as rolling direction. The IPF component uses a basic RGB colour scheme where each colour represents a different grain orientation. For the hexagonal (α) phase, red, green and blue are designated to grains whose <0001>, <$\bar{1}2\bar{1}0$> or <$01\bar{1}0$> axes, respectively, are parallel to the projection direction of the IPF. For the cubic (β) phase, red, green and blue are designated to the <100>, <110> or <111> axes, respectively [154]. Figure 6.34 - Figure 6.37 display the IPF maps for the Ti-6246 specimens tested IP and OP at 200-500°C and 200-550°C.

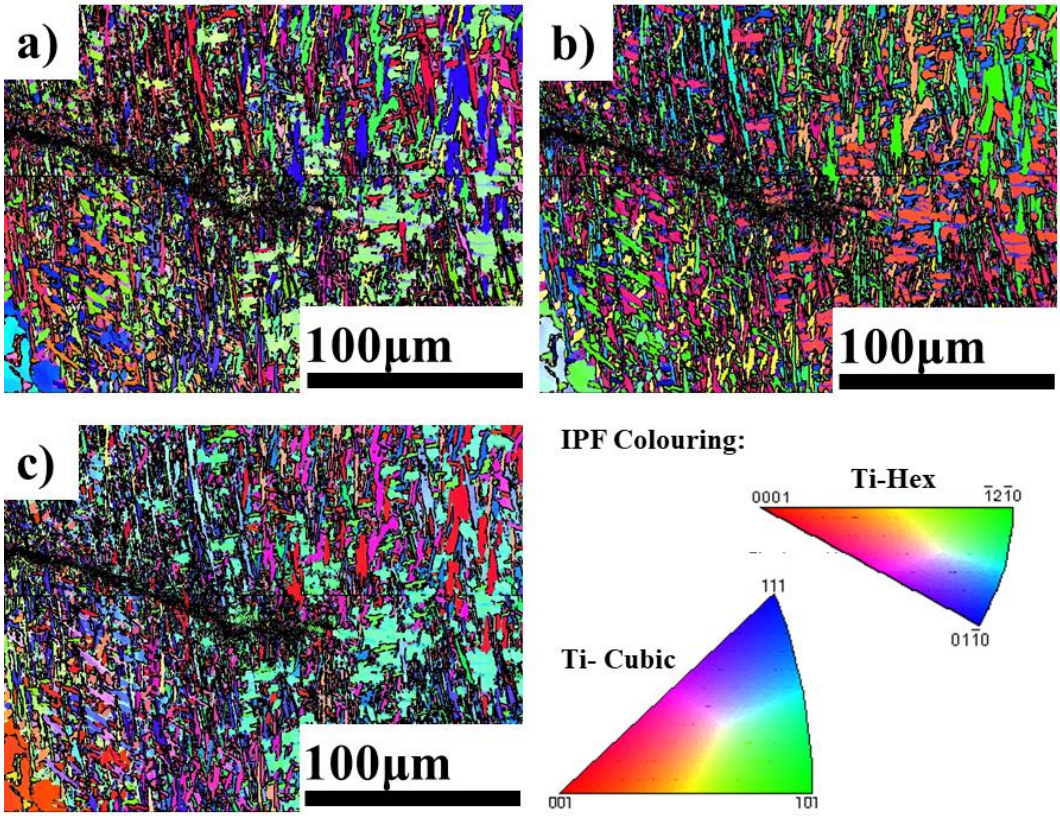

Figure 6.34 IPF maps of Ti-6246 tested IP 200-500°C in the a) x-plane (IPF||x), b) y-plane (IPF||y) and c) z-plane (IPF||z)

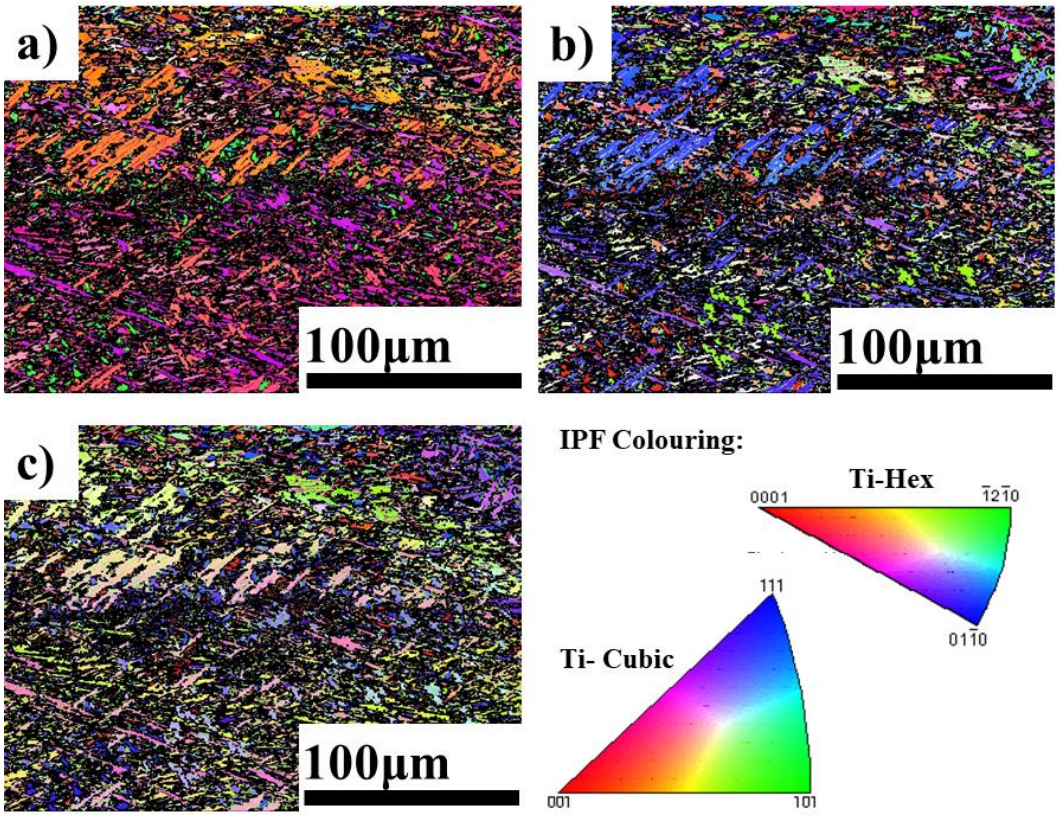

Figure 6.35 IPF maps of Ti-6246 tested OP 200-500°C in the a) x-plane (IPF||x), b) y-plane (IPF||y) and c) z-plane (IPF||z)

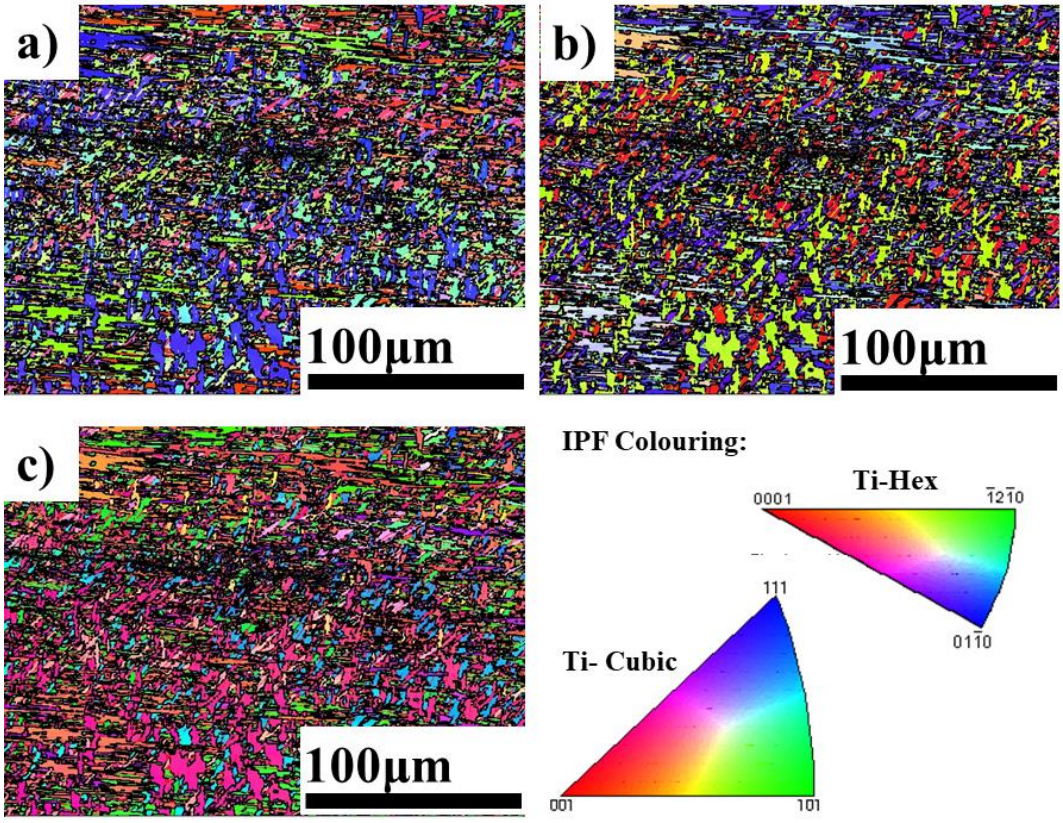

Figure 6.36 IPF maps of Ti-6246 tested IP 200-550°C in the a) x-plane (IPF||x), b) y-plane (IPF||y) and c) z-plane (IPF||z)

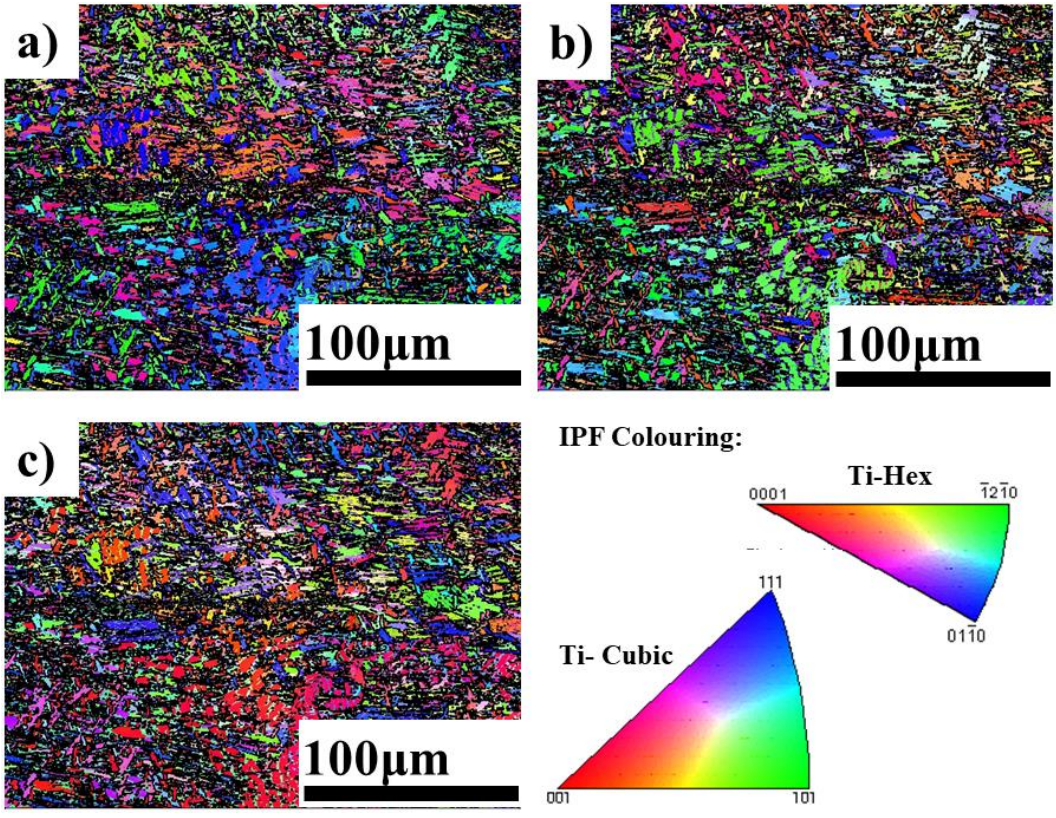

Figure 6.37 IPF maps of Ti-6246 tested OP 200-550°C in the a) x-plane (IPF||x), b) y-plane (IPF||y) and c) z-plane (IPF||z)

Figure 6.34 – Figure 6.37 shows, to some extent, that the material displays texture. This is particular prevalent in Figure 6.35 a) and Figure 6.36 c), in which both maps are largely dominated by similar colours and thus, displaying laths of similar orientations. The scale on which the IPF maps have been generated create difficulty in determining the influence of texture on FCG. However, as the specimens have come from the same batch of material and have been processed in the same manner, it is likely that the level of texture is similar across all specimens. This, coupled with the mapped differences across the four specimens, would suggest that the FCG under IP and OP conditions is not influenced strongly by localised texture. Nevertheless, further investigation would be required to confirm this.

6.3.4 IPFs

The contoured IPFs corresponding to the IPF||x maps displayed in Figure 6.34 a), Figure 6.35 a), Figure 6.36 a) and Figure 6.37 a) are displayed in Figure 6.38 and provide another method to visualise texture within a material. The contoured IPFs display contour levels in multiples of uniform distribution (MUD) and using an RGB system, it is possible to determine areas of high density. It is possible from Figure 6.38 to identify the preferred orientations for both the HCP (α) phase and BCC (β) phase, with the MUDs ranging from 0 to 9.11. However, it is important to note that one IPF is only a partial representation of the texture and for a more complete representation, the IPFs for all directions should be analysed.

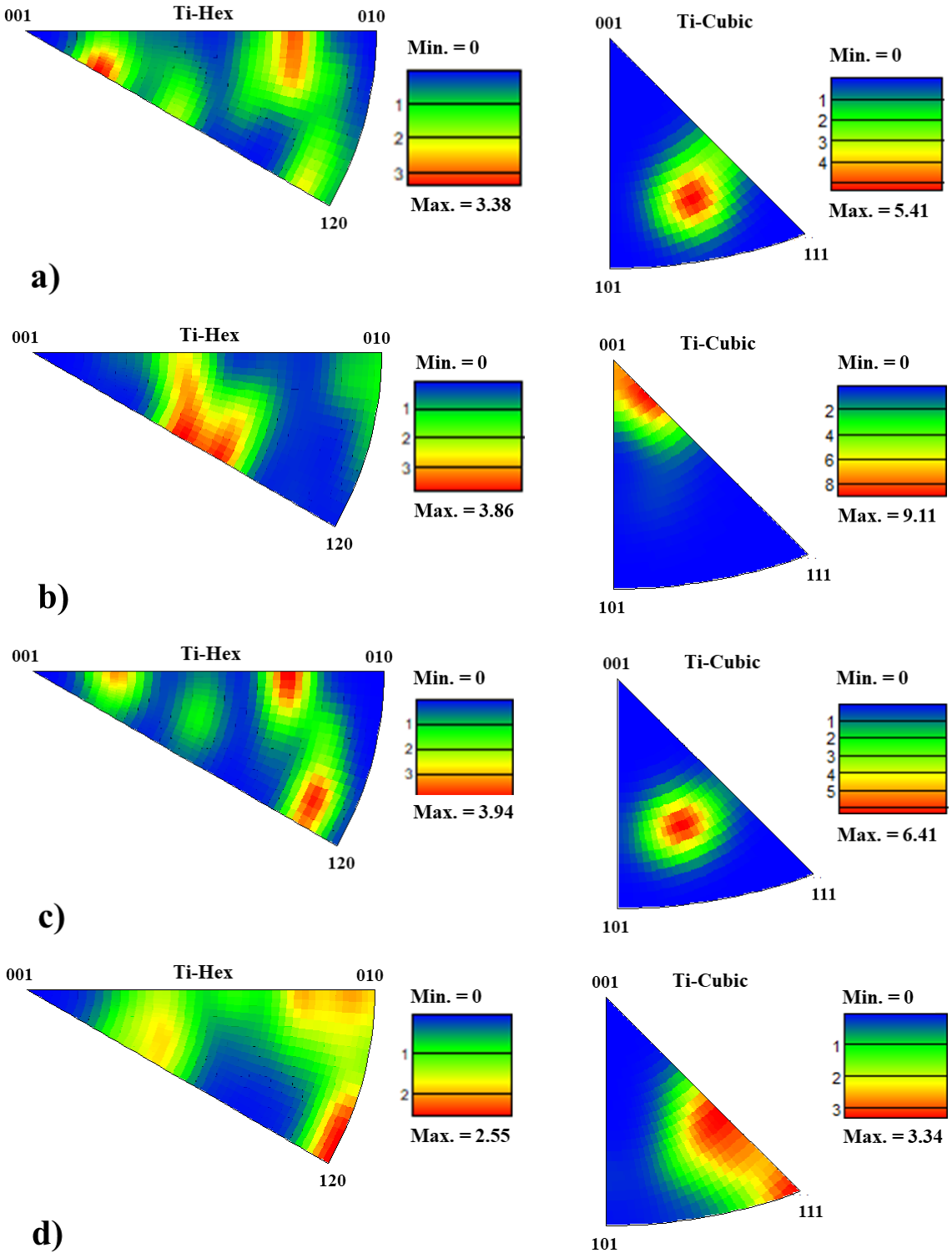

Figure 6.38 contoured IPFs, corresponding to the IPF||x maps of Ti-6246 specimens tested a) IP 200-500°C, b) OP 200-500°C, c) IP 200-550°C and d) OP 200-550°C

6.3.5 Phase maps

Ti-6246 is an α+β alloy that due to its relatively high β content, is argued by some researchers to be a near-β alloy [22]. As a part of this investigation, the data collected from the ESBD analysis was used to determine if the phases within the material influence the crack path and crack growth rate. Figure 6.39 displays the phase maps of the crack tips of the Ti-6246 specimens analysed.

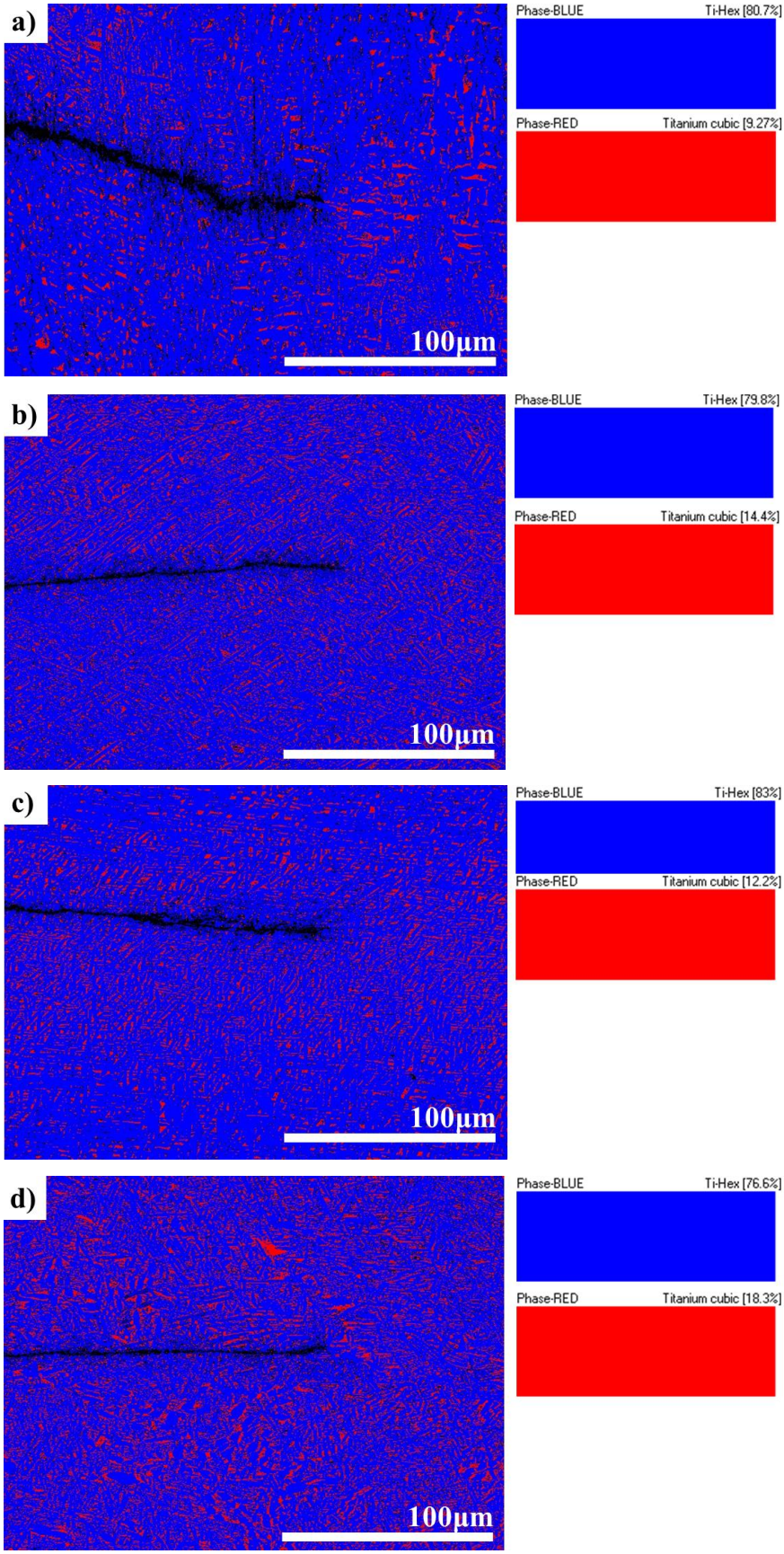

Figure 6.39 Phase maps of the crack tips of Ti-6246 specimens tested a) IP 200-500°C, b) OP 200-500°C, c) IP 200-550°C and d) OP 200-550°C

The phase maps presented in Figure 6.39 displays the α and β phases as blue and red, respectively. The maps show that the phases within the material do not have a noticeable influence on the crack path. Figure 6.39 a) – d) show that the crack has propagated through both the α and β phases under both IP and OP conditions and at T_{MAX} = 500°C and 550°C.

6.3.6 Strain contouring maps

The microstructural analysis presented earlier in 6.3 highlighted microstructural distortion around the crack plane, indicating high levels of strain in that area. Thus, to gain a better understanding of the strain distribution along the crack path and at the crack tip, strain contouring maps were plotted for both IP and OP test specimens at 200-500°C and 200-550°C. These maps are shown in Figure 6.40.

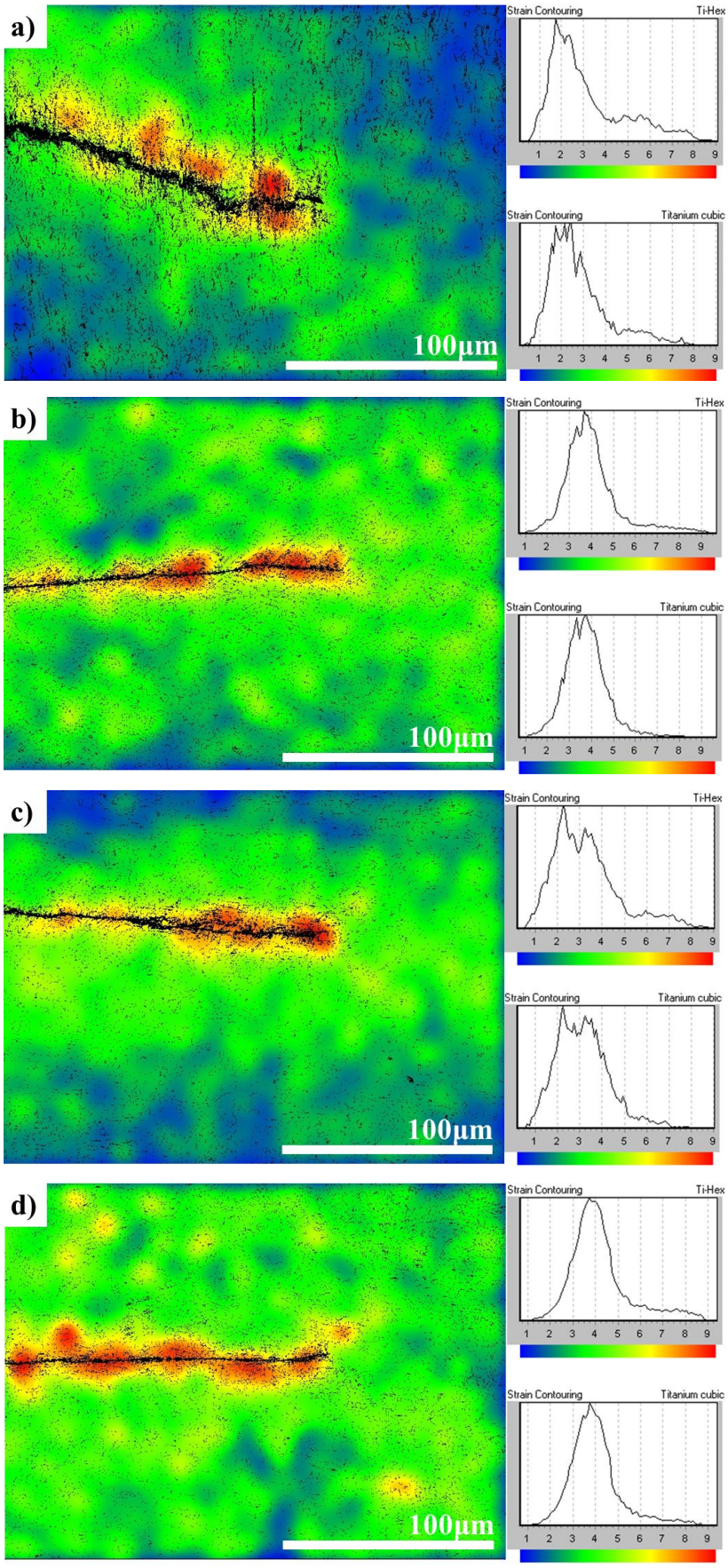

Figure 6.40 Strain contouring maps of the crack tips of Ti-6246 specimens tested a) IP 200-500°C, b) OP 200-500°C, c) IP 200-550°C and d) OP 200-550°C

Figure 6.40 shows that under both IP and OP conditions at 200-500°C and 200-550°C high levels of strain are retained around the crack plane. This corresponds with the findings highlighted in the micrographs displayed in 6.3. It is evident from Figure 6.40 a) and c), that under IP conditions the strain retention lessens in the bulk material, away from the crack plane. However, Figure 6.40 b) and d) shows that this is not the case under OP conditions, and in fact the bulk material retains higher levels of strain than the specimens tested IP. This finding could again support the theory that stress relaxation, due to creep, occurs under IP conditions. Creep damage ahead of the crack tip could cause stress to be relieved throughout the specimen, result in lower levels of strain in the material away from the crack plane.

6.3.7 EDS

EDS is a chemical microanalysis technique used in conjunction with a SEM and has been used to analyse both IP and OP test specimens at 200-500°C and IP 200-550°C. The purpose of this analysis is to gain a better understanding of the oxygen presence within the material and its contribution to oxidation damage during testing.

Figure 6.41 shows the EDS maps of the specimens, in which the alloying elements and oxygen are displayed.

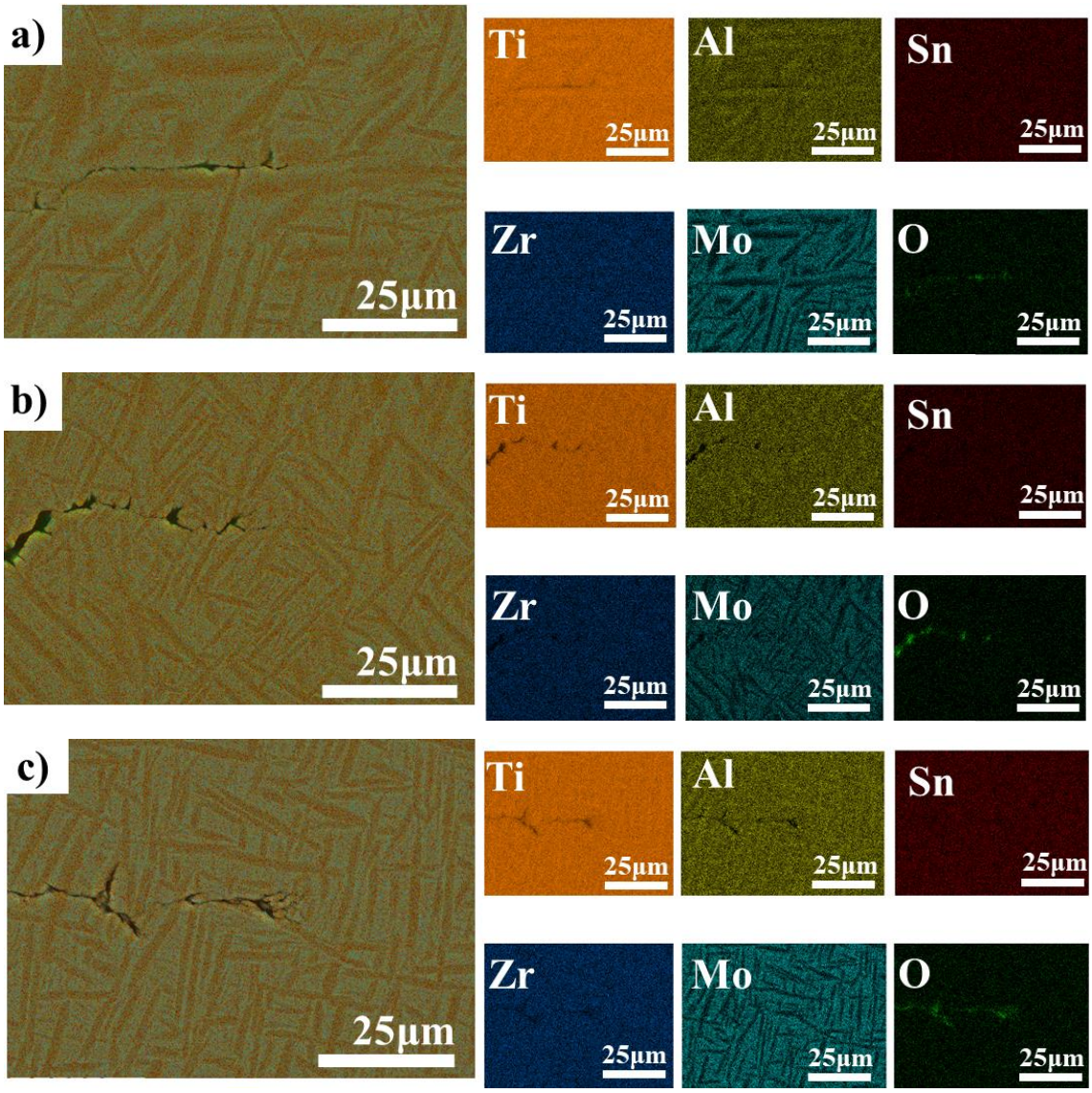

Figure 6.41 EDS maps of the crack tips of Ti-6246 specimens tested a) IP 200-500°C, b) OP 200-500°C and c) IP 200-550°C

Figure 6.41 shows the presence of oxygen which is more heavily concentrated along the crack in all specimens, as would be expected. Figure 6.41 c) shows that this concentration may be greater at T_{MAX} = 550°C, however further analysis would be required to determine the reality of this. It is also unclear as to whether or not an oxide layer has formed beyond the crack plane and thus, further investigation into the oxidation growth would be beneficial to aid the understanding of this damage mechanism.

6.3.8 Microstructural Analysis Summary

Analysing the microstructures of specimens tested, the importance of crack tip has become apparent. By assessing the crack at the tip, it can be possible to better understand the damage mechanisms the material has experienced. Figure 6.42 a) and b) show the crack tips of IP and OP test specimens, respectively, at 200-500°C. It is possible to see some crack branching in both micrographs, with the IP test showing the crack's tendency to follow the α-β interface, which could be attributed to by oxidation [12]. Figure 6.42 c) shows that at the increased T_{MAX} = 550°C, the IP test specimen experiences extensive crack branching at the crack tip. The OP test specimen, displayed in Figure 6.42 d), shows that at T_{MAX} = 550°C, the secondary cracks are able to progress and deviate further from the original crack path. Both Figure 6.42 c) and d) further support the finding of Evans and Jones, in that environmental damage accelerates the crack growth in Ti-6246 as the temperature is increased [76][144].

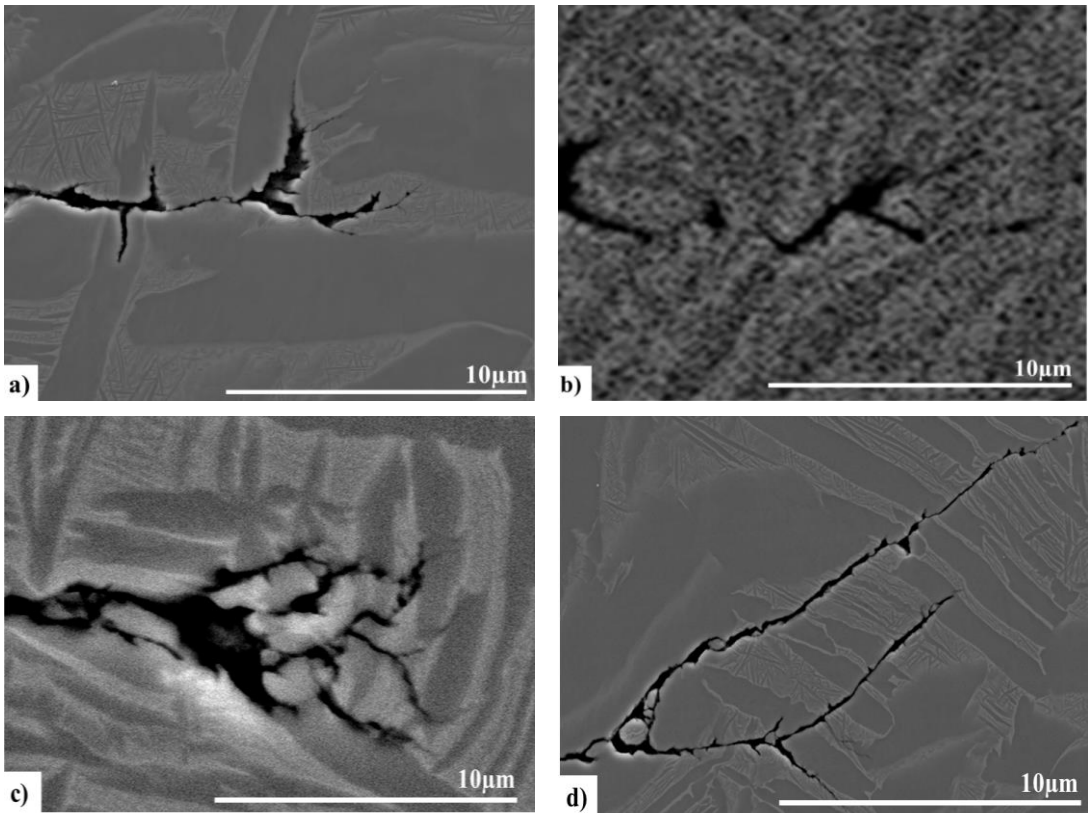

Figure 6.42 Micrographs displaying the crack tips of Ti-6246 TMFCG specimens tested under a) IP at 200-500°C b) OP at 200-500°C c) IP at 200-550°C d) OP at 200-550°C

Initial EBSD analysis has shown that under IP test conditions, less strain is retained around the crack plane than during OP testing. This could be indicative of stress relief and evidence of creep. Such findings support the micrographs in which creep and oxidation have been seen to be prominent damage mechanisms during TMFCG testing.

7 CONCLUSIONS

7.1 Test Development

This investigation has seen the development of a bespoke test facility that allows for accurately controlled, repeatable load controlled TMFCG testing. As no test standards currently exist for TMFCG testing, the code of practice for strain controlled TMF testing and the code of practice for load controlled TMF testing have been used as guidelines when developing the TMFCG facilities that utilise a 100kN servo-hydraulic test rig and an ICS. The development of the test facility has led to the following conclusions:

- Careful selection of an ICS is required to ensure the appropriate heating rates are achieved, without the eventualities of any undesired thermal gradients. Through thermal profiling of five different ICS, it has been possible to select an ICS that provides uniform heating rates across the test specimen. The selected ICS is a non-uniform multi-turn longitudinal field helical coil.
- It is possible to eradicate any undesired current interference whilst combining an ICS with the DCDP method through careful selection of the ICS. Like TCs, the directionality of the DCPD probes can result in interference. However, unlike TCs, the directionality of the DCPD probes cannot be changed, thus the ICS selected must compliment this. This investigation found that a longitudinal field helical coil did not cause interference, whereas a transversal field helical coil did.
- A cause for concern for some researchers, when using an ICS, is the occurrence of localised crack tip heating and the adverse effects that may come with it. Using an IRTC it has been possible to investigate the occurrence of localised crack tip heating. Furthermore, it has been possible to conclude that this study showed no localised crack tip heating when using an ICS as a part of this investigation.
- As well as rapid heating rates, TMF testing requires rapid cooling rates. Investigating different cooling methods, this project has shown that four air amplifiers are an economical, effective method of achieving uniform, rapid cooling. However, through thermal profiling, this study has also highlighted the difficulty in achieving such cooling.

- This study has also considered the use of a bespoke RLF for the use of TMFCG testing. It has shown that larger thermal gradients are present during the thermal cycle of the specimen, and this has been seen to affect the FCG rates. When compared to the thermal profile generated in the ICS, it was found that the RLF created a large temperature gradient during the heating cycle, whilst both the ICS and RLF experienced temperature lags across the specimen upon cooling. This highlights the challenge in achieving both uniform heating and cooling during TMFCG testing.

7.2 Test Results

This investigation set out to characterise the TMFCG behaviour of Ti-6246. The development of a bespoke test facility has resulted in a number of successful TMFCG tests being conducted. The effect of phase angle and maximum cycle temperature have been the primary focus of this test programme and from this, the following conclusions can be made:

- The development of the TMFCG test facilities saw the need to compare different heating methods. Preliminary IFCG tests using three different heating apparatus (a conventional furnace, an ICS and a RLF) concluded that both an ICS and RLF provided suitably reliable and repeatable FCG rates.
- A TMFCG comparison using an ICS and a RLF was conducted to determine the reliability and repeatability of the two systems for such testing. Small differences in the FCG rate suggests the temperature gradient created in the RLF may be resulting in thermal stresses that subsequently increase the FCG rates. This investigation has therefore highlighted that the ICS and RLF should not be used interchangeably throughout a TMFCG investigation, and in fact that the RLF may not be appropriate at all.
- In comparing the IP and OP TMFCG behaviour of Ti-6246 at 200-500°C, it was found that IP conditions resulted in faster FCG rates than OP. With maximum temperature and maximum stress occurring concurrently under IP conditions, this finding was not unexpected.
- Increasing the maximum cycle temperature to 550°C saw the disparity in IP and OP TMFCG reduce. The possibility of this reduced difference in TMFCG rates being a result of general scatter within the data was ruled out, due to the findings of other researchers that concluded this was a material behaviour. It is reasonable to conclude that this finding is likely to be a result of increased influence of time-dependent damage mechanisms at higher temperatures in Ti-6246.
- Compared to IFCG testing, it was found that IP TMF conditions resulted in faster FCG rates at both T_{MAX} = 500°C and T_{MAX} = 550°C and thus it is possible to conclude that IP is more detrimental than IF.

- Moving away from the two extremes (IP and OP), the effects of loading direction was investigated by conducting TMFCG tests at +90° (CW) and -90° (ACW). The Paris curves showed very little difference in the FCG rates and it is possible to conclude that the directionality of the diamond cycles (CW and ACW) has little to no effect on the TMFCG behaviour of Ti-6246.
- As the phase angle that most closely represents in-service conditions of the circumferential loading slot of an IP compressor disc is -135°, the effect of increasing phase angle in the ACW direction was investigated. In addition to IP, OP, CW (+90°) and ACW (-90°), tests were conducted at -135°, -150° and -170°. Although the differences in Paris curves were subtle, it was found that as the phase angle increases towards OP, the FCG rate reduces.
- It was also noted, throughout this test programme, that under all loading conditions, at higher ΔK values, the FCG rates appear to converge. This may be because of the incremental crack growth, due to oxidation, being overridden by dynamic fatigue at higher ΔK values.

7.3 Post-test Analysis

To aid the characterisation of the TMFCG behaviour of Ti-6246, various post-test analysis techniques were adopted as part of this investigation. Using a variety of microscopy techniques, the fracture surfaces and microstructures of the test specimens were analysed. Focusing predominately on test specimens subject to IP and OP TMF conditions at 200-500°C and 200-550°C. the following conclusions can be made:

- With a better understanding of the TMF behaviour of nickel-based superalloys, this study has directly compared the TMF behaviour of Ti-6246 to that of the nickel-based superalloy, RR1000. A marked transition from intergranular cracking under IP TMF conditions to transgranular cracking under OP is reported in RR1000. This transition has been attributed to the increased influence of the environment during IP testing. At 200-500°C the differences are far more subtle in Ti-6246 than previously noted in RR1000. This investigation has seen that IP TMF conditions display a mix of interlamellar and translamellar cracking on a finer scale, which on a larger scale, presents as predominately transgranular. OP conditions, on the other hand, resulted in a very flat fracture surface, indicating a translamellar/transgranular fracture mode.
- Profilometry of the fracture surfaces show that IP test conditions result in a much rougher fracture surface than OP test conditions. This further supports that there must be difference damage mechanisms present under the varying TMFCG phase angles.
- At 200-550°C, IP TMF conditions still present a mixed fracture mode, with evidence of interlamellar cracking in a predominately transgranular fracture. However, the OP TMF conditions at the higher T_{MAX} also shows evidence of interlamellar cracking, particularly as the crack progresses and ΔK increases. This finding suggests an increased influence from the environment at increased temperatures in Ti-6246 and compliments the presented FCG rates.
- At both temperatures, secondary cracking is present in the IP test specimens. Previous research suggests this α-β interface cracking is due to environmental influences. At 200-550°C, secondary cracking is also noted in the OP test specimens. This finding would support the conclusion that such interface cracking is attributed to oxidation.

- As well as exposing interface secondary cracking, the microstructural analysis along the crack also shows evidence of creep.
- IPF maps, produced through EBSD analysis, shows the fatigue crack does not follow any particular path or microstructural features. This suggests the TMFCG behaviour of Ti-6246 is not necessarily influenced by localised texture. Larger scale optical microscopy shows that the TMFCG behaviour of Ti-6246 is also not necessarily influenced by texture within the bulk material.
- Analysing phase maps, it is evident that the primary crack growth is also not necessarily influenced by distribution of the α and β phases within the microstructure.
- The presence of creep is supported by the strain contouring maps. The maps show that the material experiences stress relaxation along the crack and ahead of the crack tip during IP at both temperatures.
- Initial EDS shows the additional presence of oxygen in the plane of the fatigue crack. However, it does not show growth of an oxide layer. Nevertheless, the influence of oxidation has been evidenced throughout this study and thus, this requires further investigation.

8 FUTURE WORK

The current work has provided a good foundation into the understanding of TMFCG behaviour of Ti-6246. With the development of a robust test facility and the production of invaluable test results, the findings of this project have aided the lifing predictions computed by Rolls-Royce plc. At this relatively early stage of research, some questions have been generated which will act as potential areas for future work. Such areas include, but are not limited to:

- Carrying out more repeated tests to establish a strong data set that will enable conclusive findings to be reported. By conducting such repeats, the determination of data scatter can be made and thus improve the understanding of TMFCG behaviour of Ti-6246.
- Continue investigating the effects of phase angle on TMFCG behaviour. This programme presented TMFCG results for varying phase angles in the ACW direction, by conducting tests at phases angles in the CW direction, a better understanding of the influence of phase angle on TMFCG behaviour can be gained.
- This programme focused on two thermal cycles, whilst the maximum stress, stress ratio and frequency for every TMFCG test was kept constant. By altering the other test conditions, their effects on the TMFCG behaviour of Ti-6246 can be understood.
- To compliment additional tests, TMFCG tests conducted under vacuum would prove particularly useful in better understanding the effects of oxidation on the TMFCG behaviour.
- Further post-test analysis, such as transmission electron microscopy (TEM) may provide a better understanding of the dislocation formation and movement for each phase angle, thus providing a better understanding of their contributions to the overall TMFCG behaviour.
- An IRTC is already incorporated into the test setup. Further investigation into the use of such device for crack monitoring will allow for a completely non-invasive test facility, with the IRTC able to monitor both temperature and FCG.

- The test facility has been developed with future adaptability in mind. The chosen ICS system not only accommodates the integration of an IRTC but will also accommodate the integration of strain control/strain monitoring. By incorporating extensometers into the setup, it will be possible to investigate the influence of factors, such as strain range, on the TMFCG behaviour of Ti-6246.

9 REFERENCES

[1] Advisory Council for Aviation Research and Innovation in Europe (ACARE). Protecting the environment and the energy supply [Internet]. [Accessed 03-Jun-2016]. Available from: https://www.acare4europe.org/sria/flightpath-2050-goals/protecting-environment-and-energy-supply-0.

[2] Hardy MC, Zirbel B, Shen G, Shankar R. Developing damage tolerance and creep resistance in a high strength. Superalloys. 2004:83–90.

[3] AZoM. Titanium alloys for aeroengine and airframe applications [Internet]. [Accessed: 24-Jan-2017]. Available from: http://www.azom.com/article.aspx?ArticleID=1569.

[4] eFatigue LLC. Thermomechanical technical background [Internet]. 2008 [Accessed: 07-Mar-2016]. Available from: https://www.efatigue.com/hightemp/background/tmf.html.

[5] Titanium Engineers. Titanium 6Al-2Sn-4Zr-6Mo Ti 6246 (UNS R56260). Texas: Titanium engineers; 2016.

[6] Whittaker M. Titanium in the gas turbine engine. Advances in Gas Turbine Technology. 2011:4:315-336.

[7] Kumar AD, Sathyanarayanan S, Gupta SD, Nageswara RM. Gas turbine materials - current status and its developmental prospects - a critical review. Vellore: VIT University; 2014.

[8] Winstone MR, Brooks JL. Advanced high temperature materials: aeroengine fatigue. Ciencia & Tecnologia dos Materiais. 2008;20(1):15-24.

[9] Rolls-Royce plc. The Jet Engine. Fifth edition. Derby: The technical publications department; 1986.

[10] The Commercial Aviation Safety Team. Fundamentals of gas turbine engines. 2011.

[11] Gutta B, Srinadh K, Srinivasan J. Analysis of the effect of break edge in load and lock slot of circumferential dovetail disk of gas turbine compressor. Int J. Sci Eng Res. 2014;2(5):55-57.

[12] Whittaker MT, Harrison W, Hurley PJ, Williams S. Modelling the behaviour of titanium alloys at high temperature for gas turbine applications. Mater. Sci. Eng. A. 2010;527(16-17):4365-4372.

[13] Bache M. A review of dwell sensitive fatigue in titanium alloys : the role of microstructure , texture and operating conditions. Int. J. Fatigue. 2003;25(9-11):1079-1087.

[14] McHargue CJ. The crystallograghy of the titanium transformation. Acta Crystallogr. 1952;519(6).

[15] Barrett CS. Structure of metals. First edition. New York. Horney Press; 2008.

[16] Callister WD. Materials science and engineering an introduction. Eighth edition. Danvers: John Wiley & Sons, Inc; 2012.

[17] Leyens C, Peters M. Titanium and titanium alloys: fundamentals and applications. Cologne: Wiley-VCH; 2003.

[18] Destefani JD. Introduction to titanium and titanium alloys. ASM handbook: properties and selection: nonferrous alloys and special-purpose materials. 1990:586-591.

[19] Peters M, Kumpfert J, Ward C, Leyens C. Titanium alloys for aerospace applications. Adv. Eng. Mater. 2003;5(6):419-427.

[20] Donachie MJ. Titanium: a technical guide. Second edition. ASM International; 2000.

[21] Birosca S, Buffiere JY, Garcia-pastor FA, Karadge M, Babout L, Preus M. Three-dimensional characterization of fatigue cracks in ti-6246 using x-ray tomography and electron backscatter diffraction. Acta Mater. 2009;57(19):5834-5847.

[22] Lutjering G, Williams JC. Titanium. Second edition. New York: Springer; 2007.

[23] Lancaster RJ, Whittaker MT, Williams SJ. A review of thermo-mechanical fatigue behaviour in polycrystalline nickel superalloys for turbine disc applications. Mater. High Temp. 2013;30(1):2-12.

[24] Jones J, Whittaker M, Lancaster R, Williams S. Lifing the thermo-mechanical fatigue (TMF) behaviour of the polycrystalline nickel-based superalloy RR1000. MATEC Web Conf. 2014;19001:1-6.

[25] Huang ZW, Wang ZG, Zhu SJ, Yuan FH, Wang FG. Thermomechanical fatigue behavior and life prediction of a cast nickel-based superalloy. Mater. Sci. Eng. A. 2006;432:308-316.

[26] Franclois M, Remy L. Thermal-mechanical fatigue of MAR-M 509 superalloy comparison with low-cycle fatigue behavior. Fatigue Fract. Eng. Mater. Struct. 1991;14(1):115-129.

[27] Pahlavanyali S, Drew G, Rayment A, Rae C. Thermo-mechanical fatigue of a polycrystalline superalloy: the effect of phase angle on TMF life and failure. Int. J. Fatigue. 2008;30:330-338.

[28] Nagesha A, Kannan R, Parameswaran P, Sandhya R, Sankara K, Singh V. A comparative study of isothermal and thermomechanical fatigue on type 316L (N) austenitic stainless steel. Mater. Sci. Eng. A. 2010;527(21):5969-5975.

[29] Cai C, Liaw P, Ye M, Yu J. Recent developments in the thermomechanical fatigue life prediction of superalloys. J. Mater. 1999;51(4).

[30] Reardon AC. Metallurgy for the non-metallurgist. Second edition. ASM International; 2011.

[31] Suresh S. Fatigue of materials. Second edition. Cambridge: Cambridge University Press; 1998.

[32] Bache MR, Evans WJ. Impact of texture on mechanical properties in an advanced titanium alloy. Mater. Sci. Eng A. 2001;319:409-414.

[33] Sangid MD. The physics of fatigue crack initiation. Int. J. Fatigue. 2013;57:58-72.

[34] Forrest PG. Fatigue of metals. First Edition. Pergamon Press Ltd; 1962.

[35] Totten GE. Fatigue crack propagation. Tech spotlight. 2008:39-41.

[36] Dowling NE. Mean stress effects in stress-life and strain-life fatigue. SAE Technical Paper 2004-01-2227. 2004.

[37] Total Materia. Application of fracture mechanics [Internet]. 2011 [Accessed: 15-Aug-2016]. Available from: http://www.totalmateria.com/page.aspx?ID=CheckArticle&site=kts&NM=353.

[38] Whittaker MT. Considerations in fatigue lifing of stress concentrations in textured titanium 6-4. Int. J. Fatigue. 2011;33(10):1384-1391.

[39] IHI Inspection & Instrumentation Co., Ltd. Damage inspection and countermeasure proposals [Internet]. [Accessed: 07-Aug-2016]. Available: http://www.iic-hq.co.jp/english/03sp/02camt/02mt/ZS-02.html.

[40] Anderson TL. Fracture mechanics: fundamentals and applications. Third edition. CRC Press; 2005.

[41] Lankford J, Davidson D, Morris W, Wei R. Short fatigue cracks. Fatigue Mech. Quantitative Meas. Phys. Damage. Michigan: ASTM Publication; 1983.

[42] Total Materia. Linear elastic fracture mechanics (LEFM): part two [Internet]. 2010 [Accessed: 15-Aug-2016]. Available from: http://www.totalmateria.com/page.aspx?ID=CheckArticle&site=kts&NM=299.

[43] Nondestructive Testing Resource Center. Fatigue crack initiation [Internet]. 2016 [Accessed: 15-Aug-2016]. Available from: https://www.nde-ed.org/EducationResources/CommunityCollege/Materials/Structure/fatigue.htm.

[44] Whittaker M, Harrison W, Lancaster R, Williams S. An analysis of modern creep lifing methodologies in the titanium alloy Ti6-4. Mater. Sci. Eng. A. 2013;577:114-119.

[45] Lee S, Jeon J, Kim Y. Interfacial reaction between liquid titanium and oxide mold contained alpha-case formation phase during investment casting. 13th World conference on titanium. 2015:387–391.

[46] Hormozi R, Biglari F, Nikbin K. Experimental study of type 316 stainless steel failure under LCF/TMF loading conditions. Int. J. Fatigue. 2015;75:153-169.

[47] Strangman TE. Thermal-mechanical fatigue life model for coated superalloy turbine components. Arizona: The Minerals, Metals & Materials Society; 1992.

[48] Zhang P, Zhu Q, Chen G, Wang C. Review on Thermo-mechanical fatigue behavior of nickel-base superalloys. Mater. Trans. 2015;56(12):1930-1939.

[49] Christ H. Is thermomechanical fatigue life predictable? Procedia Eng. 2013;55:181-190.

[50] De Yedra AD, Martín RR, Pedrejón JL. Thermo-mechanical fatigue behaviour and life prediction of C-1023 nickel based superalloy. 2011;3(6):88-101.

[51] Lee D, Lee J, Kim Y, Koo J, Seok C, Kim Y. Thermo mechanical fatigue life prediction of ni-based. Int. J. Precis. Eng. Man. 2017;18(4):561-566.

[52] Larsen J, Worth B, Annis C, Hoake F. An assessment of the role of near-threshold crack growth in high-cycle fatigue life prediction of aerospace titanium alloys under turbine engine spectra. Int. J. Fract. 1996;80:237-255.

[53] Powell BE. Fatigue crack growth behaviour of two contrasting titanium alloys. Int. J. Fatigue. 1995;170(3):221-227.

[54] Saxena VK, Radhakrishnan VM. Effect of phase morphology on fatigue crack growth behavior of α-β titanium alloy — a crack closure rationale. Metall. Mater. Trans. A. Phys. Metall. Mater. Sci. 1998;29(1):245-261.

[55] Jha SK, Ravichandran KS. Effect of mean stress (stress ratio) and aging on fatigue-crack growth in a metastable beta titanium alloy. Metall. Mater. Trans. A. Phys. Metall. Mater. Sci. 2000;31(3):703-713.

[56] Jin O, Mall S. Effects of microstructure on short crack growth behavior of Ti-6Al-2Sn-4Zr-2Mo-0.1Si alloy. Mater. Sci. Eng. A. 2003;359(1):356-367.

[57] Sansoz F, Ghonem H. Effects of loading frequency on fatigue crack growth mechanisms in α/β Ti microstructure with large colony size. Mater. Sci. Eng. A. 2003;34:2565-2577.

[58] Sansoz F, Ghonem H. Fatigue crack growth mechanisms in ti6242 lamellar microstructures: influence of loading frequency and temperature. Metall. Mater. Trans. A. Phys. Metall. Mater. Sci. 2003;34(11):2565-2577.

[59] Sadananda K, Vasudevan A. Fatigue crack growth behavior of titanium alloys. Int. J. Fatigue. 2005;27(10):1255-1266.

[60] Adib A, Baptista C. An exponential equation of fatigue crack growth in titanium. Mater. Sci. Eng. A. 2007;453(4):321-325.

[61] Noroozi A, Glinka G, Lambert S. A study of the stress ratio effects on fatigue crack growth using the unified two-parameter fatigue crack growth driving force. Int. J. Fatigue. 2007;29:1616-1633.

[62] Korsunsky A, Song X, Belnoue J, Jun T, Hofmann F, De Matos P et al. Crack tip deformation fields and fatigue crack growth rates in Ti–6Al–4V. Int. J. Fatigue. 2009;31(11):1771-1779.

[63] Ghonem H. Microstructure and fatigue crack growth mechanisms in high temperature titanium alloys. Int. J. Fatigue. 2010;32(9):1448-1460.

[64] Walker KF, Newman JC. Improved test method and analytical modelling for fatigue crack growth in coarse-grain titanium alloy with rough fatigue surfaces. Fatigue Fract. Eng. Mater. Struct. 2014;37(6):659–670.

[65] Dubey S, Soboyejo A, Soboyejo W. An investigation of the effects of stress ratio and crack closure on the micromechanisms of fatigue crack growth in Ti-6Al-4V. Acta Mater. 1997;45(7):2777-2787.

[66] J. Qiu, X. Feng, Y. Ma, J. Lei, Y. Liu, A. Huang, D. Rugg, and R. Yang, “Fatigue crack growth behavior of beta-annealed Ti – 6Al – 2Sn – 4Zr – x Mo (x = 2 , 4 and 6) alloys : Influence of microstructure and stress ratio,” vol. 83, pp. 150–160, 2016.

[67] Ding J, Hall R, Byrne J. Effects of stress ratio and temperature on fatigue crack growth in a Ti–6Al–4V alloy. Int. J. Fatigue. 2005;27(10):1551-1558.

[68] Yoder G, Eylon D. On the effect of colony size on fatigue crack growth in widmanstatten structure α+β titanium alloys. Metall. Mater. Trans. A. Phys. Metall. Mater. Sci. 1979;10(11):1808-1810.

[69] Ruppen J, Bhowal P, Eylon D, McEvily A. On the process of subsurface fatigue crack initiation in Ti-6Al-4V. Fatigue Mech. 1979;17:47–68.

[70] Bania P, Eylon D. Fatigue crack propagation of titanium alloys under dwell-time conditions. Metall. Mater. Trans. A. Phys. Metall. Mater. Sci. 1978;9(6):847-855.

[71] Sommer A, Eylon D. On fatigue crack propagation of titanium alloys under dwell time conditions. Metall. Mater. Trans. A. Phys. Metall. Mater. Sci. 1983;14(10):2178-2181.

[72] Eylon D, Hall J, Pierce C, Ruckle D. Microstructure and mechanical properties relationships in the ti-11 alloy at room and elevated temperatures. Metall. Mater. Trans. A. Phys. Metall. Mater. Sci. 1976;7(12):1817-1826.

[73] Ravichandran K. Near threshold fatigue crack growth behavior of a titanium alloy: Ti-6Al-4V. Acta Metall. Mater. 1991;39(3):401–410.

[74] Lesterlin S, Sarrazin-Badoux C, Petit J. Influence of environment at 500°C on fatigue behaviour in a ti6246 alloy. Advances in Fracture Research. 1997:367-374.

[75] Sankaran SN, Herrmann RK, Outlaw RA, Clark RK. Barrier-layer formation and its control during hydrogen permeation through Ti-24AI-11Nb alloy. Metall. Mater. Trans. A. Phys. Metall. Mater. Sci. 1994;25(1):89-97.

[76] Evans WJ, Jones JP, Williams SJ. The interactions between fatigue, creep and environmental damage in Ti 6246 and Udimet 720Li. Int. J. Fatigue. 2005;27(10):1473-1484.

[77] Hurley PJ, Evans WJ. A new method for predicting fatigue crack propagation rates. Mater. Sci. Eng. A. 2006;466(9):265-273.

[78] Hurley P, Whittaker M, Webster P, Evans W. A methodology for predicting creep/fatigue crack growth rates in Ti 6246. Int. J. Fatigue. 2007;29(9):1702-1710.

[79] Hurley PJ, Whittaker MT, Evans WJ, Williams SJ. Prediction of fatigue initiation lives in notched Ti 6246 specimens. Int. J. Fatigue. 2008;30(4):623-634.

[80] ASTM E2368-10(2017). Standard practice for strain controlled thermomechanical fatigue testing. West Conshohocken: ASTM International; 2017.

[81] Jones J, Whittaker M, Lancaster R, Williams S. The influence of phase angle, strain range and peak cycle temperature on the TMF crack initiation behaviour and damage mechanisms of the nickel-based superalloy, RR1000. Int. J. Fatigue. 2017;98(5):279-285.

[82] Kirka MM, Brindley KA, Neu RW, Antolovich SD, Shinde SR, Gravett PW. Parameters influencing thermomechanical fatigue of a directionally-solidified ni-base superalloy. Int. J. Fatigue. 2015;81(12):48-60.

[83] Guth S, Doll S, Lang K. Influence of phase angle on lifetime, cyclic deformation and damage behavior of Mar-M247 LC under thermo-mechanical fatigue. Mater. Sci. Eng. A. 2015;642:42-48.

[84] Kulawinski D, Weidner A, Henkel S, Biermann H. Isothermal and thermo-mechanical fatigue behavior of the nickel base superalloy waspaloy under uniaxial and biaxial-planar loading. Int. J. Fatigue. 2015;81:21-36.

[85] Marchionni M, Klingelhöffer H, Kühn H, Ranucci T, Matzak K. Thermo-mechanical fatigue of the nickel-base superalloy nimonic 90 the mechanical behavior of materials x. Key Eng. Mater. 2007;345:347-350.

[86] Beck T, Pitz G, Lang K, Lohe D. Thermal-mechanical fatigue of IN 792 CC. Mater. Sci. Eng. A. 1997;236:719-722.

[87] Liu F, Ai S, Wang Y, Zhang H, Wang Z. Thermal-mechanical fatigue behavior of a cast K417 nickel-based superalloy. Int. J. Fatigue. 2002;24(8):841-846.

[88] Kadioglu Y, Sehitolgu H. Thermomechanical and isothermal fatigue behavior of bare and coated superalloys. J. Eng. Mater. Technol. 1996;118(1):94-102.

[89] Hyde C, Sun W, Hyde T. An investigation of the failure mechanisms in high temperature materials subjected to isothermal and anisothermal fatigue and creep conditions. Procedia Eng. 2011;10:1157-1162.

[90] Lerch B, Jayaraman N, Antolovich S. A study of fatigue damage mechanisms in waspaloy from 25. Mater. Sci. Eng. 1984;66(2):151-166.

[91] Pretty CJ, Whitaker MT, Williams SJ. Thermo-mechanical fatigue crack growth of RR1000. Materials (Basel). 2017;10(1):34-54.

[92] Prasad K, Kumar V, Rao K, Sundararaman M. A comparative assessment of crack closure mechanisms in timetal 834 near a titanium alloy under isothermal and thermomechanical fatigue loading. J. Alloys Compd. 2016;688:8-11.

[93] Prasad K, Kumar V. Isothermal and thermomechanical fatigue behaviour of Ti – 6Al – 4V titanium alloy. Mater. Sci. Eng. A. 2011;528(19-20):6263-6270.

[94] Christ HJ. Effect of environment on thermomechanical fatigue life. Mater. Sci. Eng. A. 2007;468-470:98-108.

[95] Jones JP, Brookes SP, Whittaker MT, Lancaster RJ. Non-invasive temperature measurement and control techniques under thermomechanical fatigue loading. Mater. Sci. Technol. 2014;30(15):1862-1874.

[96] Severn Thermal Solutions. Split furnace range [Internet]. [Accessed: 29-Sep-2019]. Available from: https://www.severnts.co.uk/products/split-furnace-2/.

[97] Rudnev V, Loveless D, Cook R, V. Handbook of Induction Heating. Second edition. Florida: CRC Press; 2017.

[98] Jones J, Brookes S, Whittaker M, Lancaster R, Ward B. Assessment of infrared thermography for cyclic high-temperature measurement and control. Evaluation of Existing and New Sensor Technologies for Fatigue, Fracture and Mechanical Testing. West Conshohoken, PA: ASTM International; 2015.

[99] Yuan H, Kalkhof D. Effects of temperature gradients on crack characterisation under thermal-mechanical loading conditions. Int. J. Fract. 2000;2:355-277.

[100] Andersson H, Sjostrom E. Thermal gradients in round TMF specimens. Int. J. Fatigue. 2008;30:391-396.

[101] Evans WJ, Screech JE, Williams SJ. Thermo-mechanical fatigue and fracture of INCO718. Int. J. Fatigue. 2008;30:257-267.

[102] Pernot J, Nicholas T, Mall S. Modelling thermomechanical fatigue crack growth rates in Ti-24AI- 11Nb. Int. J. Fatigue. 1994;16(2):111-122.

[103] Mall S, Nicholas T, Pernot J, Burgess D. Crack growth in a titanium aluminide alloy under thermal mechanical cycling. Fatigue Fract. Eng. Mater. Struct. 1991;14(1):79-87.

[104] Brookes S, Scholz A, Whittaker M, Loveday M, Wisby A, Ryder N et al. Code of practice for force-controlled thermo-mechanical fatigue testing. Berlin, Germany: Federal Institute for Materials Research and Testing (BAM); 2015.

[105] The British Standards Institution. BS ISO 12111:2011 - Metallic materials, fatigue testing, strain-controlled thermomechanical fatigue testing method. Geneva: BSI ISO; 2011.

[106] Hähner P, Rinaldi C, Bicego V, Affeldt E, Brendel T, Andersson H et al. Research and development into a European code-of-practice for strain-controlled thermo-mechanical fatigue testing. Int. J. Fatigue. 2008;30(2):372-381.

[107] Jones J. Enhancing the accuracy of advanced high temperature mechanical testing through thermography. Appl. Sci. 2018;8(3):380.

[108] Beck T, Rau K. Temperature measurement and control methods in TMF testing – a comparison and evaluation. Int. J. Fatigue. 2008;30:226-233.

[109] Brookes S, Kühn H, Skrotzki B, Klingelhöffer H, Sievert R, Pfetzing J et al. Axial- torsional thermomechanical fatigue of a near-γ TiAl-alloy. Mater. Sci. Eng. A. 2010;527(16):3829-3839.

[110] Palmer J, Jones J, Dyer A, Smith R, Lancaster R, Whittaker M. Development of test facilities for thermo-mechanical fatigue testing. Int. J. Fatigue. 2019;121(4):208-218.

[111] Hähner P, Affeldt E, Beck T, Klingelhöffer H, Loveday M, Rinaldi C. Validated code-of-practice for thermo-mechanical fatigue testing. Berlin, Germany: Federal Institute for Materials Research and Testing (BAM); 2006.

[112] Incropera F, DeWitt D, Bergman T, Avine L. Fundamentals of Heat and Mass Transfer. Sixth edition. New Jersey: John Wiley & Sons Inc; 2007.

[113] Younes CM, Allen GC, Nicholson JA. High temperature oxidation behaviour of single crystal superalloys RR3000 and CMSX-4. Corros. Eng. Sci. Technol. 2007;42(1): 80-88.

[114] Gemma A, Langer B, Leverant G. Thermomechanical fatigue crack propagation in an anistropic (directionally solidified) nickel-base superalloy. Thermal Fatigue of Materials and Components. West Conshohoken, PA: ASTM International; 1976.

[115] Jordan EH, Meyers GJ. Fracture mechanics applied to nonisothermal fatigue crack growth. Eng. Fract. Mech. 1986;23(2):345-358.

[116] Meola C. Infrared Thermography Recent Advances and Future Trends. Italy: Bentham Science Publishers; 2012.

[117] Rau C, Gemma A, Leverant G. Thermal-mechanical fatigue crack propagation in nickel and cobalt-base superalloys under various strain-temperature cycles. Fatigue at Elevated Temperatures. West Conshohoken, PA: ASTM International; 1973.

[118] Masakazu O, Takashi K. Crack propagation of steels during low cycle thermal-mechanical and isothermal fatigue at elevated temperatures. Metall. Mater. Trans. A. Phys. Metall. Mater. Sci. 1983;14(8):1641-1648.

[119] Pelloux R, Marchand N. Thermal-mechanical fatigue behavior of nickel-base superalloys. Massachusetts: Massachusetts Institute of Technology; 1986.

[120] Kim K, Van Stone R. Crack growth under thermo-mechanical and temperature gradient loads. Eng. Fract. Mech. 1997;58(1):133-147.

[121] The British Standards Institution. BS ISO 12108:2012 Metallic materials, fatigue testing, fatigue crack growth method. Geneva: BSI ISO; 2012.

[122] ASTM E647. Standard test method for measurement of fatigue crack growth rates. West Conshohocken: ASTM International; 2013.

[123] Matec Ltd. The potential drop technique & its use in fatigue testing. London: Matec Ltd.

[124] Chapman T, Chater R, Saunders E, Walker A, Lindley T, Dye D. Environmentally assisted fatigue crack nucleation in Ti-6Al-2Sn-4Zr-6Mo. Corros. Sci. 2015;96:87-101.

[125] Boyer R, Collings E, Welsch G. Materials properties handbook: titanium alloys. Fourth Edition. Ohio: ASM International; 2007.

[126] Total Materia. Heat treating of titanium and titanium alloys [Internet]. 2004 [Accessed 20-Aug-2016]. Available from: http://www.totalmateria.com/Article97.htm.

[127] Polmear I, St John D, Nie J, Qian M. Light alloys: metallurgy of the light metals. Fifth Edition. Elsevier; 2017.

[128] Leyens C, Peters M. Handbook of Cellular Metals Phase Transformations in Materials. Wiley-VCH; 2003.

[129] Bache M. Calibration policy. Swansea: Swansea Materials Research & Testing Ltd (SMaRT); 2015.

[130] Bache M. Sub-contracted calibrations. Swansea: Swansea Materials Research & Testing Ltd (SMaRT); 2016.

[131] Special Metals. Product handbook of product handbook of high-performance nickel alloys. West Virginia: Special Metals.

[132] Timet. Timetal 6-2-4-6 high strength intermediate temperature alloy. USA: Titanium Metals Corporation; 2000.

[133] The Spray Nozzle People. Air Amplifiers [Internet]. [Accessed 15-Jun-2018]. Available from: https://www.spray-nozzle.co.uk/spray-nozzles/air-nozzles/air-amplifiers.

[134] Meneghetti G, Ricotta M. Evaluating the heat energy dissipated in a small volume surrounding the tip of a fatigue crack. Int. J. Fatigue. 2016;92(2):605–615.

[135] Vander Voort GF. Metallography and microstructures. Ohio: ASM International; 2004.

[136] Thermo Fisher Scientific. How to choose a scanning electron microscope (SEM): guidelines for selecting the best microscope for your research. Thermo Fisher Scientific; 2019.

[137] Bruker Alicona. Infinite Focus [Internet]. [Accessed 10-May-2019]. Available from: https://www.alicona.com/en/products/infinitefocus/.

[138] ASME B46.1-2009. Surface texture (surface roughness , waviness , and lay). New York: The American Society of Mechanical Engineers; 2002.

[139] Blunt L, Jiang X. Advanced Techniques for Assessment Surface Topography. Elsevier Ltd; 2003.

[140] Stout K, Blunt L, Dong W, Mainsah E, Luo N, Mathia T et al. Development of Methods for Characterisation of Roughness in Three Dimensions. First Edition. Butterworth-Heinemann; 2000.

[141] The British Standards Institution. BS ISO 25178-2:2012 Geometrical product specifications (GPS) - surface texture: areal - part 2: terms, definitions and surface texture parameters. Geneva; BSI ISO: 2012.

[142] Materials Evaluation and Engineering Inc. Energy dispersive X-ray spectroscopy (EDS) [Internet]. [Accessed 27-Aug-2018]. Available from: https://www.mee-inc.com/hamm/energy-dispersive-x-ray-spectroscopyeds/.

[143] Nikon Instruments Inc. Polarized light microscopy [Internet]. [Accessed 27-Aug-2018]. Available from: https://www.microscopyu.com/techniques/polarized-light/polarized-light-

microscopy.

[144] Jones JP, Bache MR, W. J. Evans WJ. High temperature fatigue behaviour of Ti6246. Swansea: Swansea University; 1996.

[145] Ghonem H, Foerch R. Frequency effects on fatigue crack growth behavior in a near-a titanium alloy. Mater. Sci. Eng. A. 1991;138:69-81.

[146] Pretty CJ. Thermo-mechanical fatigue crack growth of a polycrystalline nickel alloy. Swansea: Swansea University; 2014.

[147] Jones J, Whittaker M, Lancaster R, Hyde C, Rouse J, Engel B et al. The effect of phase angle on crack growth mechanisms under thermo-mechanical fatigue loading. Int. J. Fatigue . 2020;135.

[148] Dang N, Liu L, Maire E, Adrien J, Cazottes S, Xiao W et al. Analysis of shear stress promoting void evolution behavior in an α/β Ti alloy with fully lamellar microstructure. Mater. Sci. Eng. A. 2018;737:27-39.

[149] Goyal S, Mariappan K, Shankar V, Sandhya R, Laha K, Bhaduri A. Studies on creep-fatigue interaction behaviour of Alloy 617M. Mater. Sci. Eng. A. 2018;730:16-23.

[150] Birosca S, Buffiere J, Garcia-Pastor F, Karadge M, Babout L, Preuss M. Three-dimensional characterization of fatigue cracks in Ti-6246 using X-ray tomography and electron backscatter diffraction. Acta Mater. 2009;57(19):5834-5847.

[151] Hu Y, Floer W, Krupp U, Christ H. Microstructurally short fatigue crack initiation and growth in Ti-6.8Mo-4.5Fe-1.5Al. Mater. Sci. Eng. A. 2000;278(1-2):170-180.

[152] Mohammadtaheri M. A new metallographic technique for revealing grain boundaries in a new metallographic technique for revealing grain boundaries in aluminum alloys. Metallogr. Microstruct. Anal. 2012;1:224-226.

[153] Vander Voort GF. Color Metallography. Microsc. Microanal. 2005;10:70-71.

[154] Maitland T, Sitzman S. Electron backscatter diffraction (EBSD) technique and materials characterization examples. Scanning microscopy for nanotechnology: techniques and applications. New York: Springer; 2007.